THESIS

DEVELOPMENT AND FABRICATION OF LOW-MASS, LOW-POWER, INTERNALLY-CALIBRATED, MMIC-BASED MILLIMETER-WAVE RADIOMETERS AT 92 AND 166 GHZ

Submitted by

Alexander L. Lee

Department of Electrical and Computer Engineering

In partial fulfillment of the requirements

For the Degree of Master of Science

Colorado State University

Fort Collins, Colorado

Spring 2012

Master's Committee:

Advisor: Steven C. Reising

Branislav Notaros
Christian D. Kummerow
Pekka Kangaslahti

ABSTRACT

DEVELOPMENT AND FABRICATION OF LOW-MASS, LOW-POWER, INTERNALLY-CALIBRATED, MMIC-BASED MILLIMETER-WAVE RADIOMETERS AT 92 AND 166 GHZ

This thesis discusses the design, fabrication, and testing of two millimeter-wave internally calibrated MMIC based radiometers operating at 92 and 166 GHz. These laboratory prototype radiometers are intended to increase the technological maturity of the radiometer components and reduce the risk, development time and cost of deploying satellite based radiometers operating in the 90-170 GHz frequency range. Specifically, radiometers at similar frequencies are being considered on NASA's SWOT mission, planned for launch in 2020. The SWOT mission is an ocean altimetry mission intended to increase the Earth science community's knowledge of the kinetic energy in ocean circulation and mesoscale eddies as well as the vertical transport of heat and carbon in the ocean.

These direct detection Dicke radiometers have two internal calibration sources integrated in the front end. These sources consist of a high excess noise ratio noise diode and a temperature controlled matched load. Internal calibration is a requirement on ocean altimetry missions to avoid the need for moving parts, which are necessary to accomplish external calibration.

The index of refraction of the atmosphere depends on temperature and humidity. The variability of humidity in time and space is more difficult to measure and model than that of temperature. Changes in the index of refraction of the atmosphere add error to satellite based ocean altimetry measurements. Microwave radiometers have been used on altimetry missions to measure the amount of atmospheric water vapor, and this data is used to correct the altimetry measurements. Traditionally, microwave radiometers in the 18-37 GHz range have been used on these missions. However, due to the large instantaneous fields of view (IFOV) on the Earth's surface, land begins to encroach upon the radiometer's surface footprint at about 40 km from the coast. The emission from the land adds additional error to the radiometer measurements. The amount of error is unknown due to the highly variable emissivity of land. The addition of higher frequency millimeter-wave radiometers in the 90-170 GHz frequency range will reduce the IFOV on the Earth's surface and therefore enable atmospheric water vapor measurements closer to the coasts.

The radiometers presented in this thesis are laboratory prototypes. They are intended to demonstrate new component technology and improve estimates of mass, volume, power consumption, and radiometric performance for future space-borne millimeter-wave radiometers.

ACKNOWLEDGEMENTS

I would first like to thank Dr. Steven Reising for his guidance and support throughout this project. I would like to thank Dr. Christian Kummerow and Dr. Branislav Notaros for their input and for serving as members of my thesis committee.

I would like to thank the team at NASA's Jet Propulsion Laboratory for their willingness to offer guidance and support whenever they were asked. There is no doubt that this work is of a higher quality because of their input. I would like to specifically thank Dr. Pekka Kangaslahti, Dr. Todd Gaier, Douglas Dawson, Oliver Montes, Mary Wells, and Heather Owens for their tremendous help.

I would like to thank the other students in the Microwave Systems Laboratory for their help with this work. I would especially like to thank Darrin Albers, Dr. Xavier Bosch, and Kyle Gilliam for their technical contributions to this work.

Lastly, I would like to thank my wife Ambrosia for her patience and support.

DEDICATION

I dedicate this thesis to my loving and supportive wife Ambrosia and my parents, Andrew and Suzanne Lee.

TABLE OF CONTENTS

LIST OF FIGURES

LIST OF TABLES

Chapter 1: Introduction

1.1 Principles of Microwave Radiometry

A black body is a theoretical object that absorbs all incident electromagnetic radiation. Since a black body is a perfect electromagnetic absorber, it is also a perfect emitter of thermal radiation. If the black body remains in thermal equilibrium, the same amount of energy that it absorbs must be emitted. Thermal radiation is electromagnetic radiation generated by the thermal motion of charged particles in matter [1]. The thermal radiation emission from a black body is dependent on the physical temperature of the body and can be described using Planck's law

$$B_f = \frac{2hf^3}{c^2}\left[1/\left(e^{\frac{hf}{kT}} - 1\right)\right] \tag{1-1}$$

where B_f is black body spectral brightness in units of W/(m^{2}SrHz), h is Planck's constant in units of J·s, f is frequency in Hz, k is Boltzmann's constant in units of J/K, T is absolute temperature in K, and c is the velocity of light in m/s [1].

For long wavelengths or high temperatures, the term in the exponential in Planck's law becomes small

$$\frac{hf}{kT} \ll 1 \tag{1-2}$$

and can be approximated by

$$e^{\frac{hf}{kT}} - 1 \approx \frac{hf}{kT} \tag{1-3}$$

This approximation leads to Planck's law being expressed as

$$B_f = \frac{2kT}{\lambda^2} \tag{1-4}$$

where λ is wavelength in units of m. This is known as Rayleigh-Jeans Law [1].

Consider an antenna viewing a blackbody. The antenna is positioned such that it only receives power from the black body. Assume the black body is at temperature *T* and we ignore any antenna ohmic losses. If the antenna is operating in the Rayleigh-Jeans region, and the detected power is limited to a narrow bandwidth where B_f is constant, the power received by the antenna can be expressed by

$$P_{bb} = kTB\frac{A_r}{\lambda^2}\iint_{4\pi} F_n(\Theta,\phi)d\Omega \tag{1-5}$$

P_{bb} is the detected power in W, A_r is the effective aperture of the antenna, and $F_n(\theta,\Phi)$ is the normalized radiation pattern of the antenna. Simplifying this equation leads to

$$P_{bb} = kT_BB \tag{1-6}$$

This is a fundamentally significant result that shows a direct linear relationship between power and brightness temperature [1].

It is important to notice that Equation (1-6) is the same equation that describes the noise power that a resistor at temperature *T* will deliver to a load. This indicates that an ideal

antenna observing an ideal black body will appear to a receiver as a terminated resistor at a temperature equivalent to the temperature of the black body that it is observing [1].

It is standard to refer to the power being emitted from a black body in terms of brightness temperature, T_B. It is more convenient to speak in terms of temperatures, as opposed to powers, so that measurements from different systems with different bandwidths can be compared more easily.

Since perfect black bodies do not exist, the concept of emissivity is used to describe how closely a material's emission resembles that of a black body. The emissivity of an object varies from zero, a perfect reflector, to one, a black body. Equation (1-7) shows the relationship between physical temperature, brightness temperature and emissivity.

$$T_B = eT \tag{1-7}$$

All matter at temperatures above absolute zero absorbs and emits electromagnetic radiation. The concepts discussed above, black body radiation, brightness temperature, and emissivity, are used in radiometry to draw insight about an object being observed by a radiometer. The most obvious information that can be gained from radiometric observations is temperature. However, many other physical quantities can be characterized using these basic concepts.

1.2 Scientific Background: SWOT Mission

NASA's Earth Science strategic goal is to "advance Earth System Science to meet the challenges of climate and environmental change." The NASA Earth Science research program focuses on six areas that are addressed through both operating and future missions. The National Research Council's first-ever Earth Science Decadal Survey, completed in 2007, recommended 14 missions for NASA to launch during 2010-2020 and an additional mission for NASA and NOAA to implement jointly. These missions were grouped into three tiers, reflecting technology readiness of the major components of the missions and the context of measurements to be made by international and interagency partners. NASA is pursuing all of the Tier 1, or first set of missions, to be ready for launch within a four-year period from mid-2010.

One of the Tier 2 missions is the Surface Water and Oceanographic Topography (SWOT) mission, which focuses on the NASA Earth Science focus areas of (1) climate variability and change, and (2) water and energy cycles. Recently accelerated and planned for launch in 2020, SWOT will expand upon NASA's series of ocean altimetry missions (in collaboration with CNES) of TOPEX, Jason-1, Jason-2 and NOAA's upcoming Jason-3 operational altimeter [2].

SWOT uses a Ka-band Radar Interferometer (KaRIN) to measure the height of the Earth's bodies of water, i.e. oceans, lakes, and rivers, on horizontal scales between 10 and 300 km. This height information allows scientists to better understand the kinetic energy in ocean circulation, and mesoscale eddies as well as the vertical transport of heat and

carbon in the ocean. SWOT will also measure water height on inland bodies of water with areas greater than 250 m^2 and rivers with widths greater than 100 m. In general, ocean altimetry data helps to improve understanding of the Earth's climate, hurricane prediction, and weather forecasting [3].

Microwave brightness temperature measurements of the atmosphere are used to retrieve the water vapor density and temperature due to microwave absorption lines of water vapor and oxygen, respectively. Knowledge of these thermodynamic variables in the atmosphere on fine temporal and spatial scales is essential to improve weather prediction and to monitor global climate processes. In the context of the SWOT mission, microwave radiometers are vital to satellite-based altimeter missions. Atmospheric water vapor changes the index of refraction of the atmosphere between the satellite and the surface thereby causing errors in the apparent surface height, called wet-tropospheric path delay. Microwave radiometers have been and are an invaluable component of past and current NASA altimeter missions (in collaboration with CNES).

Past satellite ocean altimeter missions have included a nadir-viewing, co-located 18-37 GHz multi-channel microwave radiometer to measure wet-tropospheric path delay. Due to the large diameters of the surface instantaneous fields of view (IFOV) at these frequencies, the accuracy of wet path retrievals begins to degrade at approximately 40 km from the coasts when the land begins to encroach upon the satellite's surface IFOV [4]. This "land contamination" adds error to the radiometer's atmospheric brightness temperature measurements. The amount of error is unknown due to the high variability of

the emissivity of land. Land emissivity depends upon many factors including vegetation, surface roughness, snow, and soil moisture. For the same antenna aperture, the IFOV size is proportional to the wavelength. Therefore, radiometers at higher frequencies have inherently better spatial resolution. In order to enable wet path delay measurements closer to the coastline, additional higher-frequency microwave channels with smaller IFOVs centered at 92, 130, and 166 GHz are being considered for the SWOT mission. Figure 1-1 shows an illustration of the described problem and solution.

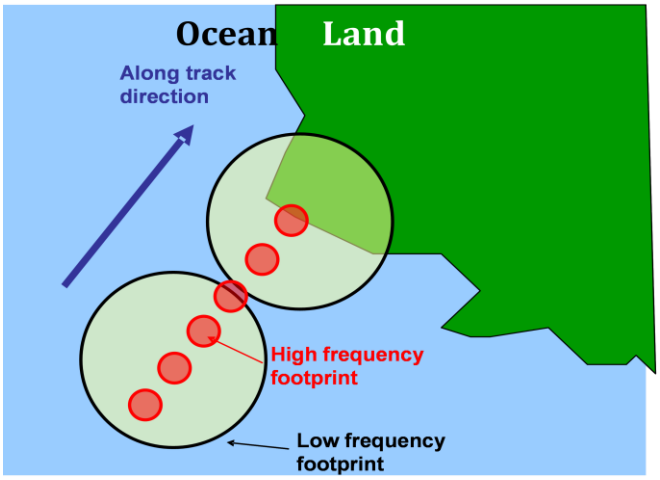

Figure 1-1. A comparison of the IFOV of the high frequency radiometers with that of the low frequency radiometers [5]

A mission concept study was completed at NASA's Jet Propulsion Laboratory (JPL) comparing the path delay error for a low frequency only algorithm, 18-37 GHz, with the path delay error for the combined low and high frequency algorithm, 18-37 GHz and 90-170 GHz. The results from this study are shown in Figure 1-2. It can be seen that the additional high frequency radiometers allow wet path delay retrievals with error less than 1 cm up to 2 km from the coast.

Traditional 18-37 GHz radiometers use water vapor sounding channels, while these higher frequency radiometers, in the 90-170 GHz range, use imaging channels. Sounding channels detect electromagnetic radiation in narrow bandwidths at frequencies near absorption lines. Imaging channels detect electromagnetic radiation far from absorption lines, in so called "window" channels. Sounding channels allow the ability to detect the amount of water vapor at different layers in the atmosphere while window channels only allow the measurement of integrated atmospheric water vapor. Although these imaging channels are located away from absorption lines the presence or absence of water vapor at these frequencies still has an effect on the spectral opacity of the atmosphere. Figure 1-3 shows a spectral plot of atmospheric attenuation as a function of integrated water vapor content.

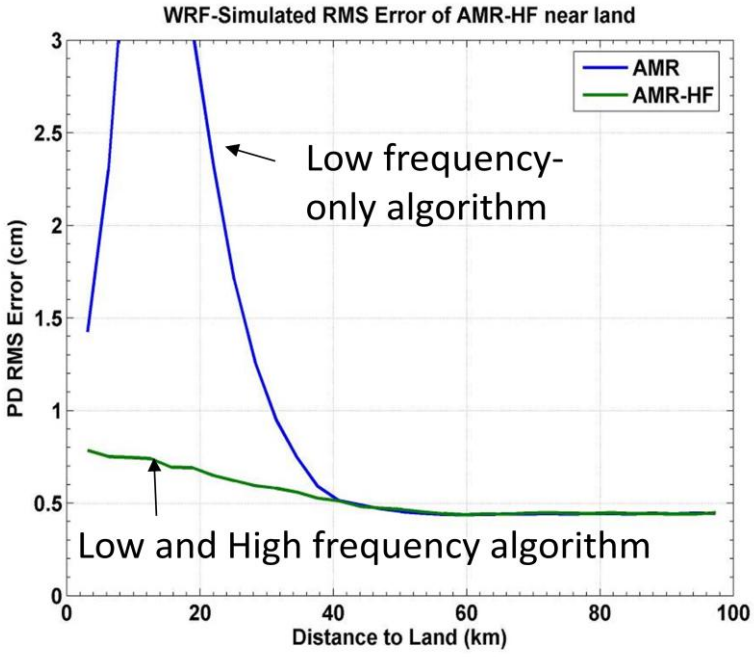

Figure 1-2. Path delay error vs. distance to land [5]

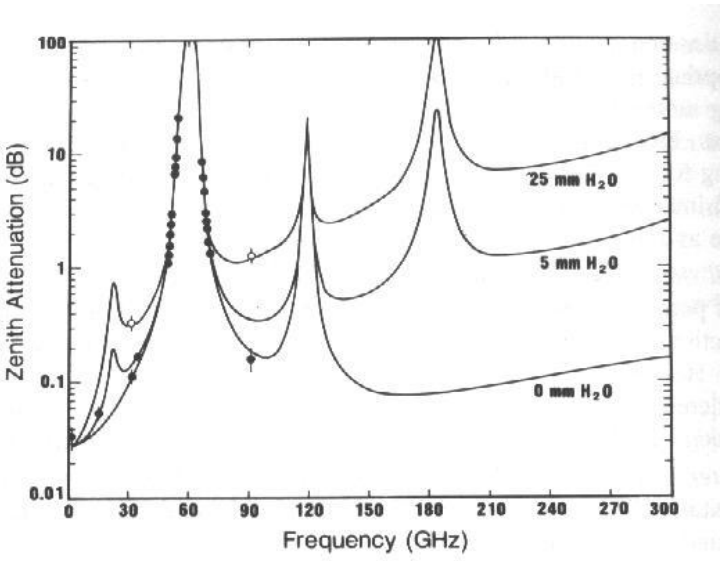

Figure 1-3. Spectrum of atmospheric attenuation for various values of atmospheric integrated water vapor content [1]

1.3 Advanced Component Technology (ACT) Objectives

This thesis work was supported through a NASA Earth Science Technology Office (ESTO) Advanced Component Technology (ACT-08) grant. The objectives for this ACT grant are to develop key radiometer technologies to enable high frequency (90-170 GHz) space borne radiometers in support of the SWOT mission described in Section 1.2. The "big picture" goal is to increase the Technology Readiness Level (TRL) of these components. TRL is a metric that indicates the level of risk associated with deploying a component or system into the field. The key components are a tri frequency feed horn, PIN diode based switches, wide bandwidth noise sources for internal calibration, and a three channel radiometer to demonstrate the functionality of these components in a

realistic system [6]. The demonstration radiometer will be used to develop realistic mass, volume, and power estimates for a space borne system.

1.3.1 Tri-Frequency Feed-horn and Triplexer

A single tri-band feed horn and triplexer is required to maintain acceptable antenna performance since separate feeds for each of the high-frequency channels would need to be moved further off the reflector focus, degrading this critical performance factor. As well, the need for a single antenna for all three channels is motivated by the requirement to have a low mass, and small volume system for future space or aviation deployment. This feed horn must have wide enough bandwidths, greater than 10 GHz, in all three channels. In this ACT bandwidths were defined as the range of frequencies that had return loss measurements greater than 15 dB.

Fabrication of this feed horn, shown in Figure 1-4, which operates at center frequencies of 92, 130, and 166 GHz was completed by NASA's JPL.

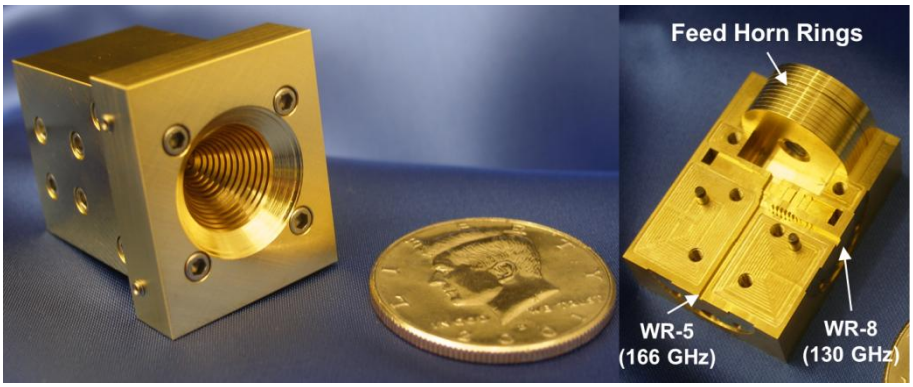

Figure 1-4. Tri-Frequency feed-horn

1.3.2 PIN Diode Switches

PIN diode switches are necessary to switch the receiver input between viewing the antenna and viewing a matched load for internal calibration, or to operate as a Dicke radiometer. Single Pole Double Throw (SPDT) switches have been designed at JPL and fabricated at Northrop Grumman. These switches use Northrop Grumman's InP MMIC PIN diode process to provide low insertion loss, high return loss, and high isolation switching.

1.3.3 Calibration Noise Sources

Traditionally, nadir-pointing radiometers are flown on altimetry missions with no moving parts. Moving parts produce angular momentum that will interfere with vibration sensitive instruments on the satellite. Therefore, external calibration sources, such as the cosmic microwave background radiation, are not available. This lack of external calibration sources forces these radiometers to use internal calibration [7].

For this project, internal calibration was defined as the availability of two calibration points inside the front end of the radiometer, after the antenna. The internal calibration points consist of a matched load and a high excess noise ratio (ENR) noise diode. The definition for ENR is

$$ENR_{dB} = 10\log_{10}[(T_s^{ON} - T_s^{OFF})/T_o] \quad (1\text{-}8)$$

where T_s^{ON} and T_s^{OFF} are the noise temperatures of the noise source in its on and off states, and T_o is the reference temperature of 290 K.

External calibration is defined as one or more calibration points outside of the radiometer system that the antenna views. External calibration points could be a temperature controlled black body, the cosmic microwave background radiation, or an area of the earth with a well characterized emissivity such as the Amazon rain forest [8].

The advantages of internal calibration are a smaller radiometer size and no need for any moving parts. The advantage of external calibration is that every part of the system is calibrated; internal calibration only calibrates out changes after the point at which the calibration temperature is injected.

1.3.4 Demonstration Radiometers

All of these components are integrated into a three channel demonstration radiometer. This three channel radiometer consists of channels centered at 92, 130, and 166 GHz. This radiometer will provide realistic mass and performance estimates for the consideration of SWOT mission planning. A common radiometer back end has also been developed to control each channel and record brightness temperature output data.

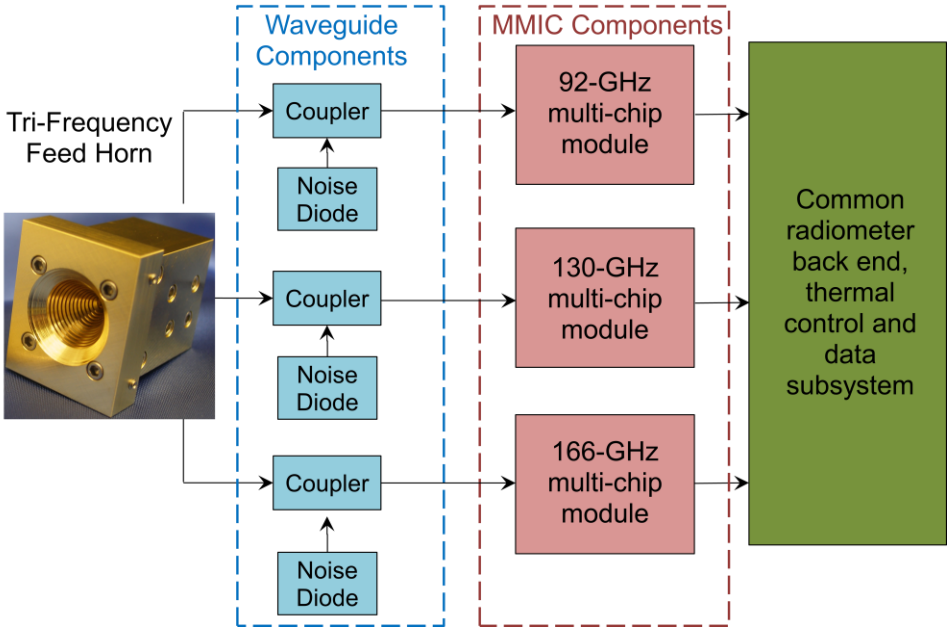

Figure 1-5. Radiometer system block diagram

All three radiometers developed for the SWOT ACT use similar direct detection Dicke architecture. Direct detection indicates the lack of any down conversion in the radiometer. The absence of a mixer and local oscillator reduces the required power, design complexity, mass, and volume of the radiometer. Low power and low mass are critical design requirements necessary to stay within the SWOT mission constraints. Direct detection architecture is made possible by the availability of millimeter-wave low noise amplifiers with significant gain and low noise figures, as well as high sensitivity power detectors.

This thesis discusses the design details, fabrication and measured performance of the 92 and 166 GHz radiometer channels. Details for the 130 GHz channel are presented in Darrin Albers' thesis.

1.4 Dicke Radiometers and Total Power Radiometers

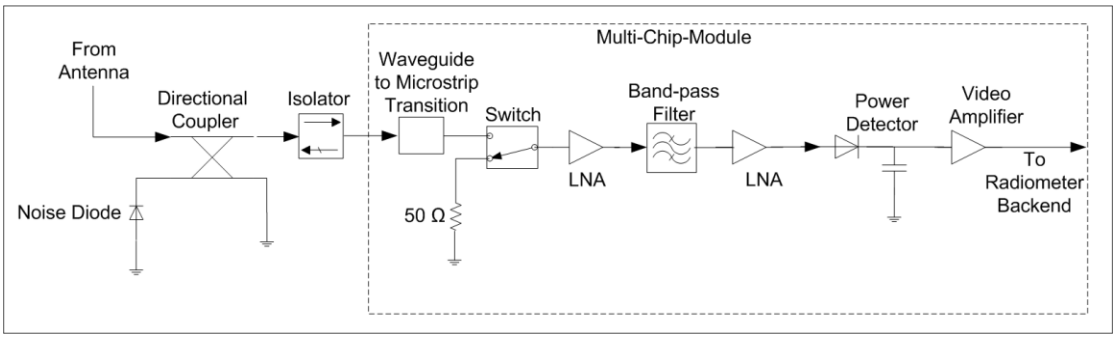

Figure 1-6. 92 GHz block diagram

The block diagram for the 92 GHz radiometer is shown in Figure 1-6. The switch at the beginning of the RF chain allows the radiometer to function as either a Dicke or total power radiometer. When the radiometer is operating in total power mode the switch remains in one position, with the antenna connected to the RF chain. In Dicke mode, the switch alternates between the antenna and matched load at regular intervals. Dicke mode is beneficial because it reduces the effects of gain variations on the system output. The output voltage for a total power radiometer is

$$V_{out\,TP} = kBG\beta(T_A + T_{REC}) + kB\Delta G\beta(T_A + T_{REC}) \tag{1-9}$$

and for a 50% duty cycle Dicke radiometer is

$$V_{out\,Dicke} = kBG\beta(T_A - T_{REF}) + kB\Delta G\beta(T_A - T_{REF}) \tag{1-10}$$

where k is Boltzmann's constant, B is bandwidth, G is RF power gain, β is detector sensitivity in V/W, T_A is the antenna temperature, T_{REC} is the system noise temperature, and T_{REF} is the matched load temperature.

It can be seen that the T_{REC} in the total power equation has been replaced with a $-T_{REF}$ in the Dicke equation. The second term in both equations represents the deviation in output voltage due to gain variations. The $-T_{REF}$ in the Dicke equation reduces the error produced by gain variations since T_{REF} is generally much smaller than T_{REC}. For example, in the 92 GHz radiometer T_{REF} is 300 K while T_{REC} is about 1200 K. If we assume an antenna temperature of 100 K, it can be seen that a total power radiometer will have about 6.5 times more error due to gain variations than a Dicke radiometer with equivalent gain variations. The other benefit of a Dicke architecture is the availability of a resistive matched load for calibration purposes. The matched load can be used as a calibration point with noise temperature equal to the physical temperature of the load. The load needs to be well matched to avoid generation of standing waves.

Dicke architecture reduces the effects of gain variations on the radiometer's output, but the tradeoff is worse radiometric resolution. Radiometric resolution, also known as NEΔT, is defined as the minimum change in brightness temperature at the radiometer's input that will result in a detectable change in voltage at the radiometer's output.

The Dicke architecture affects radiometric resolution in two ways. First, the switch at the input of the receiver will add loss prior to the first LNA. Loss prior to the first gain element substantially increases the system noise temperature, T_{REC}. Second, since the switch is toggled with a 50% duty cycle, only half of the available time is spent looking at the scene temperature. This 50% duty cycle increases the radiometric resolution by a

factor of two compared to that of an ideal total power radiometer. The radiometric resolution for a total power radiometer is

$$NE\Delta T_{TP} = (T_A + T_{REC})\left[\frac{1}{B\tau} + \left(\frac{\Delta G}{G}\right)^2\right]^{\frac{1}{2}} \tag{1-11}$$

and that for a 50% duty cycle Dicke radiometer is

$$NE\Delta T_{DR} = \left[\frac{2(T_A + T_{REC})^2 + 2(T_{REF} + T_{REC})^2}{B\tau} + \left(\frac{\Delta G}{G}\right)^2 (T_A - T_{REF})^2\right]^{\frac{1}{2}} \tag{1-12}$$

When the gain variations are neglected, the total power radiometer's radiometric resolution is at least two times lower than that of the Dicke radiometer. However, as gain variations are increased, the radiometric resolution of the total power radiometer increases much more quickly than that of the Dicke radiometer.

For example, consider a radiometer with a bandwidth of 5 GHz, integration time of 100 ms, and a receiver noise temperature of 1400 K. Ignoring gain variations, the radiometric resolution for a total power radiometer is 0.067 K while the Dicke radiometric resolution is 0.143 K. Now, if we assume gain variations $\Delta G/G$ of 0.0005 and a reference load at a temperature of 300 K, the total power radiometer has a radiometric resolution of 0.75 K while the Dicke has a radiometric resolution of 0.17 K. It is clear that especially as gain variations increase, the Dicke radiometer performance is superior to the total power radiometer in both accuracy and radiometric resolution.

Chapter 2: 92 GHz Radiometer

2.1 Radiometer System Overview

The 92 GHz channel was the first radiometer designed as part of this work. Since this radiometer design occurred in the early stages of this project, some of the JPL designed components were not able to be used and had to be replaced with commercially available components. All of the active components used in this design are commercially available components.

The block diagram for this radiometer can be seen in Figure 1-6 [9] [10]. As previously mentioned, this design uses a Dicke-switched, direct detection architecture. Table 2-1 shows the component manufacturers, part numbers, gain, noise figure, and cumulative system noise temperature for the initial 92 GHz design. Several design changes were implemented and are discussed in Section 2.5. The loss specified on the components' data sheets, as opposed to the measured loss, was used to determine the required gain and to calculate the expected system noise temperature. The predicted noise temperature can be used to calculate the predicted system radiometric resolution.

2.1.1 Predicted Gain Requirements

The system gain requirement is driven by three constraints. First, the detector diode must remain in the square law region of detection. For a large range of input power levels a diode output voltage is given as

$$V_{out} = K * \left(\sqrt{P_{in}}\right)^{\alpha} \quad (2\text{-}1)$$

[11]. For low input powers, up to about –20 dBm, α is equal to two [11]. This region is referred to as the square law region where the output voltage is linearly proportional to the input power. This linearity is extremely important; all measurements made with the radiometer assume that the detector is operating in the square law region. The square law region enables a two point radiometer calibration. The power detector used in this design will remain in the square law region with input signals as large as –30 dBm.

Secondly, the input signal must remain above the noise floor of the detector, about –60 dBm.

Lastly, larger signals will result in a higher signal to noise ratio at the output of the detector and provide greater immunity to noise interference. For example, if the detector has a sensitivity of β = 15,000 V/W and the input signal is –50 dBm, the output voltage will be approximately 150 μV. If the same detector is used with an input signal of –32 dBm the output voltage will be approximately 10 mV. Detecting microvolt level signals

presents a number of problems, including very high sensitivity to noise that is coupled onto the line and offset voltages caused by non-idealities in operational amplifiers.

Due to these three constraints, it would seem that the ideal design would have enough gain so that the largest input signal will be just at the edge of the detector's square law region. However, due to the statistical nature of noise, the ideal signal is about 10 dB below the square law region of the detector, which is –40 dBm for the detector in the 92 GHz radiometer. The power delivered to the detector, in dBm, can be calculated as

$$P_{detector}(dBm) = 10 * \log\left\{\frac{k * (T_A + T_{REC}) * B * G}{10^{-3}}\right\} \quad (2\text{-}2)$$

In order to minimize the chip count, power consumption, and likelihood of amplifier oscillations, only one LNA was originally used in this design. The largest expected signal in the 92 GHz radiometer is the noise diode calibration point, around 580 K. The system noise temperature with only one LNA is predicted to be 727 K, the gain is 25 dB, and the bandwidth is 5 GHz. The power delivered to the detector was calculated to be –45 dBm using Equation (2-2), with T_A equal to 580 K. The average detector sensitivity across the radiometer's bandwidth is approximately 13,500 V/W. A –45 dBm input power results in a 400 μV signal at the detector output. Detecting this small output voltage presented problems that necessitated changes in the radiometer architecture. These changes are discussed in Section 2.5.

Table 2-1. Preliminary single LNA 92 GHz design noise analysis

Component	Vendor	Part Number	Gain (dB)	Noise Figure (dB)	Cumulative Noise Temperature
Directional coupler	Dorado	DCG-10-10E	-0.50	0.50	35
Isolator	Raditek	RADI-75-110-WR10	-0.50	0.50	75
Waveguide to microstrip transition	MSL	-	-0.25	0.25	97
Switch	M/A-Com	MA4GC6773	-1.20	1.20	220
LNA	HRL Labs	LN5-100	29.00	3.00	727
BPF	MSL	-	-1.50	1.50	727
Receiver gain (dB)	25.1				
Receiver noise figure (dB)	5.5				
Receiver noise temperature (K)	727.4				

2.1.2 Predicted System Noise Temperature

System noise temperature is a very important metric of any receiver system. It is especially important in radiometry because it directly relates to the system's radiometric resolution, see Equation (1-12). A large system noise temperature gives a larger, i.e. worse, radiometric resolution. The system noise temperature can be calculated using the cascaded noise temperature equation [12]

$$T_{sys} = T_1 + \frac{T_2}{G_1} + \frac{T_3}{G_1 G_2} + \cdots \tag{2-3}$$

where $\{T_1, T_2, T_3\}$ and $\{G_1, G_2, G_3\}$ are the noise temperatures and gains of the first three components in the RF chain, respectively. The predicted system noise temperature is 727 K. The corresponding radiometric resolution is shown as a function of integration time in Figure 2-1. This radiometric resolution plot assumes a Dicke mode of operation, an antenna temperature of 100 K, and normalized gain variations, $\Delta G/G$, of 0.0005, as

measured for the Compact Microwave Radiometer for Humidity (CMR-H) profiling at CSU [13].

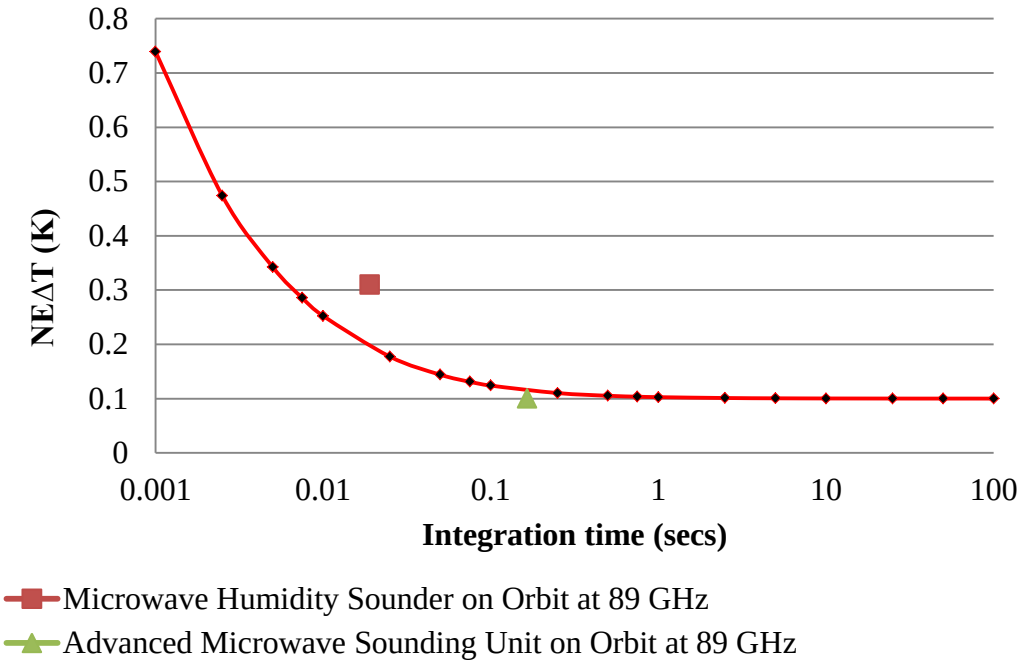

Figure 2-1. Initial 92 GHz design, predicted radiometric resolution

2.2 92 GHz Component Design and Measurement

2.2.1 Custom Designed Passive Components

The following passive components were all designed, simulated, and tested at the Microwave Systems Laboratory (MSL) by graduate students. They were fabricated at Applied Thin Film Inc. (ATP) on 5 mil thick polished alumina substrates. Alumina was used due to its low cost, low loss, low coefficient of thermal expansion, and its long history of successful use in MMIC circuits. The loss tangent, tan δ, of alumina is

approximately 0.0001. An alternative low loss dielectric material is quartz, which has a lower relative permittivity than alumina. Polished alumina is used to reduce the surface roughness, and thus the loss, of the substrate. The thickness of the substrate is important to consider at these frequencies. If the substrate is too thick, it can act as a parallel plate waveguide, generating higher order modes between the metalized surface and ground plane, causing loss and distortion, as discussed in Section 3.2.1. All of the 92 GHz designs used gold metallization with a thickness of 0.125 mils.

2.2.1.1 Bandpass Filter

The bandpass filter defines the bandwidth over which the radiometer will sense electromagnetic radiation. It has an effect on the power level at the input to the power detector, as shown in Equation (2-2), and on the radiometric resolution of the receiver, as shown in Equation (1-12).

The bandpass filter is a fifth order Butterworth filter. It uses an edge coupled microstrip topology to allow the filter to be easily wire bonded to the other components. Increasing the filter order increases the out of band rejection. However, the physical size and complexity of the filter also increase as well as the difficulty of tuning the design. A fifth order filter was deemed to be the best compromise among out of band rejection, filter size, and design complexity. During the design phase, Chebyshev filters with 0.5 dB and 0.1 dB ripple in the passband and Butterworth filters with maximally flat response in the passband were compared, as shown in Figure 2-2 and Figure 2-3. A Butterworth design was chosen for a maximally flat filter response in the pass band. A Chebyshev design was

considered to maximize out of band rejection. It was decided that the improvement in out of band rejection was not worth the additional loss or ripple in the pass band.

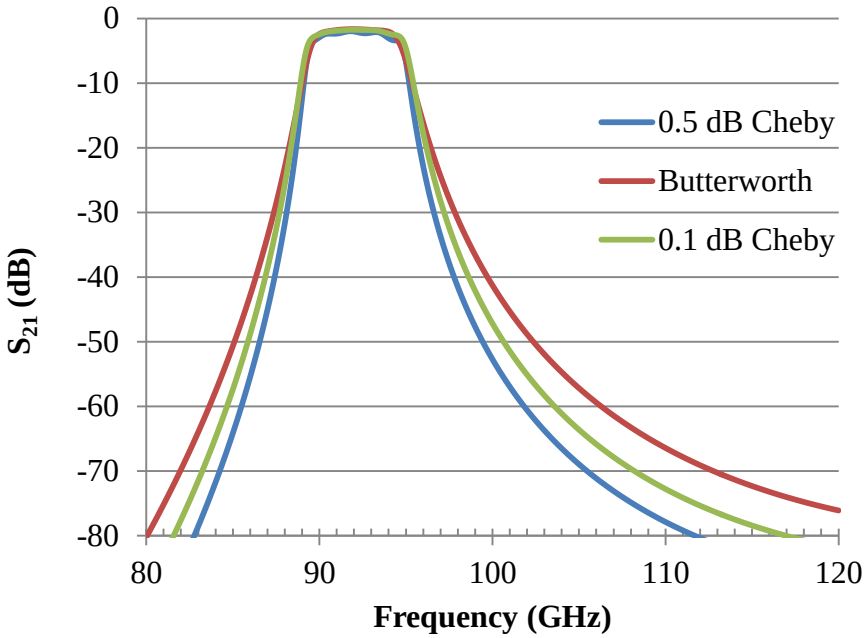

Figure 2-2. Comparison of ideal bandpass filter simulated responses

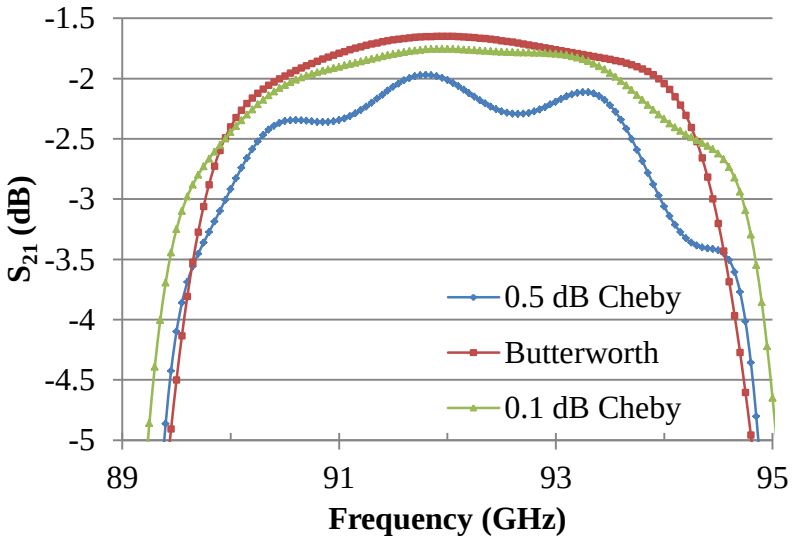

Figure 2-3. Narrow band ideal bandpass filter response comparison

An iterative design process was used for the filter design. The initial design was created using hand calculations and element values from [14]. This design was then verified using Ansoft Designer, an analytical circuit simulation tool. This tool uses equivalent circuit models of each transmission line element; it is limited in the types of circuits that can be simulated. Next, the design was analyzed using Ansoft's Planar EM, a 2.5D simulation tool. The 2.5D tool allows the user to define different homogenous layers at different heights in the simulation space. Each layer consists of only one material; the user is able to specify the material properties, thickness, and a layout pattern for each layer. The 2.5D tool also allows the design to be simulated in a cavity. Figure 2-4 shows the 2.5D model used for this filter. Finally, the design was simulated using Ansoft's HFSS, a full wave 3D Finite Element Method (FEM) simulation program. HFSS allows the user to create a complete 3D model of the design using as many different materials as the user would like. Figure 2-5 shows the HFSS 3D model that was used for this filter. Each step in the design process used a more complicated tool than the previous step. More complicated tools require more computation time and model setup time.

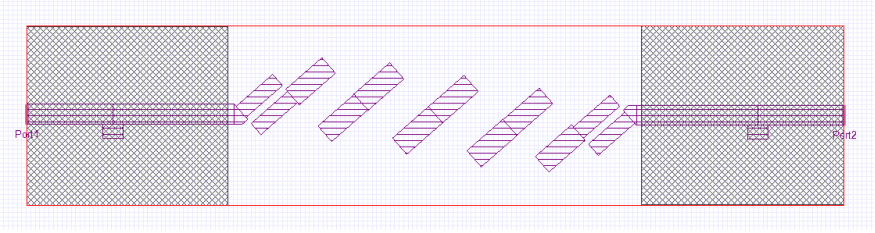

Figure 2-4. 92 GHz 2.5D filter model

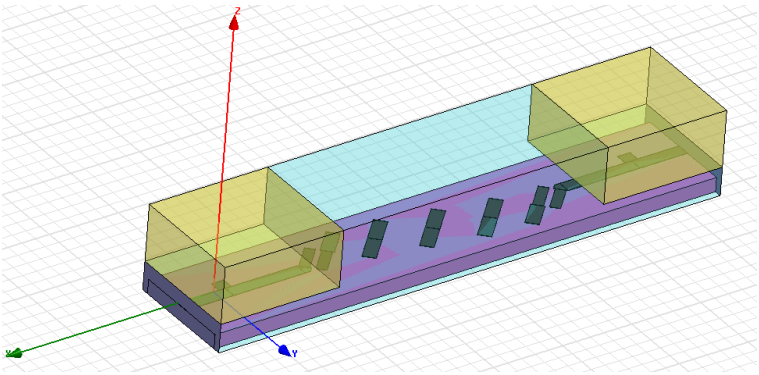

Figure 2-5. 92 GHz HFSS 3D filter model

For later designs, the optimization tool in HFSS was used to properly tune the filter. However, on this design all of the tuning had to be done by hand. Tuning the filter by hand is very time consuming, and is not recommended. The difficulty of hand tuning the filter increases with higher frequencies, i.e. decreasing wavelength. This is because of the higher sensitivity to error when the wavelengths become small. The wavelength in alumina for this filter is 41 mils (1 mm). After many hours of hand tuning, the filter's return loss response was still not acceptable. The final tuning of the return loss was achieved by adding an open circuit stub matching network on either side of the filter. Even with the matching network, there was an unacceptable level of ripple in the return loss pass band. This ripple is believed to be due to coupling between the filter's resonators and the matching network's open circuit stubs. In order to reduce the coupling, the lid height over the open circuit stubs was reduced to 5 mils above the substrate. This can be seen by the gold rectangular prisms in Figure 2-5. In the final design, the return loss performance was acceptable. Figure 2-6 shows insertion loss and return loss values simulated in HFSS. The 3 dB bandwidth is 6.9 GHz, with a center frequency of 92 GHz.

Within the 3 dB filter bandwidth, the average insertion loss is 1.56 dB, and the average return loss is 22 dB.

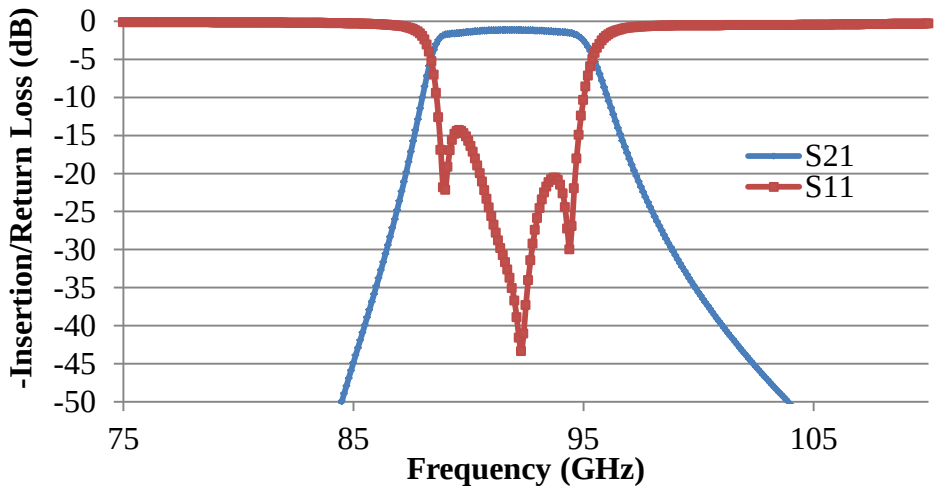

Figure 2-6. HFSS 92 GHz filter simulation results (in cavity)

The filter was measured in open air with an Agilent Technologies Vector Network Analyzer and Cascade Microtech probe station. The network analyzer, an Agilent E8364B, included 100 GHz frequency extension options and a set of OML Waveguide extender heads, model V10VNA2. J micro Technology coplanar to microstrip transitions were wire bonded at either end of the filter to allow the Cascade Microtech probes to interface with the filter. A photograph of the filter is shown in Figure 2-7. The open air filter measurement response is shown, Figure 2-8 and Figure 2-9, in comparison with the HFSS open air simulation. It can be seen that the open air measurement agrees very well with the HFSS open air simulation.

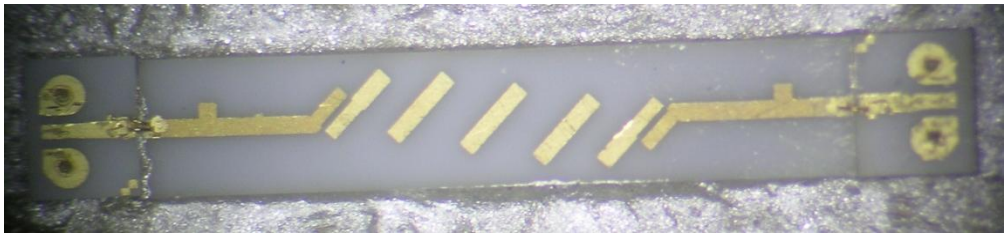

Figure 2-7. 92 GHz bandpass filter

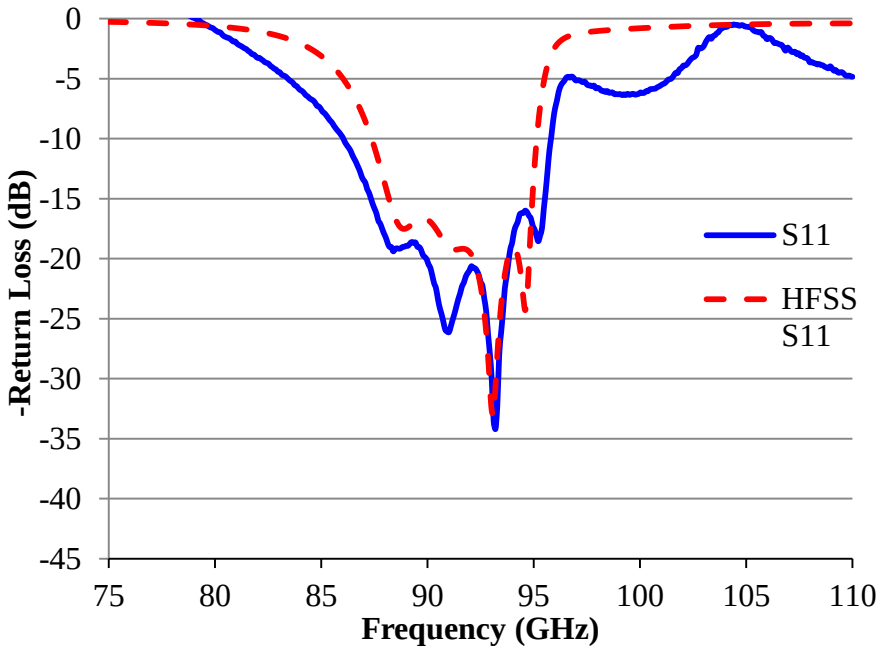

Figure 2-8. Comparison of 92 GHz bandpass filter simulated and measured return loss

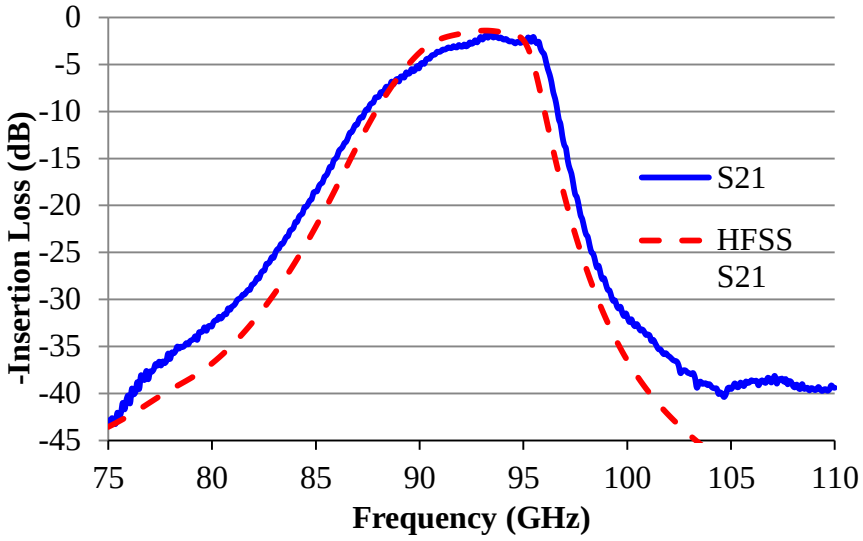

Figure 2-9. Comparison of 92 GHz bandpass filter simulated and measured insertion loss

The height of the lid above the filter has a significant impact on filter response, as can be seen by comparing the open air HFSS simulation results above with the cavity simulation results. Therefore, it was decided to design a fixture to test the filter response in a cavity identical to the cavity of the MCM. This would allow the bandwidth of the filter to be directly measured as opposed to extrapolating what the filter's performance in a cavity would be based upon open air measurements. A component level block diagram of the test fixture is shown in Figure 2-10; an image of the RF trench in the assembled test fixture is shown in Figure 2-11. The measured results are shown in Figure 2-12 and Figure 2-13.

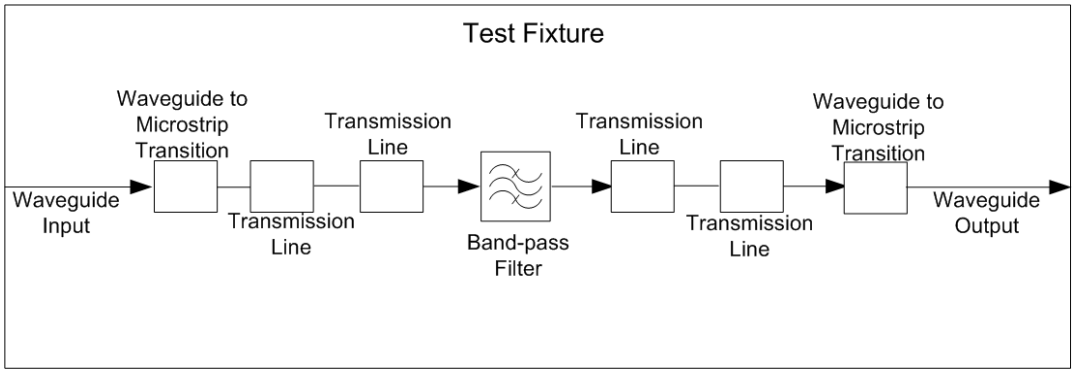

Figure 2-10. Test fixture block diagram

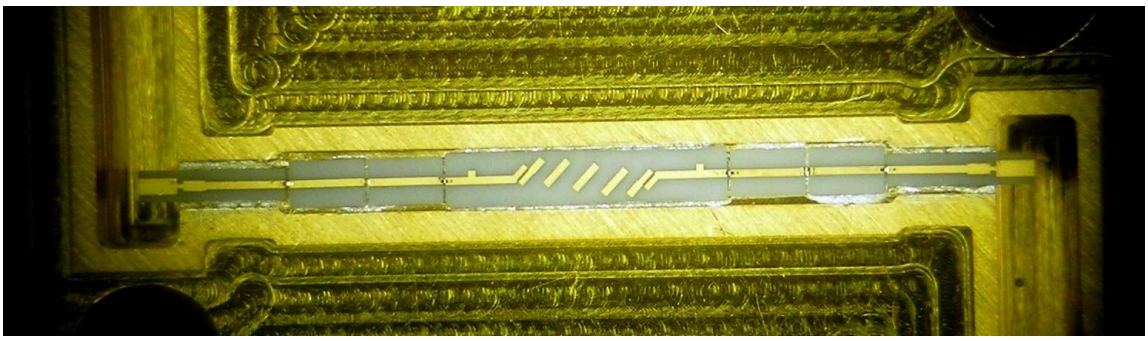

Figure 2-11. The bandpass filter test fixture's RF trench

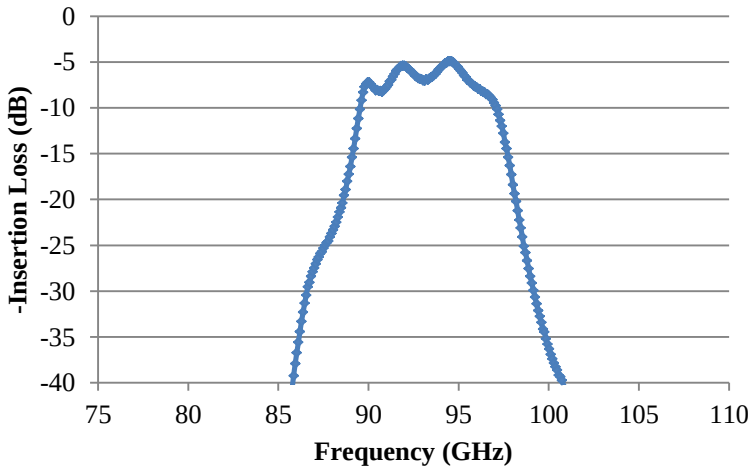

Figure 2-12. Measured filter insertion loss in the test fixture

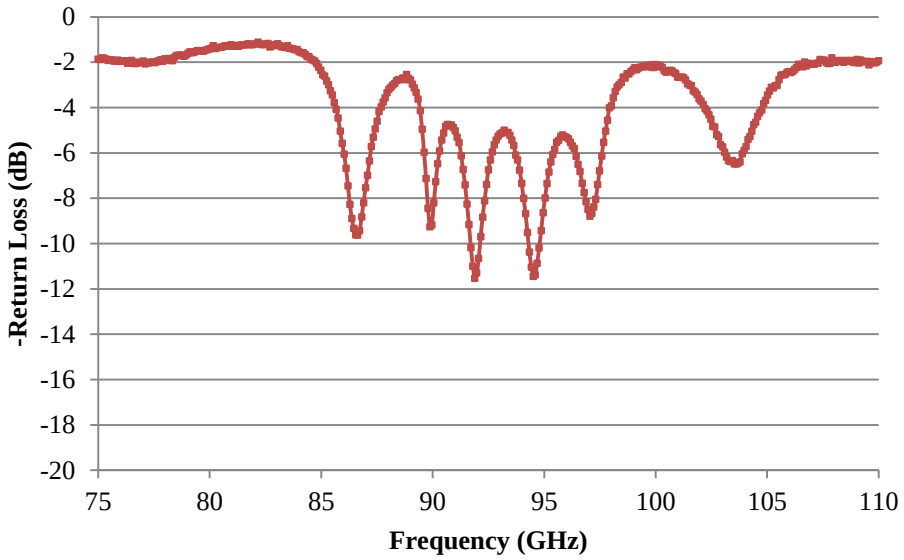

Figure 2-13. Measured filter return loss in the test fixture

As can be seen from the measured response plots, there is considerably more ripple and insertion loss in the measured test fixture response than in any of the other simulated or measured data. It is difficult to determine what is causing this ripple, but it is believed to be due to the number of wire bonds. An HFSS simulation of the test fixture setup was performed and compared with the measured response; it is shown in Figure 2-14 and Figure 2-15.

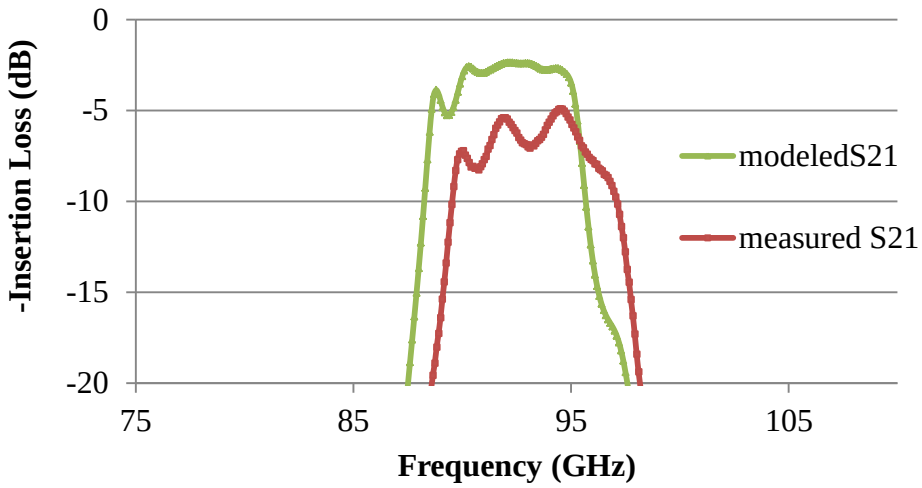

Figure 2-14. Simulated vs. modeled test fixture performance

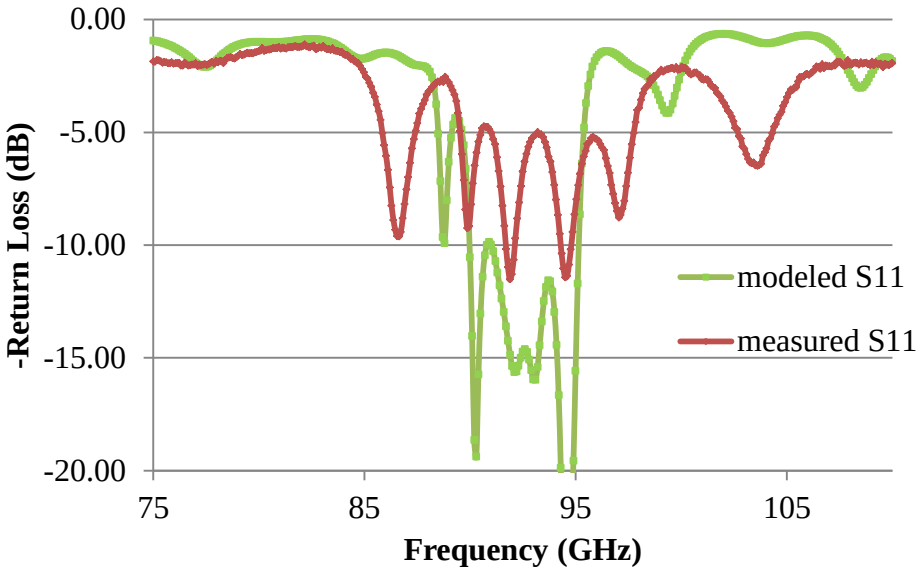

Figure 2-15. Simulated vs. modeled test fixture performance

It can be seen that simulating the test fixture with all of the components and wire bonds adds some ripple to the response but still does not match well with the measured performance. The measured performance has about 3 dB more insertion loss and about 5

dB less return loss. It is difficult to determine what is causing this performance degradation due to the number of unknowns in the system. If another test block were designed, it would be better to minimize the number of wire bonds, thereby reducing the number of unknowns. A better design would have been smaller, only including a waveguide-to-microstrip transition input, a band pass filter, and a waveguide-to-microstrip transition output.

2.2.1.2 Matched Load

The matched load is used as a calibration reference. This load is precisely temperature controlled to maintain a constant reference noise temperature. The load is well matched to eliminate generation of standing waves. The matched load uses a quarter wavelength open-circuited stub with a characteristic impedance of 50 ohms, known as a virtual ground, to provide an RF ground over the bandwidth of interest. This design eliminates the need for vias, which have a high parasitic inductance at these frequencies. The resistor itself is composed of Tantalum Nitride, TaN, deposited via a thin film sputtering process. The resistance is 25 ohms per square; the dimensions of the resistor are 4 mils (0.10 mm) long by 2 mils (0.05 mm) wide for a total resistance of 50 ohms. There is a short length of microstrip line with characteristic impedance of 50 ohms at the input of the load for wire bonding purposes.

The matched load was simulated in Ansoft HFSS. The 3D model is shown in Figure 2-16. The resistor was modeled using a 2D impedance boundary, represented in red in the model.

The matched load was measured in open air using the same test setup as the bandpass filter. A J micro Technology coplanar to microstrip transition was wire bonded to the input to allow the probe station to interface with the component. A photograph of the component is shown in Figure 2-17. A comparison of simulated and measured results is shown in Figure 2-18.

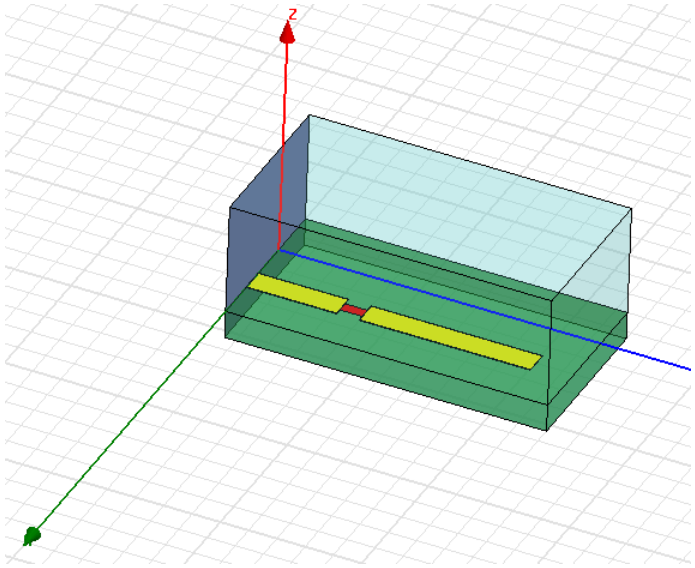

Figure 2-16. HFSS 3D model of the 92 GHz matched load

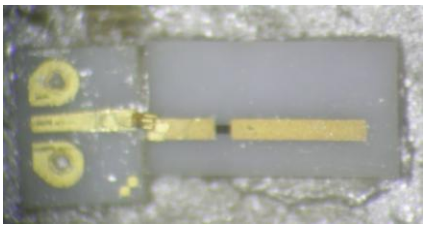

Figure 2-17. Custom designed matched load

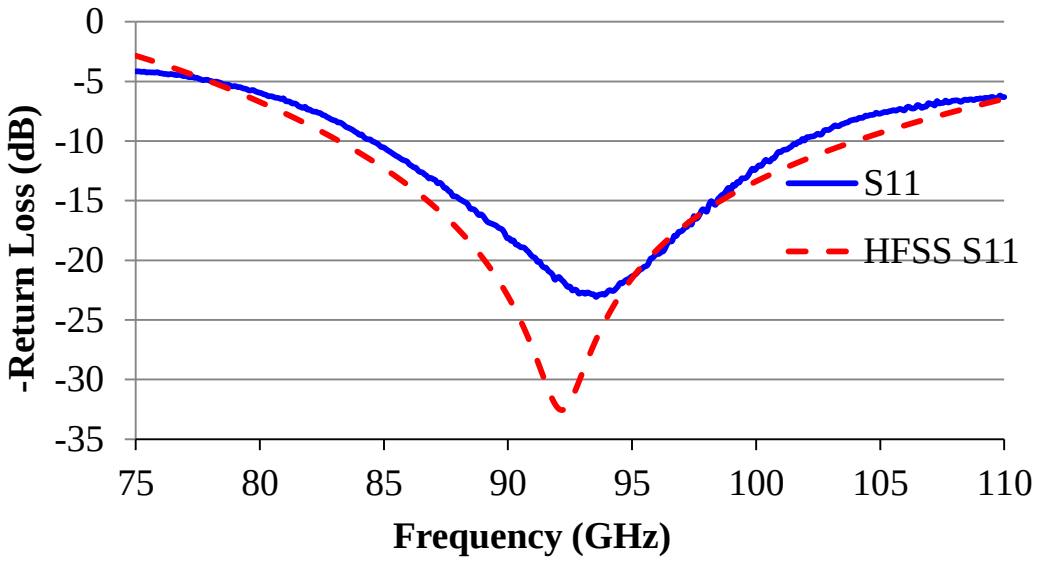

Figure 2-18. Comparison of simulated and measured performance for the 92 GHz matched load

2.2.1.3 Waveguide-to-microstrip transition

The waveguide-to-microstrip transition acts as a low loss pathway to convert the electromagnetic energy from a rectangular waveguide mode of propagation to a microstrip mode of propagation. This is necessary to interface the waveguide based components, i.e. the antenna, coupler, and noise source, with the microstrip and MMIC based components in the MCM. The transition needs to be low loss and well matched over the bandwidth of the radiometer.

The design for the waveguide-to-microstrip transition is based upon the E-plane probe design presented in [15]. The microstrip probe enters the waveguide via a window on the broad wall of the waveguide, as shown in the HFSS model in Figure 2-19. The

waveguide ends in a short circuit, known as a backshort, some distance past the point where the transition intersects the waveguide; the distance between the waveguide-to-microstrip transition and the short circuit is referred to as the backshort distance. The transition consists of two sections, first a large probe on the portion of the substrate that lies in the waveguide, and second, a microstrip matching network consisting of a small high impedance section, a quarter wave transformer, and a 50-ohm line. The underside of the probe section has no metallization, while the rest of the substrate has a metal layer on the underside. There is a combination of probe widths, probe lengths, and back short distances that result in a constant impedance with frequency at the output of the probe section. These variables, i.e. probe width, length, and backshort distance, were tuned until constant impedance was obtained over the frequency band of interest. The constant impedance had a capacitive component that was canceled by the high impedance section to give a purely real impedance at the output of the high impedance section. The real impedance was then transformed to 50 ohms using the quarter wave transformer. This is matched to a 50-ohm line connected to the output of the transition. The transition was simulated using Ansoft HFSS. This component was not measured directly because of problems with measuring cavity based components, as mentioned in Section 2.2.1.1. The HFSS simulation results are shown in Figure 2-20 and Figure 2-21. A photograph of the waveguide-to-microstrip transition is shown in Figure 2-22.

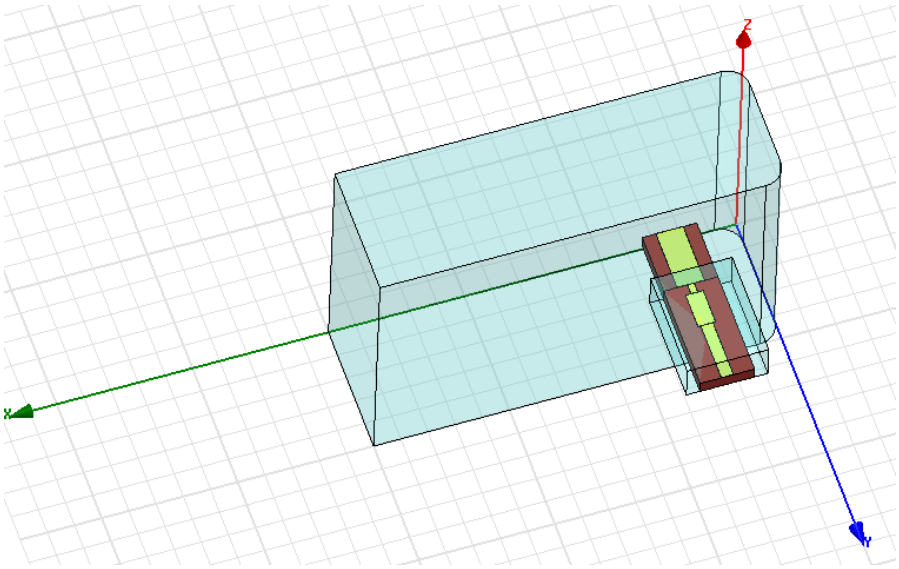

Figure 2-19. HFSS model of 92 GHz waveguide-to-microstrip transition

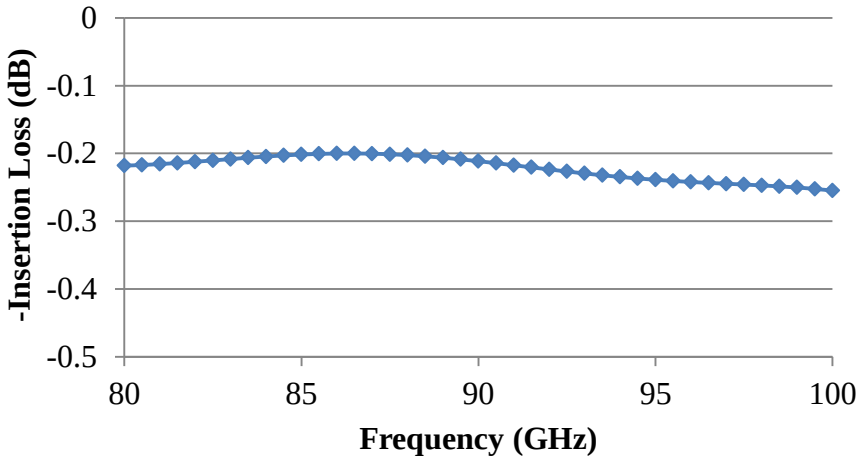

Figure 2-20. Simulated waveguide-to-microstrip transition insertion loss

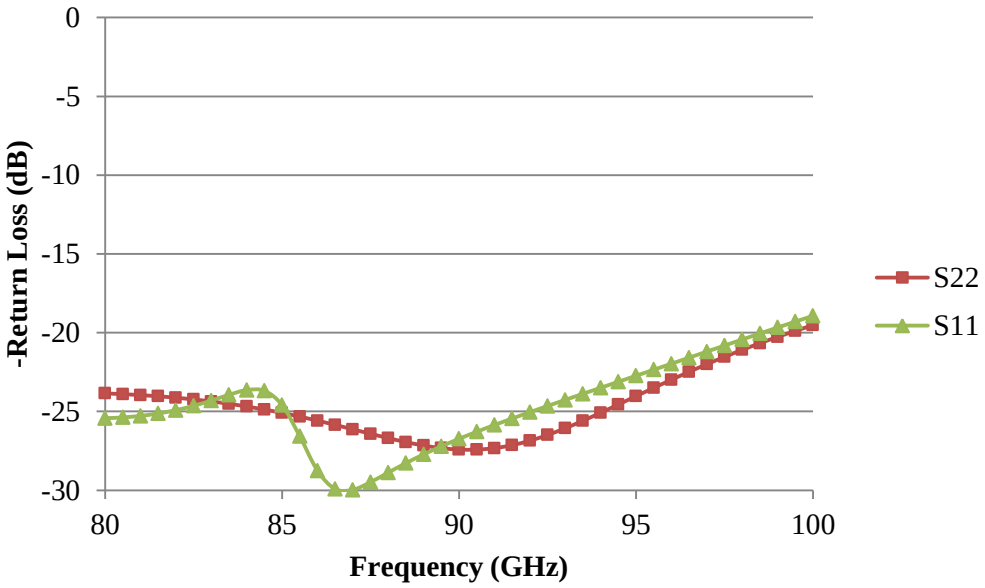

Figure 2-21. Simulated waveguide-to-microstrip transition return loss

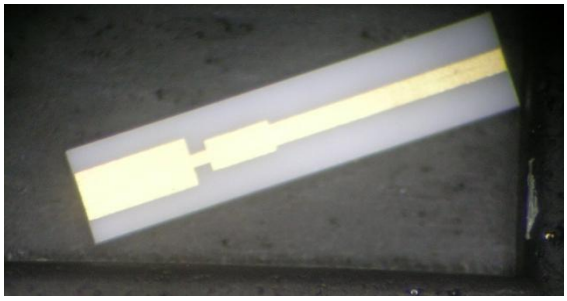

Figure 2-22. Photograph of 92 GHz waveguide-to-microstrip transition

2.2.2 Commercially Available Components

Commercially available components were used for the waveguide based components and all of the MMIC components for the 92 GHz radiometer.

2.2.2.1 92 GHz Low Noise Amplifier

The Low Noise Amplifier (LNA) used in this design is the HRL Laboratories LN5-100. This LNA is a five stage indium phosphide (InP) high electron mobility transistor (HEMT) based design. The LNA has a data sheet specified gain of 29 dB and a 3 dB noise figure from 70-100 GHz. The LNA has separate gate bias lines for the first transistor stage and the subsequent stages to allow the user to optimize the amplifier's noise performance. These LNAs were chosen due to their high gain, low noise figure, and HRL's willingness to donate these MMICs. These are depletion mode devices, meaning that negative gate bias voltages are used; they use a drain voltage of 1.25 V.

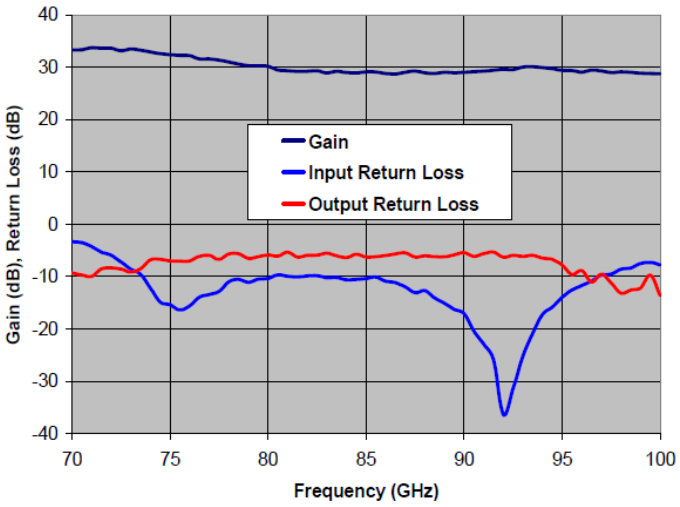

Figure 2-23. 92 GHz low noise amplifier performance specified by HRL

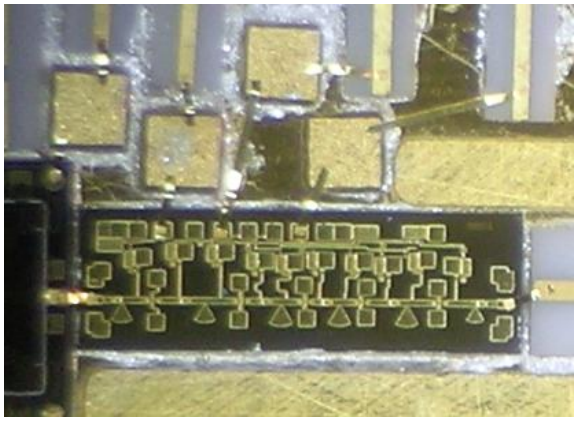

Figure 2-24. 92 GHz low noise amplifier, HRL LN5-100, as mounted in the MCM

2.2.2.2 92 GHz Power Detector

HRL Laboratories V1A square law detector is used for power detection in the 92 GHz receiver. This detector is optimized for a similar bandwidth as the 92 GHz LNA, 90-95 GHz. This detector has an extremely high sensitivity of approximately 15,000 V/W between 90 and 95 GHz. The detector operates in the square law region below input powers of –30 dBm. Performance plots for this component are shown in Figure 2-26 and Figure 2-27.

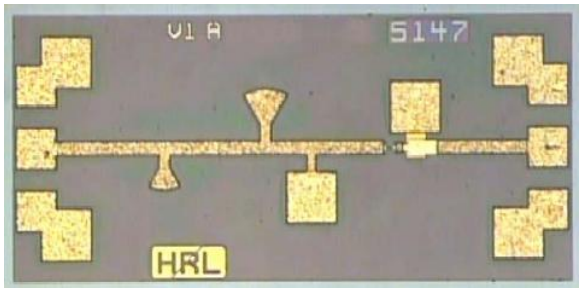

Figure 2-25. 92 GHz power detector, the HRL V1A

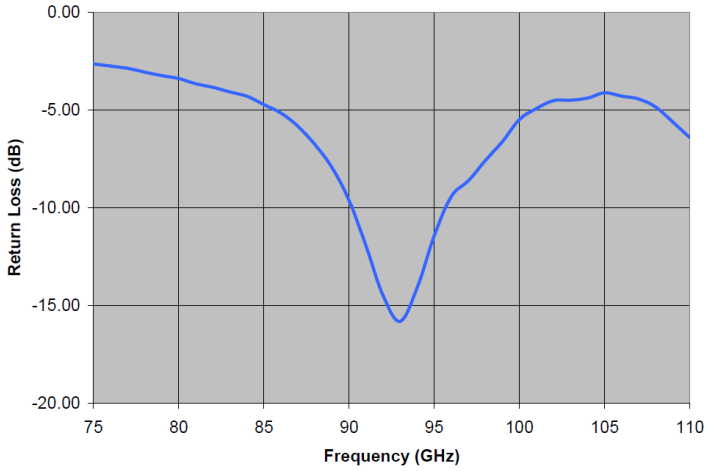

Figure 2-26. 92 GHz power detector's return loss response measured by HRL

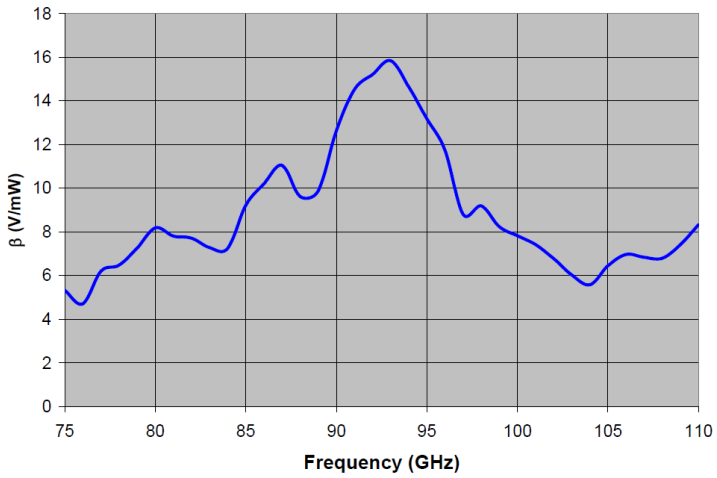

Figure 2-27. 92 GHz power detector's sensitivity as a function of frequency measured by HRL

This component was a major reliability problem in the radiometer due to voltage transients coming from the post detection video amplifier, as discussed in Section 2.4. When this component was suspected of being damaged, it was important to determine whether or not it was actually destroyed prior to removing it. The detector functionality

can be assessed by measuring the DC I-V curve and comparing it to the plot supplied by the component's manufacturer, shown in Figure 2-28. The input section of the detector is a DC ground. The I-V curve can be obtained by grounding a test voltage source to the chassis and applying a negative and positive voltage to the output of the chip while monitoring the test voltage source's current. The diode's cathode is connected to the output of the detector chip, and at low frequencies its anode is connected to the detector ground. When a negative voltage is applied to the output of the chip, a relatively large diode forward current will flow, as shown in Figure 2-28. Therefore, when a positive voltage is applied to the output, a very small reverse current will flow, due to diode leakage current.

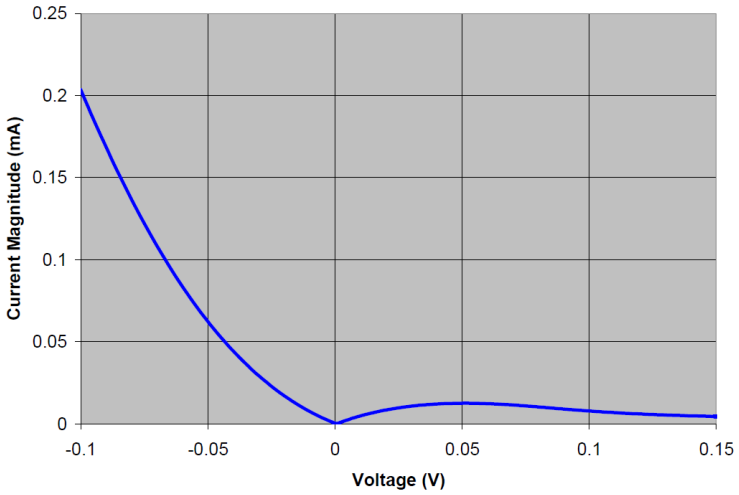

Figure 2-28. DC I-V characteristics of the 92 GHz power detector, the HRL V1A

2.2.2.3 92 GHz Dicke Switch

The Dicke switch is used to switch the front end of the radiometer between the antenna and the matched load. This switch must provide low insertion loss, high isolation, and a good match. In addition, it needs to have a nearly identical response in both switch positions. Since this switch is located prior to the first gain stage, any loss will have a significant impact on system noise figure and radiometric resolution. If the switch's isolation is not high enough, error will be added to the radiometer measurements from either the matched load when viewing the antenna or from the antenna when viewing the matched load.

As part of the ACT project, JPL designed several PIN diode switches including one optimized for the 92 GHz radiometer band, discussed in Section 2.2.3.1. Due to the long lead times associated with wafer foundry fabrications, the JPL switch was not able to be used in this radiometer. A commercially available SPDT switch optimized for use in the 92 GHz frequency band was not available at the time of fabrication of the 92 GHz radiometer. As a compromise, the M/A-Com MA4GC6773 switch was used for the 92 GHz Dicke switch. This switch's datasheet specifies operation up to 77 GHz. The switch's data sheet specifies 1.2 dB insertion loss, 24 dB isolation, and 15 dB return loss at 77 GHz.

The switch was measured in open air with the same test equipment as the thin film components. Several additional thin film components were used to interface the probe station with this chip's port locations and to terminate the unused port. These additional

components are straight and curved 50-ohm lines, a matched load, and a J micro Technology ground-signal-ground (GSG) transition. The measured response and a photograph of the test setup are shown in Figure 2-29 through Figure 2-31. The measured results include uncertainties due to the additional thin film components and the wire bonds. The average insertion loss and return loss measured across the bandwidth of the radiometer are 3.55 dB and 15.3 dB, respectively.

The switch is controlled with two complementary ± 5V control signals, with a current of 10 mA.

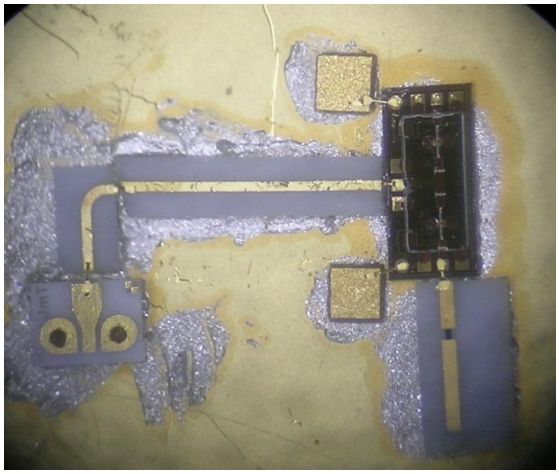

Figure 2-29. 92 GHz Dicke switch test setup

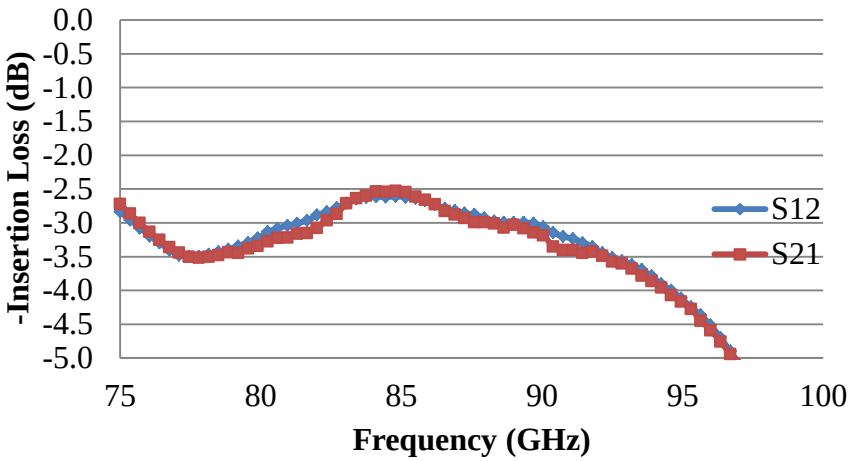

Figure 2-30. Measured 92 GHz switch insertion loss

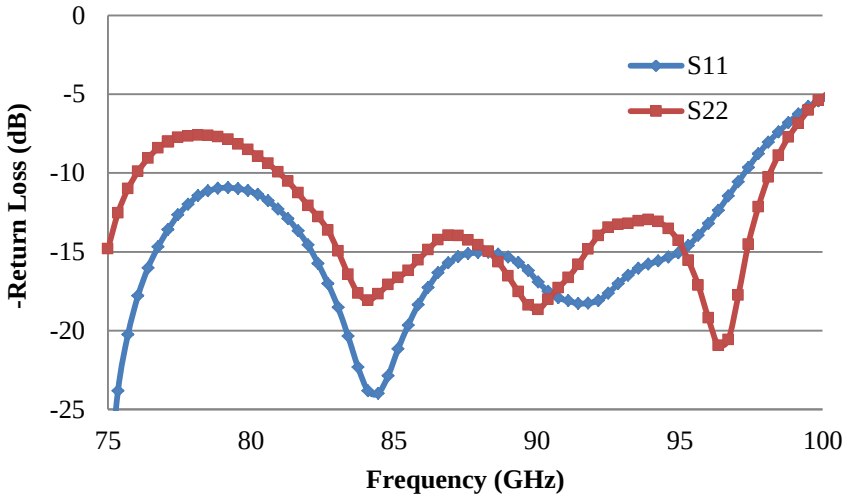

Figure 2-31. Measured 92 GHz switch return loss

2.2.2.4 92 GHz Coupler

The coupler is used to inject the noise diode signal into the receiver front end. The coupler needs to be low loss, provide a good match, and high directivity. The coupler used in the 92 GHz radiometer is the ELVA DC-10. The coupler has a data sheet

specified insertion loss of 1.2 dB. It has a specified return loss of 23.1 dB, and a directivity of 30 dB. These performance parameters are specified in the WR-10 waveguide band of 75-110 GHz.

Instead of a coupler, a switch could be used to inject the noise diode signal into the radiometer front end. This could be a second SPDT switch located closer to the antenna than the Dicke switch. This could also be a single pole triple throw (SPTT) switch, switching the radiometer input between the reference load, a noise diode, and the antenna. A second SPDT switch is not a good option because of the added loss prior to the first gain stage. A SPTT switch could work well but would add complexity to the MCM design. It would also necessitate fabricating a microstrip based substrate with an integrated matching network and pads for mounting the noise diode. This would ensure that the noise diode is well matched and would easily interface with the other microstrip and MMIC based components. Another potential issue with a SPTT switch is that different switch positions could present different impedances to the input of the low noise amplifier. These different impedances cause gain and noise figure changes in the amplifier. An isolator placed between the switch and the LNA can be used to solve this problem. However, microstrip-based isolators are not available at these frequencies.

Coupler insertion loss is defined as

$$I.L._{dB} = -10\log[(P_2 + P_3)/P_1] \tag{2-4}$$

Equivalently, the insertion loss is the ratio of the sum of the received powers at the through and coupled ports to the injected power at the input port, using the port

numbering shown in Figure 2-32. It is important to note that any noise added to the system due to the coupler will be due only to the insertion loss. The power that is coupled away will reduce the signal level at the through port but will not affect the receiver noise temperature.

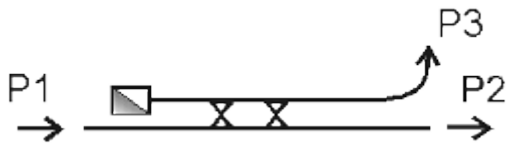

Figure 2-32. Generic coupler schematic showing port numbering [16]

Coupler directivity is defined as

$$Directivity_{dB} = -10\log[P_3/P_2] \tag{2-5}$$

Equivalently, the directivity is the ratio of the power received at the coupled port to the power injected at the through port, using the port numbering shown in Figure 2-32. In an ideal coupler the directivity is infinite, since port 3 is perfectly isolated from port 2.

Because the noise diode output is coupled into the radiometer, both the coupling factor and the antenna temperature affect the power received from the noise diode. For example, referring to Figure 2-32, consider the equivalent temperature at P1 of a lossless coupler with P2 connected to an antenna and P3 connected to a noise diode. The equivalent temperature at P1 of the coupler is

$$T_{out,lossless} = (1 - C)T_A + C \cdot T_{ND} \tag{2-6}$$

where T_A and T_{ND} are the equivalent temperatures due to the antenna and noise diode, respectively, and C is the coupling factor, in linear units. It is clear that the equivalent temperature at the output of the coupler, and therefore the noise diode calibration point, depends upon T_A. We define the noise deflection as the difference between the coupler output with the noise diode on and with the noise diode off, assuming T_A is constant over the measurement. The deflection temperature is independent of T_A *as*

$$T_{deflection,lossless} = C(T_{ND\_ON} - T_{ND\_OFF}) \tag{2-7}$$

where T_{ND_ON} and T_{ND_OFF} are the equivalent temperatures of the noise diode output when the noise diode is on and off, respectively. Noise deflection at the output of a coupled noise source is a more useful term than equivalent temperature, since noise deflection is independent of T_A. Equations (2-6) and (2-7) can be modified to include lossy couplers

$$T_{out,lossy} = ((1 - C)T_A + C \cdot T_{ND} + T_E)G \tag{2-8}$$

$$T_{deflection,lossy} = GC(T_{ND\_ON} - T_{ND\_OFF}) \tag{2-9}$$

where T_E is the equivalent input referred noise temperature of the coupler due to its insertion loss, and G is the gain of the coupler, equal to the reciprocal of its insertion loss.

As can be seen using Equations (2-4) through (2-7) above, a tradeoff exists between the coupling factor and the required noise diode performance. For example, after considering system dynamic range and stability, it was decided that all of the radiometers for this ACT require a 290 K noise deflection. A 20 dB coupler will require a 20 dB ENR noise diode to meet the required noise deflection. If a 10 dB coupler is used instead, the

required noise diode output power will be only 10 dB ENR, an order of magnitude less power than with a 20 dB coupler. Producing a 20 dB ENR noise diode at 92 GHz is currently not feasible. Realizing a 10 dB ENR noise diode at 92 GHz has been achieved, as described in Section 2.2.3.2. Therefore, a 10 dB coupler was chosen for this radiometer.

The coupler was measured with an Agilent E8364B Vector Network Analyzer, including 100 GHz frequency extension options, and a set of OML Waveguide extender heads, model V10VNA2. The measured transmission loss, return loss, coupling and directivity are shown in Figure 2-33 through Figure 2-36, respectively. The coupler's measured insertion loss over the bandwidth of the radiometer is only 0.315 dB, 0.9 dB less than specified. The measured coupling factor, which includes insertion loss, is 10.5 dB. Assuming a 10 dB ENR noise diode, the measured insertion loss ($1/G$) and coupling factor (C) correspond to a noise deflection of 258 K, as shown by Equation (2-9). For example, when the antenna observes a 300 K scene with the noise diode on, the output of the coupler has an equivalent temperature of 558 K; this is generally the largest temperature that will be output from the coupler and this is what determines the maximum signal level at the power detector.

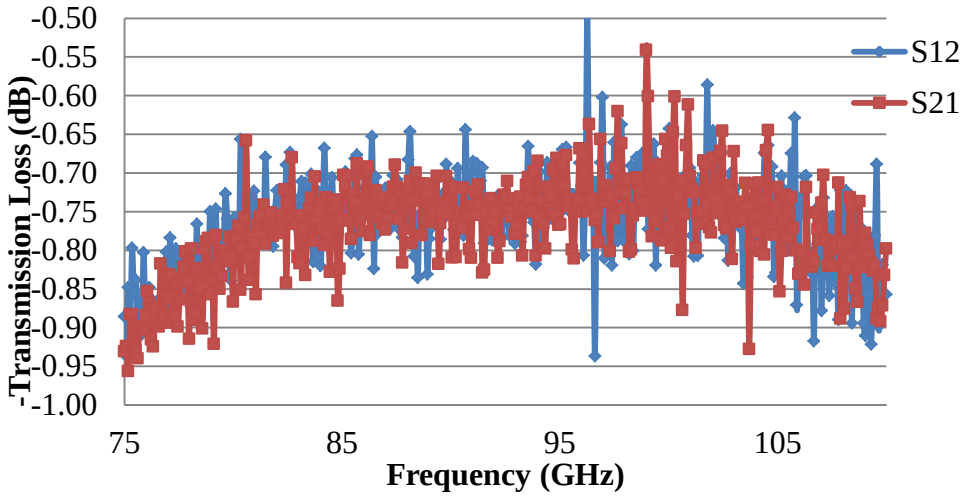

Figure 2-33. ELVA coupler measured transmission loss response

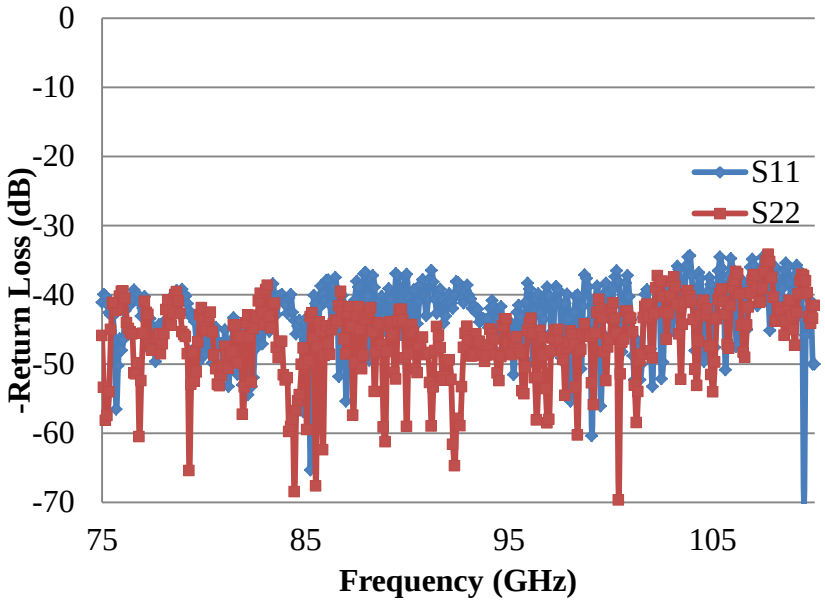

Figure 2-34. ELVA coupler measured return loss response

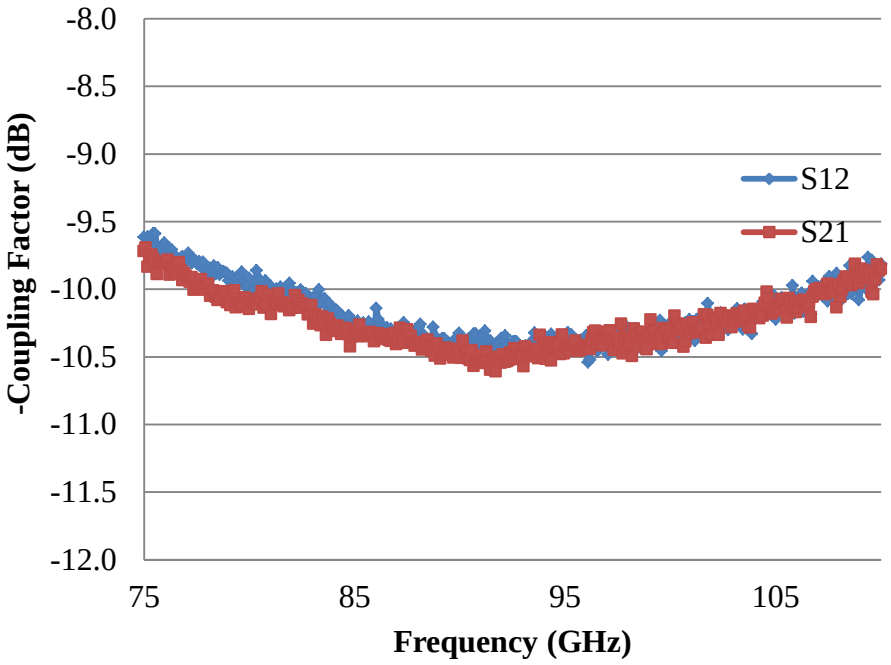

Figure 2-35. ELVA coupler measured coupling factor

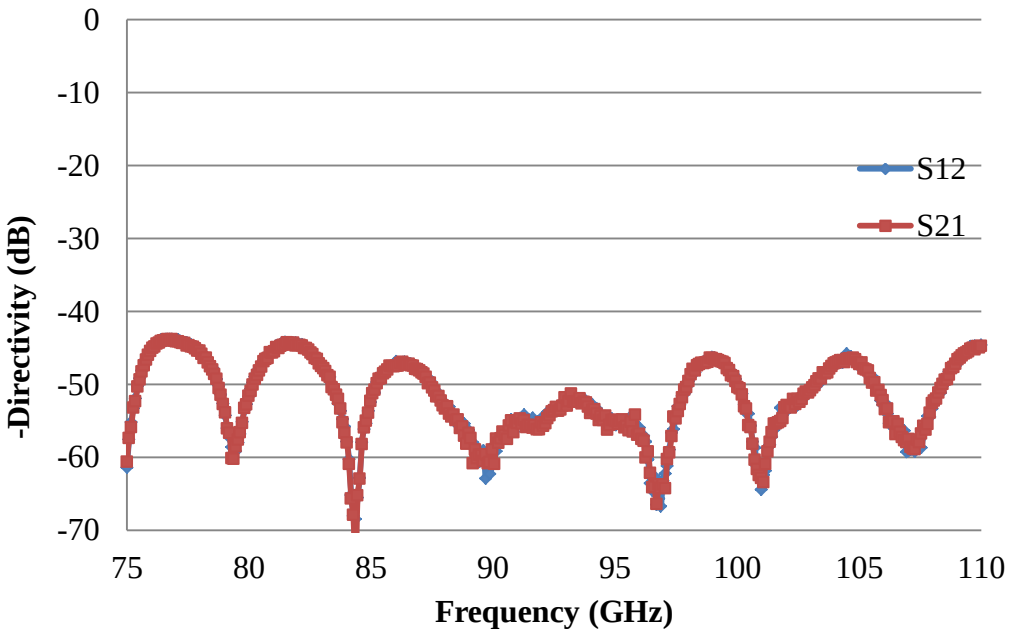

Figure 2-36. ELVA coupler measured directivity

2.2.3 JPL Designed Components

The objective of the ACT project is to reduce the risk, cost, and development time to deploy high frequency radiometers in the 90-170 GHz range on ocean altimeter satellite missions. Several key radiometer components were identified as technological challenges to be overcome. These components needed to be designed and demonstrated in a laboratory prototype radiometer system. The MSL at Colorado State University (CSU) was responsible for designing the demonstration radiometers, and NASA's JPL was responsible for developing the individual component technologies. This section will present the design objectives and measured performance of these essential components designed by JPL for the 92 GHz band.

2.2.3.1 PIN Diode Switch for 80-105 GHz band

As stated in Sections 2.2.2.3 and 2.1, this switch was not used in the 92 GHz radiometer due to the long lead times associated with wafer fabrication. The design goals were insertion loss of less than 2 dB, return loss of greater than 15 dB, and isolation of greater than 20 dB. Several different variations of this switch were produced, including variations in diode size, switch layout, and a switch with an integrated matched load. Only the results for the symmetric switch layout will be discussed.

This switch was fabricated using Northrop Grumman's InP MMIC p-type insulator n-type (PIN) diode process. The switch uses PIN diodes in a series-shunt configuration, shown in Figure 2-37, to maximize port to port isolation. Open circuit radial stubs were

used for RF grounds to avoid high parasitic inductance vias. Microstrip transmission lines were used, Figure 2-38 shows a photograph of the switch. Figure 2-39 shows a comparison of measured and simulated responses.

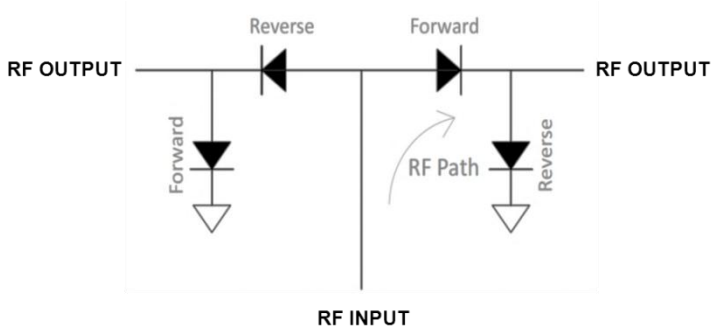

Figure 2-37. Simplified block diagram of a series-shunt diode switch configuration showing DC biasing of the diodes and the RF path [17]

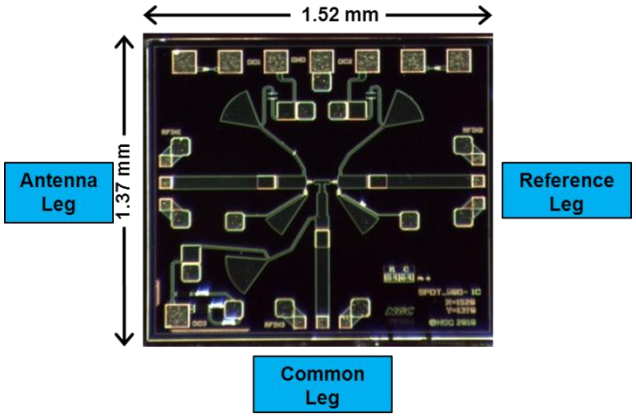

Figure 2-38. Photograph of 80-105 GHz PIN diode switch [17]

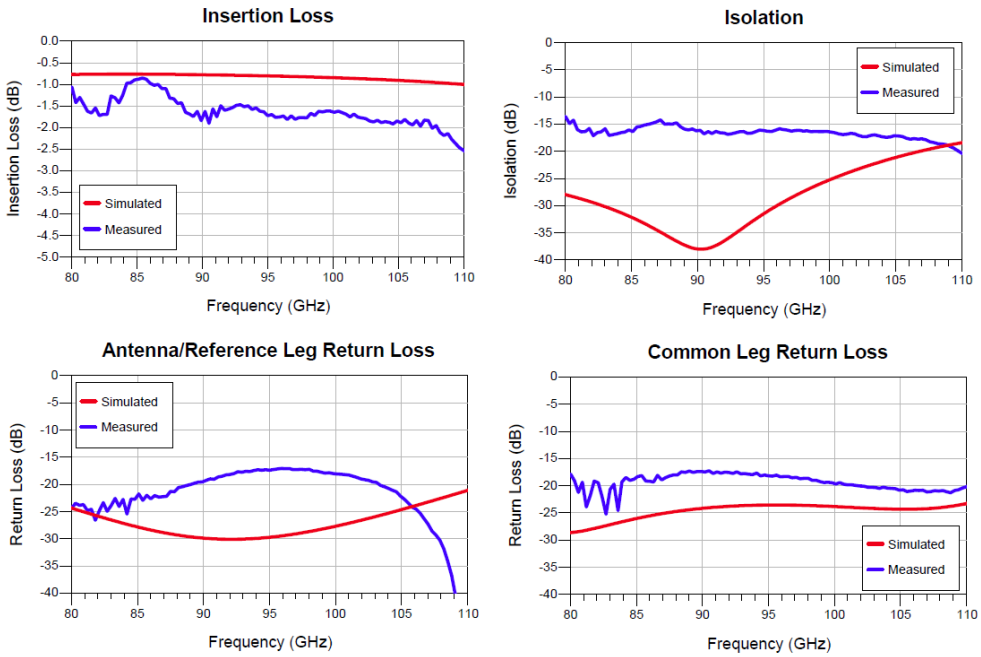

Figure 2-39. Comparison of JPL-measured and simulated performance of 80-105 PIN diode switch [17]

The measured switch insertion loss in the frequency band of interest is between 1.5 and 1.9 dB, return loss is greater than 17 dB, and isolation is greater than 15 dB. Although the insertion loss and return loss do not exactly match the simulation, they meet the design goals and are better than the M/A-Com switch results shown in Section 2.2.2.3.

The measured switch isolation is considerably different from the simulated response. The measured isolation can be seen to start trending downward at the high frequency end of the plot in Figure 2-39. The minimum isolation occurs at around 112 GHz. The offset in the isolation frequency response is believed to be due to an inaccurate diode model used in design and simulation. This issue was resolved by increasing the electrical length of the radial stub that provides the RF ground for the shunt PIN diode. This increase in

electrical length adds additional inductance to the open circuit stub. This added inductance better cancels the capacitance of the shunt diode. The electrical length was increased by bonding a piece of gold ribbon to the end of the stub. A photograph of this solution is shown in Figure 2-40. A comparison of the measured isolation before and after the fix is shown in Figure 2-41.

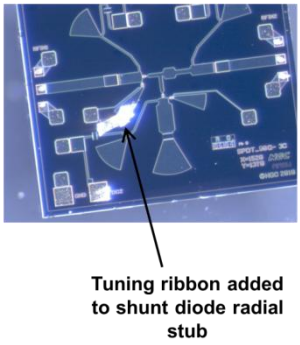

Figure 2-40. Photograph of the switch after the radial stub length was increased [17]

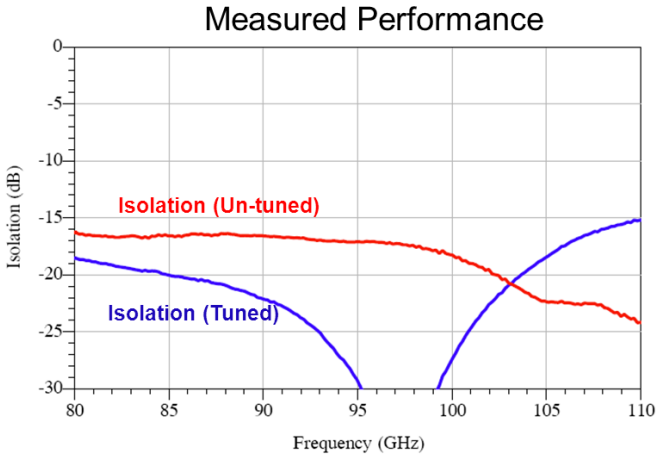

Figure 2-41. A comparison of JPL-measured isolation before and after the radial stub was tuned [17]

Although this is not a permanent fix for the isolation response, it demonstrates that this performance can be improved. A second wafer of PIN diode switches was produced up until the last step of etching the top metal layer. In the future, this measured data can be used to improve the model of the diodes, and the isolation performance can be improved on the second wafer.

2.2.3.2 92 GHz Noise Source

The noise source is used as one of the two internal calibration reference points. It must have sufficiently high ENR, and be stable over time, temperature, and frequency.

This design is based on a well characterized reverse biased PIN diode. When a diode goes into the avalanche breakdown region, it generates RF noise. Noise diodes are optimized for generating stable, repeatable noise output powers for specific reverse breakdown currents.

Several noise diode types were tested. The noise diode with the highest measured ENR is a beam lead packaged avalanche diode manufactured by M-Pulse Microwave. It was developed at the request of NASA Goddard Space Flight Center (GSFC) under a NASA Small Business Innovation Research (SBIR) grant and is not commercially available. A photograph of the diode in the test housing is shown in Figure 2-42. The measured noise source response for various bias currents is shown in Figure 2-43. The diode was tested in a generic waveguide housing that JPL has designed to test LNAs. It was mounted on a generic alumina biasing substrate. The measurements show significant ripple in the

frequency response. This ripple is due to the lack of a matching network in this test setup. A better test would have included a matching network, either on the alumina substrate or an isolator outside of the waveguide.

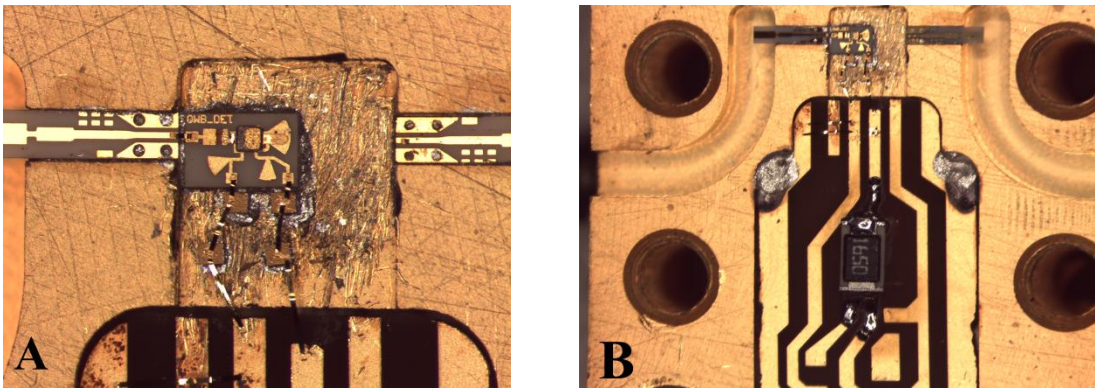

Figure 2-42. Images of the diode test setup, (A) close up and (B) zoomed out, including the biasing board and current limiting resistor [18]

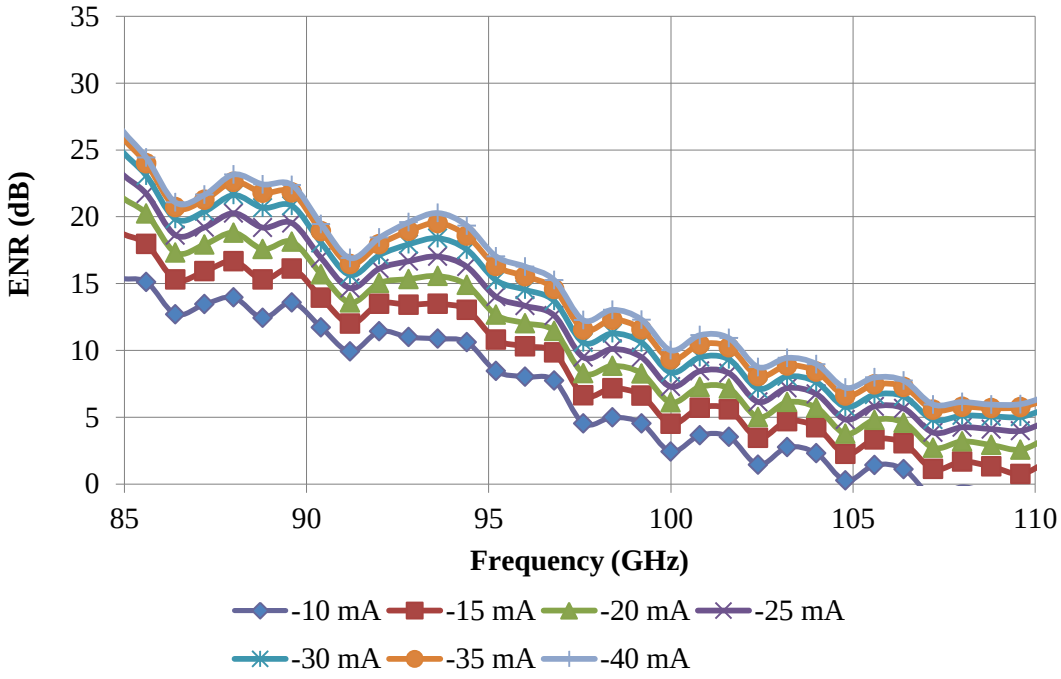

Figure 2-43. JPL-measured diode ENR for several different bias currents [18]

It can be seen that the goal of a 10 dB diode ENR will be achievable with a bias current between 10-15 mA.

2.3 92 GHz Multichip Module

The multichip module (MCM) is depicted in the 92 GHz block diagram, Figure 1-6, indicated by a dashed line. The MCM houses the microstrip and MMIC based components and their associated biasing printed circuit boards (PCBs). It provides the components with a bonding surface, a common ground plane, and a common thermal connection. The MCM utilizes a split block design, consisting of two halves that are bolted together to complete the assembly; it is machined in brass and gold plated. The 92 GHz MCM was designed using AutoCAD by CSU students.

The MCM provides a length of waveguide to interface the thin-film waveguide-to-microstrip transition with the waveguide based components outside of the MCM. Standard WR-10 waveguide dimensions of 100 mils (2.54 mm) by 50 mils (1.27 mm) were used. Half of the MCM waveguide is in the lower half of the split block and half of the waveguide is in the upper half of the split block. The field lines of a TE_{10} propagation mode in a rectangular waveguide are symmetric about the center of the broad wall, see Figure 2-44. The waveguide was split about its broad wall to minimize any disruption of these field lines and to minimize resistive and radiative losses in the waveguide [19].

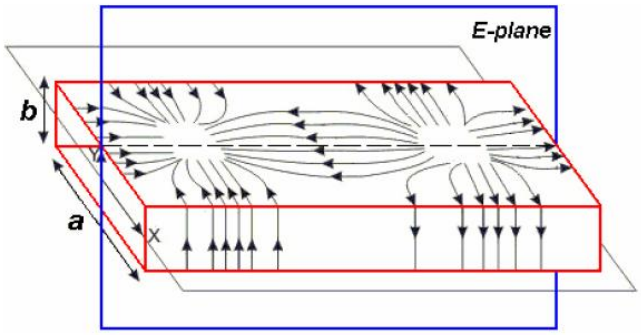

Figure 2-44. Electric field lines of the TE_{10} mode of propagation in a rectangular waveguide [19]

The trench in the MCM where the MMIC components are located is referred to as the RF trench. The trenches that connect the RF trench to the bias boards are referred to as the biasing trenches. When the MCM is assembled, these trenches act as waveguides. The dimensions of the RF and biasing trenches were carefully designed to be certain that their waveguide cutoff was far above the system's operating frequency. The equation for the waveguide cutoff of the dominant TE_{10} mode in an empty cavity is

$$f_c = \frac{c}{2 * a} \tag{2-10}$$

where *a* is the dimension of the broad wall of the waveguide and c is the velocity of light. The dielectric loading of the cavity by components will lower the actual cutoff frequency. If the waveguide is not in cutoff, it can act as a feedback path from the output of the amplifiers to their input and cause the LNAs to become unstable. The widest trench in the MCM is 40 mils (1.0 mm), with an associated cutoff frequency of 147.6 GHz.

Cavity dimensions, especially lid height, have a significant impact on component performance at millimeter wavelengths. The impact of cavity dimensions is especially

apparent in the response of the bandpass filter. The simulated filter response in open air and in a cavity can be seen by comparing Figure 2-6 and Figure 2-9. All of the components were designed, simulated, and optimized in cavities with dimensions that needed to be precisely replicated in the MCM. The highest level of precision, without a significant increase in cost, which a machinist can provide is on the order of 0.1 mils (2.5 μm).

The bottom half of the MCM clamshell was cut 5 mils (0.13 mm) deeper than the regions closest to the RF and bias trenches, as shown in Figure 2-45. The higher portions next to the trenches form a pressure ridge of 5 mils (0.13 mm) height. The pressure ridges concentrate the compression force on the component trenches and ensure a close fit between the top and bottom of the MCM. The compression is from the bolts holding the MCM closed.

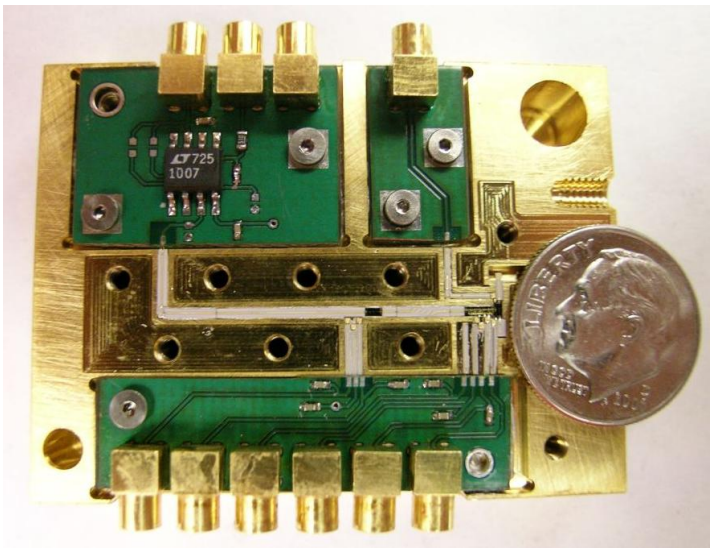

Figure 2-45. Bottom half of assembled 92 GHz MCM

2.4 Bias Boards

The bias boards interface the MMIC components with their respective bias and control signals. These PCBs are fabricated on standard FR4 copper clad laminates. The copper on the bottom side of all of these boards was left exposed, i.e. no solder mask, and they were silver epoxied to the MCM to ensure the lowest possible impedance ground connection. The ground reference for all of these boards is provided through a single large gauge wire between the MCM chassis and the back-end board. A single ground connection is important to avoid the generation of ground loops. OrCad tools were used for both schematic design and layout of these PCBs.

The 92 GHz radiometer has three bias boards, i.e. a gate and drain control board, a Dicke switch board, and an output gain board. These boards interface with the MMIC based components through on-board wire bonding pads. It is difficult to produce a reliable wire bond on the solder coated PCB pads, so the connections were made using a gold ribbon parallel gap welding machine. Another solution would be to use a gold plated board, although this is an expensive option.

The gate and drain control board routes the gate and drain bias voltages from the back-end board to the MMIC based LNAs. It also carries one of the two switch control signals. There are three gate bias lines, two for the first LNA and one for the second LNA. The first gain stage of the first LNA has a separate gate control line to allow bias adjustment

of the first LNA for minimum receiver noise figure. The board uses voltage dividers on the gate control lines. The use of on-board voltage dividers is beneficial because it allows for the LNA and bias generation to have identical ground references. In the final configuration, the best performance was achieved by grounding all three gate lines. This provided a minimum noise figure. Additional gain was not needed due to the two high gain, 30 dB, LNAs. The board also provides a common drain voltage line to bias both LNAs. The drain line is AC bypassed with 1 μF capacitors near each bond pad. The board connects to the back-end board via a 6 pin Molex PicoBlade connector.

The Dicke switch requires two complementary control signals, one positive and one negative. One of them is supplied by the Dicke switch board, and the other is supplied by the gate and drain control board. This line is AC bypassed with a 1 μF capacitor near the bond pad. This board uses a 2 pin Molex Picoblade connector.

The output gain board amplifies the DC output of the RF square law detector and interfaces the amplified signal with the back end board. This amplification is accomplished using a Linear Technologies LT1007 ultra low noise, high speed, precision operational amplifier. This amplifier was incorporated in the MCM to provide noise immunity for the power detector signal being routed from the MCM to the back-end board; smaller signals are more susceptible to interference.

As mentioned in Section 2.2.2.2, after several months of testing the 92 GHz radiometer, three RF power detectors failed on three separate occasions. After the first detector

failure, electrostatic discharge (ESD) was the expected cause. However, even after closely following ESD precautions, two additional power detectors failed. HRL Technologies, the manufacturer of the power detector, indicated that the operational amplifier on the output gain board could be responsible for the issue. The input of the operational amplifier was measured with an oscilloscope. It was discovered that the moment a bias voltage was applied, or removed, the amplifier's input would source a transient voltage. The transient voltage has an amplitude swing between ± 300 mV, enough to destroy the detector. After this was discovered, an RC low pass filter was added between the detector and the amplifier, as shown in Figure 2-46. Prior to that, the amplifier input had been connected directly to the detector output. The problem has not re-emerged since this solution was implemented.

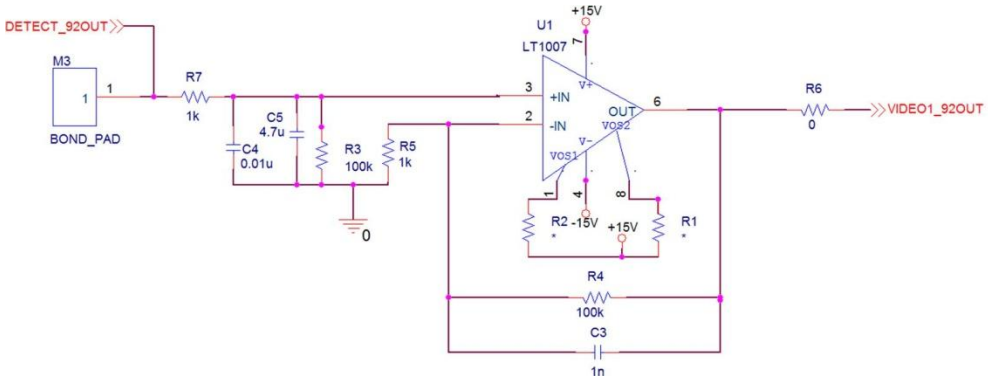

Figure 2-46. Amplifier schematic with input low pass filter

Two revisions of the bias boards and the back-end board were fabricated. On the first revision, extremely small coaxial cables and connectors, micro miniature coaxial (MMCX), were used to interface between the back-end and the bias boards. These were

used because their shielding reduces the potential for any RF interference on the signals interfacing between the back-end board and the MCM. However, it was discovered upon testing the first revision that there was an unacceptable amount of noise on the detected power detector signal on the back-end board. Several changes were made to the back-end, including changing the MMCX cables to discrete wire connectors. The problem with the MMCX cables is that each cable provides a separate ground path to the MCM. These separate ground paths allow ground loops to form, i.e. different potentials at different grounds as opposed to one equipotential ground plane. Ground loops can be a major source of noise and interference. The second revision of the back-end board and bias boards eliminated the noise issues that had plagued the first revision. Since so many things were changed, it is unclear whether or not changing the cables had a large impact. There are ways to reduce ground loops due to shielded cables; solutions include adding isolation transformers, optical isolators, or ferrite chokes to the lines. However, the simplest and cheapest solution for this application is to switch from the coaxial cables to discrete cables.

2.5 92 GHz Radiometer Testing and Performance

Three metrics were used to determine system functionality and performance. These were system noise temperature, system stability, and internal calibration stability. Through these three measurements it is possible to compare the system to other radiometers, calculate how often a calibration is necessary, and calculate the uncertainty associated with measurements.

2.5.1 Final System Gain and Noise Figure Calculation

The component list and noise analysis of the final design are shown in Table 2-2. The receiver noise figure and noise temperature were calculated using Equation (2-3). The measured insertion loss of the components, when available, was used to determine the predicted receiver noise temperature. The major design differences between the initial and final designs are a second gain stage, an alternate directional coupler, the removal of the isolator, and an improved estimate of Dicke switch insertion loss.

Table 2-2. Updated system noise temperature estimate

Component	Vendor	Part Number	Gain (dB)	Noise Figure (dB)	Cumulative Noise Temperature (K)
Directional coupler	ELVA	DC-10	-0.32	0.32	22
Waveguide through line	Custom Microwave	ST10R	-0.20	0.20	37
Waveguide to microstrip transition	MSL	-	-0.50	0.50	77
Switch	M/A-Com	MA4GC6773	-3.55	3.55	541
LNA	HRL Labs	LN5-100	29.00	3.00	1367
BPF	MSL	-	-1.56	1.56	1368
Attenuator	MSL	-	-2.75	2.75	1369
LNA	HRL Labs	LN5-100	29.00	3.00	1372
Attenuator	MSL	-	-2.75	2.75	1372
Receiver gain (dB)	46.4				
Receiver noise figure (dB)	7.6				
Receiver noise temperature (K)	1371.9				

A second LNA gain stage was included in the final radiometer design to increase the post detection signal level as well as the radiometer's voltage-temperature sensitivity.

The coupler was changed from the Dorado coupler in the initial design to an ELVA coupler. This was done because the Dorado coupler had an unacceptably high measured insertion loss of 1.8 dB compared to the ELVA insertion loss of only 0.32 dB. Dorado did not specify an insertion loss on their data sheet; the loss of an ideal coupler was used in the original noise analysis.

The isolator was removed from the design because it was deemed unnecessary. Typically, an isolator is placed between the first LNA and the Dicke switch. This is done to eliminate LNA gain changes due to the different impedances presented at its input at different Dicke switch positions. This was not possible in this design due to the lack of availability of W-band microstrip based isolators. The initial purpose of including an isolator between the coupler and the MCM was to improve the match between the input of the MCM and the antenna. However, the effect of the isolator's loss on the system noise figure outweighed any benefit that the improved matching added. Instead, the isolator is used between the noise diode and the coupled port of the directional coupler. The isolator greatly improves the noise diode's poor match, and the noise diode's ENR level is still sufficient, even after the insertion loss of the isolator.

As stated previously, the 92 GHz Dicke switch is specified to operate only up to 77 GHz. The insertion loss of the Dicke switch used in the original system noise figure calculation is that specified for 77 GHz. The updated loss used in the final calculation includes some error due to the microstrip transmission lines and the J micro Technologies GSG transitions that were included in the switch measurement.

The updated gain and noise figure analysis results in a predicted 1372 K system noise temperature and 46.4 dB of receiver gain. This gain and noise figure results in a predicted signal level of –23 dBm presented to the detector when the 600 K noise diode is turned on. For a detector sensitivity of 13,500 V/W, this should result in an 88 mV detector output and a pre video gain sensitivity of 45 μV/K. However, the measured detector output is only 2.64 mV and the system sensitivity is 1.6 μV/K. This 2.64 mV output voltage is consistent with a –37 dBm signal at the power detector input. This power level is within the square law region of the detector diode and reasonably close to the upper limit of –40 dBm.

If we assume that the system bandwidth is 5.1 GHz, and the detector sensitivity is 13,500 V/W, the gain required to produce the measured voltage to temperature sensitivity can be calculated by differentiating the output voltage with respect to temperature

$$V_{out} = k\left(T_{sys} + T_A\right)BG\beta \tag{2-11}$$

$$\frac{dV_{out}}{dT} = kBG\beta \tag{2-12}$$

In this manner, the gain was measured to be 32.3 dB. There is a 14 dB difference between the calculated gain and the measured gain. It is unclear from where the disparity between the measured and calculated gains arises. This could be due to matching issues within the MCM, wire bond losses and mismatches, or due to components behaving differently than expected inside a cavity.

2.5.2 Measured Noise Performance

The Y-factor method was used to measure the system noise temperature. For this radiometer, the Y-factor method was implemented as follows: The radiometer takes measurements of a microwave absorber at ambient temperature, i.e. the warm reference, as well as an absorber that has been soaked in liquid nitrogen (LN_2), i.e. the cold reference. These measurements are made with the radiometer operating in a total power mode. This means that the Dicke switch remains in the antenna position during the entire measurement. The physical temperature of the ambient absorber is measured, and the liquid nitrogen cooled absorber is assumed to be 77.6 K. The Y-factor is calculated using

$$Y = \frac{V_{roomtemp}}{V_{LN_2}} \tag{2-13}$$

Next, the system noise temperature is calculated using

$$T_{sys} = \frac{T_{roomtemp} - Y * T_{LN_2}}{(Y - 1)} \tag{2-14}$$

The system noise temperature was initially measured to be 1400 K. The LNA drain voltage was then increased from 0.9 V to 1.15 V. The increase in drain voltage caused an increase in LNA bias current and a decrease in receiver noise temperature, to 1272 K. The lower receiver noise temperature is likely due to an increase in amplifier gain, reducing the effect of the noise temperature of components after the LNA. The receiver noise temperature decrease could have been due to the increase in drain voltage, which in turn brought the second LNA out of compression.

The system noise temperature, 1272 K, is lower than predicted. There are several uncertainties in the characteristics of the radiometer components that could cause this lower noise temperature. These uncertainties include the switch insertion loss, waveguide-to-microstrip transition loss, the LNA noise temperature and gain in the band of the 92 GHz radiometer. There are relatively large uncertainties in the switch insertion loss measurements, due to the uncertain insertion loss of the microstrip transmission lines and the J micro technology GSG, as described in Section 2.2.2.3. If the predicted loss prior to the first LNA decreases from the predictions by only 0.25 dB, the predicted noise temperature matches the measured. The uncertainty of the microstrip transmission lines and GSG in the switch insertion loss measurements could easily be on the order of 0.25 dB. If this is the case, the actual switch insertion loss would be 3.3 dB.

Since the measured voltage is statistical in nature, not just a constant output voltage, the average value of the radiometer output was used to calculate the system noise temperature. The warm reference and the cold reference were both measured for 15 seconds at a time, and the radiometer output was averaged over this time period.

The time variation of the measured receiver noise temperature is shown in Figure 2-47.

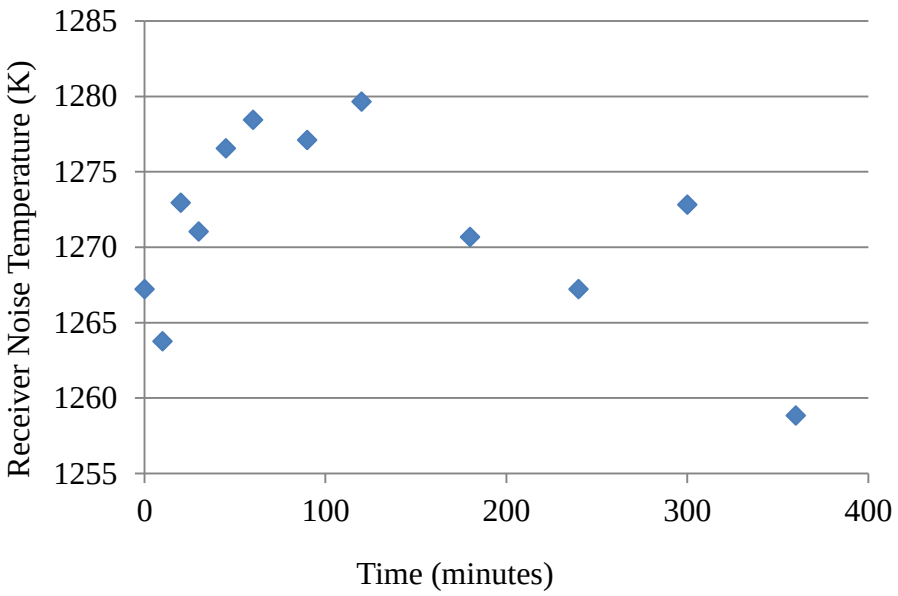

Figure 2-47. Time variation of the measured 92 GHz receiver noise temperature

2.5.3 System Stability

System stability is an important consideration that determines required calibration frequency as well as maximum effective integration time. The system stability was determined by making long term measurements, on the order of several hours, of stable reference temperatures, including the temperature controlled internal matched load. The stability of the long term data was quantified using Allan deviation analysis.

The stability of the radiometer is highly temperature dependent. Variations in the temperature of the MCM or the back-end board cause variations in the measured output data. The MCM is thermally controlled with a Peltier thermoelectric heater/cooler. The MCM temperature is controlled to within ± 0.1 °C at a set point of 28 °C. The entire

radiometer system, except for the microcontroller development board, is housed in thermally insulating foam. The back-end board does not have any active temperature control; it is very likely that adding active temperature control to this board would improve the stability of the radiometer.

The radiometer was left powered on for several hours prior to making any system stability measurements. This was done to allow the radiometer to 'warm up' until the measured temperatures of various points on the radiometer are stable to within ±0.1 K. The radiometer takes about two and a half hours to achieve this level of thermal stability. This time could be reduced if active temperature control were added to the back-end board. A time series of radiometer output is shown in Figure 2-48. The radiometer was unpowered for over 24 hours prior to this test. This plot illustrates the effect of temperature variation on the un-calibrated output of the radiometer. The data for the plot was collected from the time that the radiometer was powered on to the point when the output fluctuations were within ±0.1 K.

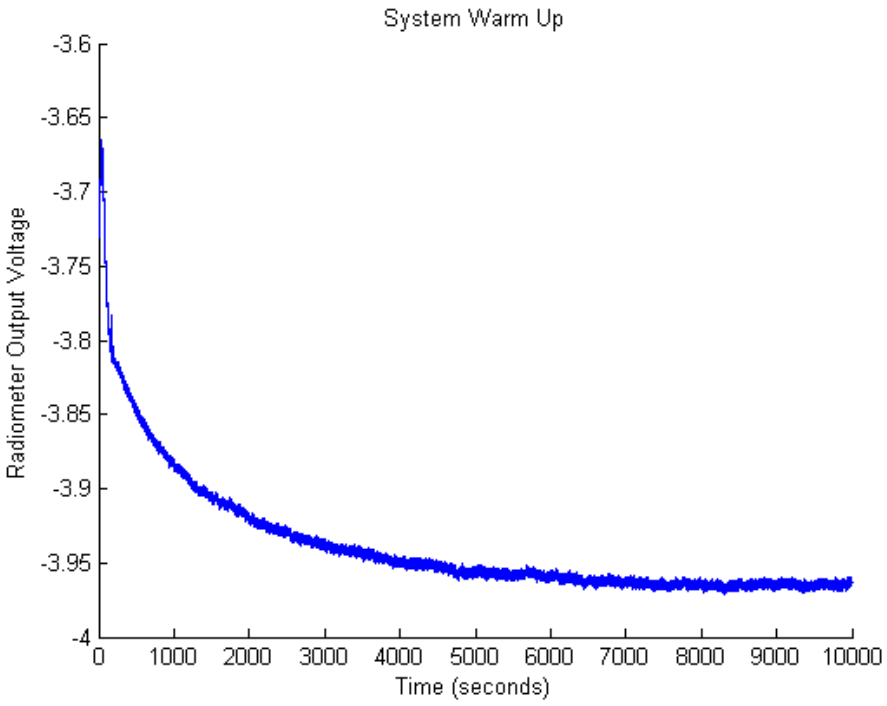

Figure 2-48. 92 GHz radiometer output voltage versus time, demonstrating system warm up time

Allan variance is a useful tool for analyzing the stability of systems. It is commonly used to measure oscillator stability. Allan variance is a two-sample variance formed by the average of the squared differences between successive values of a regularly measured quantity taken over sampling periods from the measuring interval up to half of the maximum measurement time [20]. Allan variance is defined as

$$\sigma_y{}^2(\tau_o) = \frac{1}{2(N-1)} \sum_{i=1}^{N-1} (T_{i+1} - T_i)^2 \tag{2-15}$$

for N measurements of brightness temperature T_i with sampling period τ_o. The sampling period is varied by averaging n adjacent values of T_i so that $\tau = n\tau_o$

$$\sigma_y{}^2(\tau) = \frac{1}{2\tau^2(N-2n+1)} \sum_{i=1}^{N-2n+1} (T_{i+2n} - 2T_{i+n} + T_i)^2 \quad (2\text{-}16)$$

Allan deviation is defined as [21]

$$\sigma_y(\tau_o) = \sqrt{\sigma_y{}^2(\tau_o)} \quad (2\text{-}17)$$

Allan time is defined as the point at which longer averaging, or observation, times do not further reduce the Allan deviation. In terms of microwave radiometry, the Allan time is the maximum integration time that will result in a reduced radiometric resolution before gain variations overcome the effect of longer averaging times.

The Allan deviation and a time series of un-calibrated radiometer output are shown in Figure 2-49 and Figure 2-50. Time series of the MCM and back-end temperatures during the Allan deviation testing are shown in Figure 2-51 and Figure 2-52. It can be seen that there is a correlation between the radiometer output and back-end thermal variations.

The measured Allan time for this system is 3.5 seconds. Several steps could be taken to improve long term system stability. These steps include the addition of active temperature control on the back-end board, replacing the first video amplifier with a chopper style amplifier, as discussed in Section 5.2, and housing the entire system in a temperature controlled chassis.

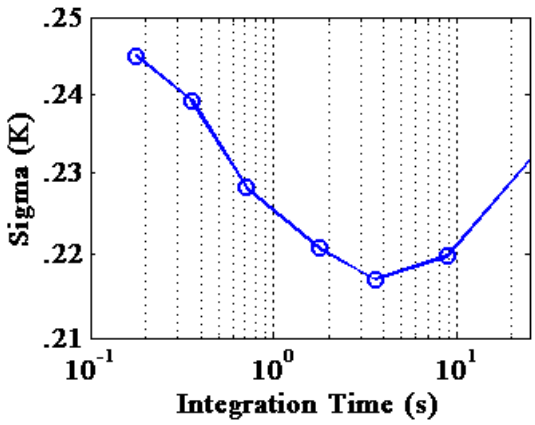

Figure 2-49. 92 GHz radiometer Allan deviation

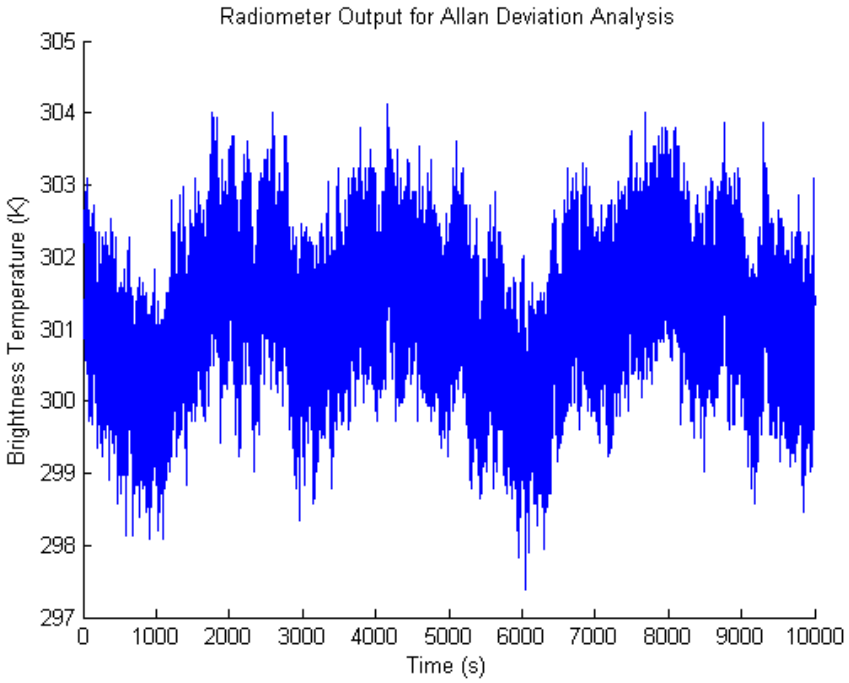

Figure 2-50. 92 GHz radiometer measured brightness temperature versus time

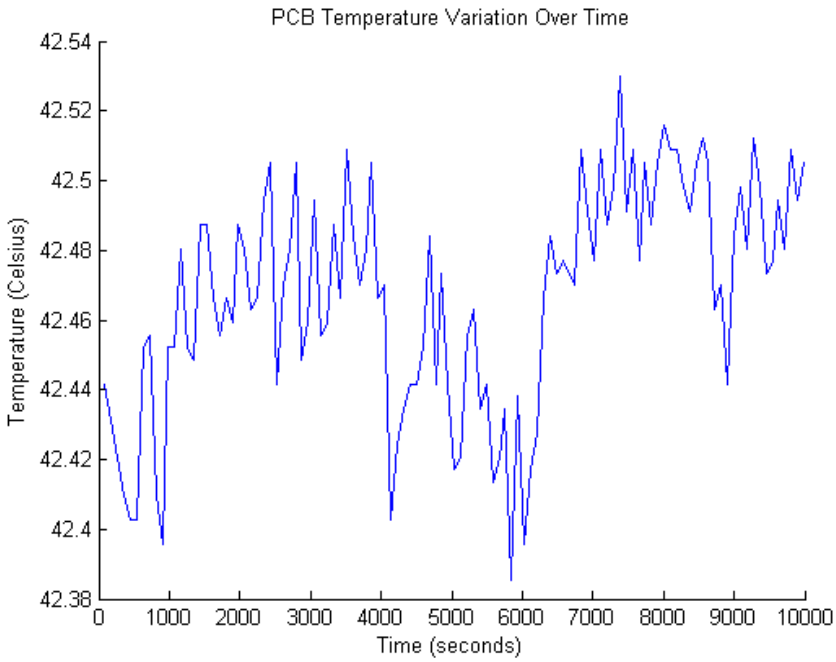

Figure 2-51. 92 GHz back-end board temperature variation during Allan deviation testing

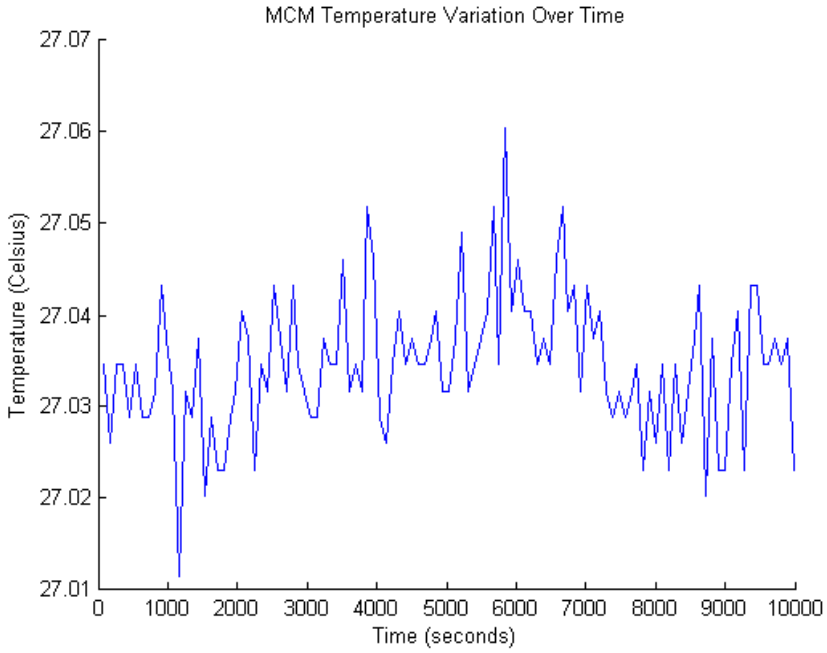

Figure 2-52. 92 GHz MCM temperature variation during Allan deviation testing

The results of the measured system noise temperature and the Allan deviation testing were used to calculate the radiometer's radiometric resolution. The normalized gain variations, $\Delta G/G$ in Equation (1-11), were adjusted until the total power radiometric resolution at integration times greater than 1 s matched the minimum Allan deviation value, approximately 0.2 K. This minimum resolution corresponds to normalized gain variations of $1.60 \cdot 10^{-4}$ at a frequency of 1 Hz. Using an antenna temperature of 300 K and the normalized gain variations based upon the measured Allan deviation, Equations (1-11) and (1-12) were used to calculate the radiometric resolution for total power and Dicke modes of operation, respectively. The radiometric resolution is shown in Figure 2-53. It is interesting to note that the predicted radiometric resolution, with a receiver noise temperature of 727 K, shown in Figure 2-1 is worse than that shown in Figure 2-53, which uses a receiver noise temperature of 1272 K. This is because the predicted gain variations, used in Figure 2-1, were higher than the measured gain variations, used in Figure 2-53.

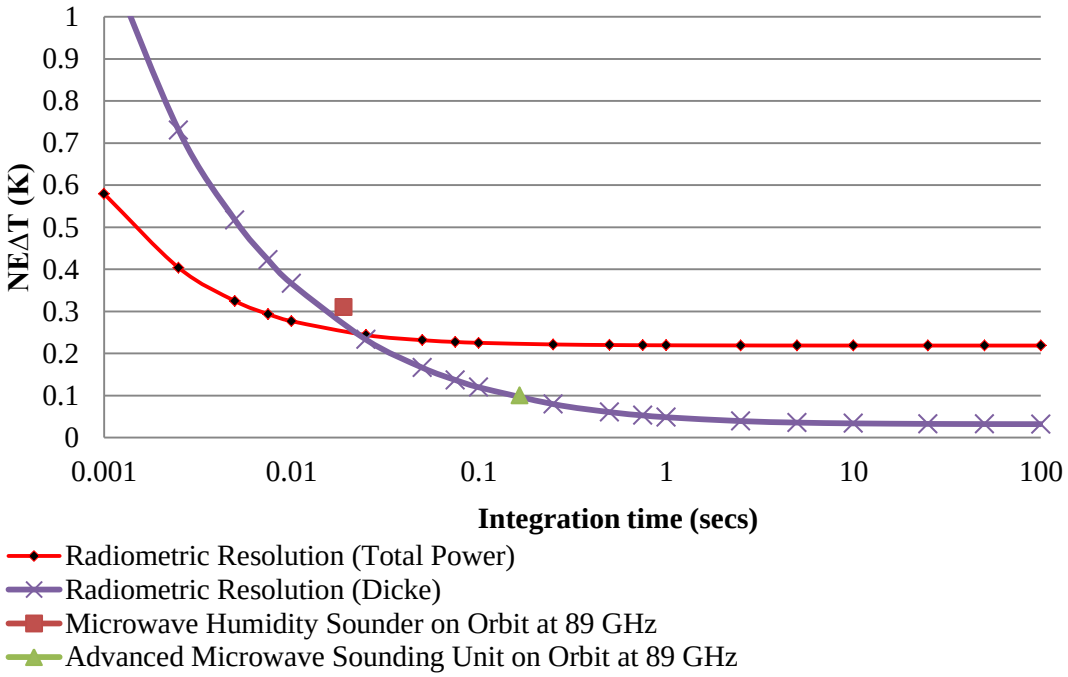

Figure 2-53 92 GHz radiometric resolution

2.5.4 External Calibration

The Y-factor method involves the same steps as external calibration. So, in addition to calculating the system noise temperature, the radiometer can be calibrated using the results of the Y-factor method. Since the detector is operating in the square law region, i.e. linear relationship between input power and output voltage, there is a linear relationship between antenna temperature and radiometer output voltage. The general equation for output voltage versus antenna temperature is

$$V_{out} = aT_{Ant} + b \tag{2-18}$$

where a is the slope in volts per Kelvin and b is the offset voltage.

The coefficients, *a* and *b*, can be calculated by observing two known scene temperatures and recording the radiometer output voltage, as described in Section 2.5.2. These two points are used to calculate the equation of the line. The measured slope of the 92 GHz radiometer is approximately 2.4 mV per K, and the offset voltage varies with time and temperature. The slope of the calibration curve is dependent on system gain, detector sensitivity, and bandwidth. The offset voltage varies much more than the slope. These variations in both the slope and offset are the reason that radiometer calibration is necessary.

The antenna referred temperatures of the internal calibration sources can be calculated using the external calibration curves. Noise produced by the Dicke matched load is equivalent to an antenna temperature of 346 K, and the equivalent antenna temperature of the noise diode is 639 K, with the antenna viewing a 300 K absorber, a bias voltage of 11.4 V, and a current of 15.2 mA.

2.5.5 Internal Calibration

The steps to perform internal calibration are very similar to those of external calibration. Two known temperature points are observed, and the coefficients *a* and *b* in Equation (2-18) are calculated. Instead of observing external scene temperatures, e.g. a microwave absorber with a known temperature, internal sources of known temperature are observed, i.e. the noise diode and the Dicke reference load.

It is important to note that the antenna temperature, T_A, affects the noise diode calibration temperature, as discussed in Section 2.2.2.4. In order to have a consistent calibration point, either the antenna temperature must be known, or the noise diode deflection must be used. If the calibration is performed using the noise diode deflection, the calibration steps will be slightly different than described above. The difference between the two output voltages, along with the measured noise deflection, will be used to solve for the slope, *a* in Equation (2-18). Then, the offset, *b* in Equation (2-18), will be determined by observing the matched load calibration point. In internal calibration testing in the laboratory, all noise diode calibrations were performed with the radiometer observing room temperature microwave absorber. This antenna temperature gives a noise diode equivalent temperature of approximately 560 K.

The downside of internal calibration is that only part of the radiometer system is calibrated, i.e. only the components after the injection of the two calibration signals are calibrated. However, the upside is the ability to calibrate the system without moving parts or external scenes of known brightness temperature.

An interesting practical note is that the most stable operation of the noise diode occurs just after its bias is applied. The noise diode should be allowed to current stabilize; in this testing the current stabilized after about 10 seconds. After the calibration point is measured, the noise diode should be turned off. It was found that leaving the noise diode on for long periods of time caused the output power of the noise diode to drift with time.

2.5.5.1 Internal Calibration Stability

An important consideration is the stability of the two internal calibration points. Any variation in the brightness temperature of the internal calibration points will cause error in the calibration, and therefore in the calibrated brightness temperature measurements [22]. This is not as much of an issue for the Dicke reference load temperature, since it is actively temperature controlled, as it is for the noise diode. The output of the noise diode will vary to some degree with both time and temperature.

In order to assess the stability of the internal reference temperatures, a study was conducted. An external calibration was performed to calculate the antenna-referred brightness temperatures of the internal calibration sources. Next, internal calibrations were performed at regular intervals, and immediately after the internal calibration was performed, a microwave absorber that had been immersed in liquid nitrogen was observed. If the internal calibration sources remain constant, the brightness temperature of the LN_2 cooled absorber is expected to remain constant. A time series of the measured brightness temperature of the LN_2 cooled absorber is shown in Figure 2-54.

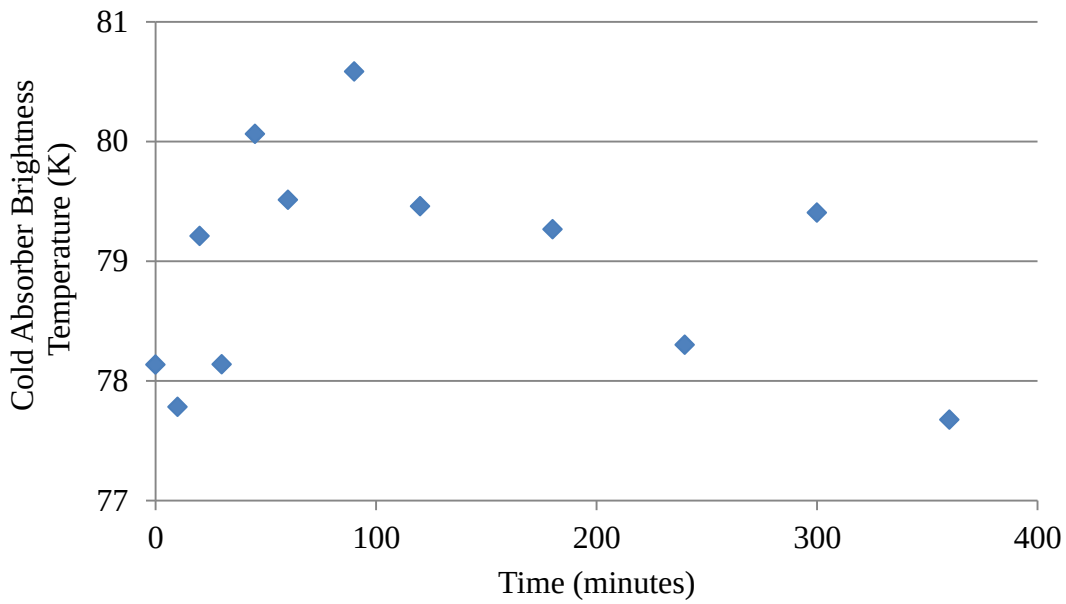

Figure 2-54. Time variation of observed brightness temperature of an absorber cooled in LN_2

Several thermistors monitored the temperature of the MCM, back-end PCB and noise diode over the course of the calibration stability test. In order to determine the cause of the cold absorber fluctuations, the thermistor data was plotted against the absorber brightness temperature. However, no clear correlation was found. Figure 2-55 through Figure 2-57 show the data and R^2 values. All of the correlation coefficients are less than 0.25. This data indicates that variations in the physical temperature of the radiometer are not responsible for the brightness temperature variations.

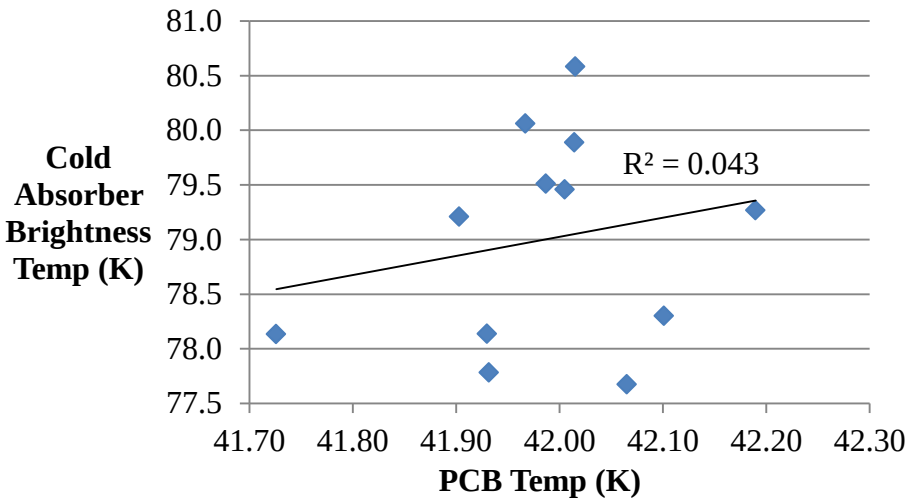

Figure 2-55. Correlation between PCB temperature variations and cold absorber brightness temperature variations

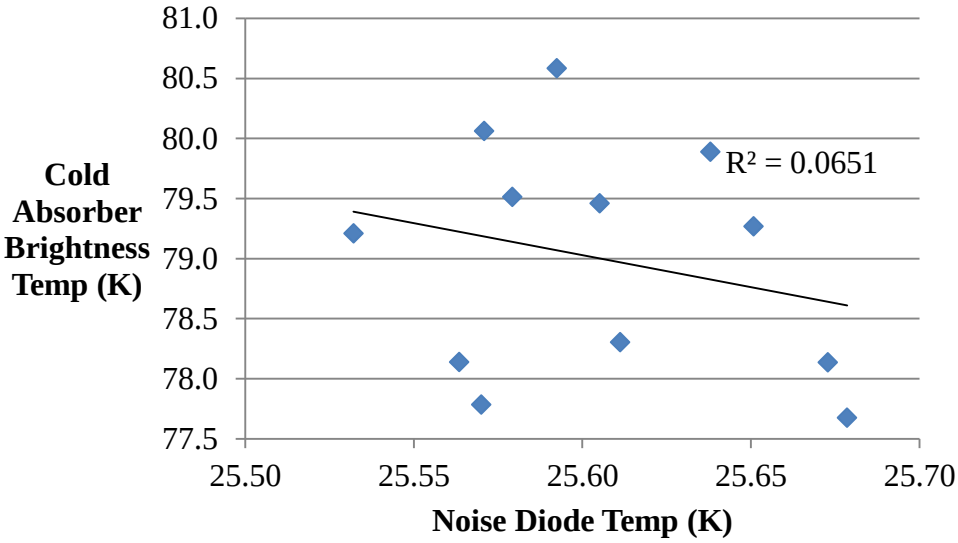

Figure 2-56. Correlation between noise diode temperature variations and cold absorber brightness temperature variations

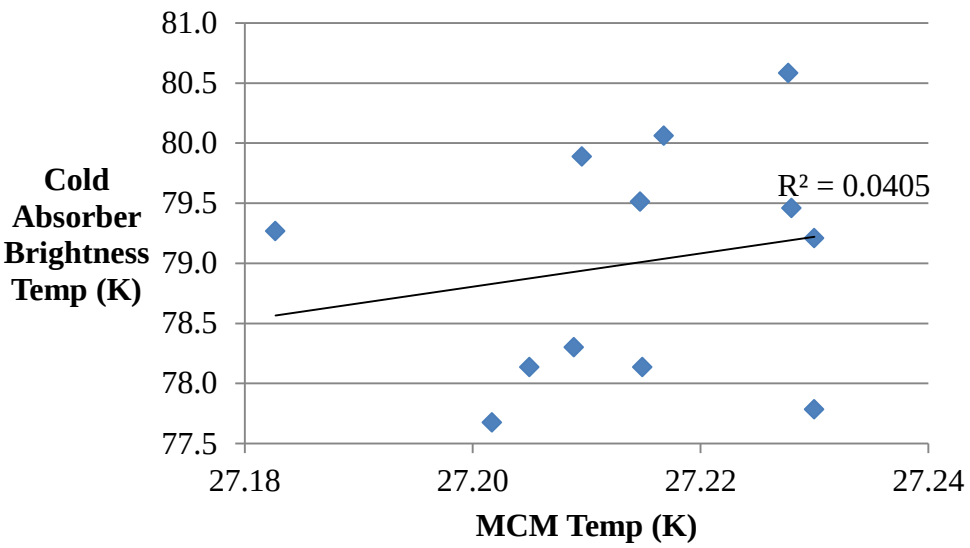

Figure 2-57. Correlation between MCM temperature variations and cold absorber brightness temperature variations

One limitation of this testing method was the way that the LN_2 was measured. The absorber was quickly removed from the liquid nitrogen and held in front of the antenna. This method adds uncertainty to the retrieved data. Once the absorber is removed from the LN_2 it begins to warm up, and its exact temperature is unknown. Also, after some period of time, water begins to condense on the absorber, and the emission from the liquid water adds error to the measurement. In this internal calibration stability study, variations in the noise diode output power could not be differentiated from physical temperature variations in the cooled microwave absorber.

A related internal calibration stability study was performed by [23]. A temperature-controlled and stable calibrated Ka-band radiometer was used to make brightness temperature measurements of absorber immersed in LN_2. The range of variability of the brightness temperature of LN_2 reported by [23] is very similar to that shown in Figure

2-54. For this reason, it is possible that the error due to the LN_2 measurement is greater than the error due to noise diode variation. A more accurate external reference temperature is needed to truly measure the variation in noise diode brightness temperature.

It was found that LN_2 observations with durations under about 10 seconds resulted in relatively consistent measured data, i.e. data with a standard deviation less than about 0.4 K. The output voltage begins to slope upward with longer observation times, likely due to condensation. A time series of radiometer output voltages when observing a cold absorber is shown in Figure 2-58. The slope that occurs, likely due to condensation forming on the absorber, can be seen starting at around 10 seconds.

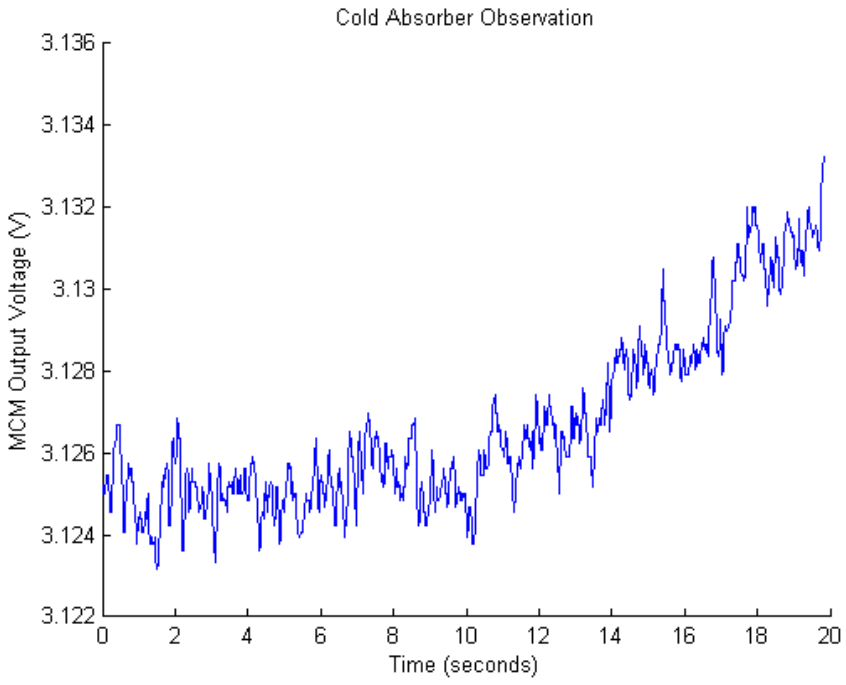

Figure 2-58. Cold absorber observation showing slope likely due to condensation

2.5.6 92 GHz Mass and Power Consumption

A table with the mass of the various radiometer components is shown in Table 2-3. This table does not include the mass of the power supplies or temperature control module. These components were not optimized for low mass, and therefore different components would be used in space-borne radiometers.

Table 2-3. 92 GHz radiometer mass

	Mass (g)
MCM and waveguide components	675
Heat sink, fan, and Peltier device	463
Back-end board	144
Microcontroller development board	197
Total	1,479

The 92 GHz radiometer power consumption is shown in Table 2-4. This table does not include power consumed by the thermal control or the microcontroller development board. These subsystems were not optimized for minimum power consumption and therefore would be designed differently for space-borne radiometers.

Table 2-4. 92 GHz radiometer power consumption

	Power consumption (W)
MCM	0.204
Back-end board	3.220
Total	3.424

Chapter 3: 166 GHz Radiometer

3.1 Radiometer System Overview

The 166 GHz radiometer is the highest frequency of the three radiometers designed as part of the ACT project. This design was started after the majority of the 92 GHz testing was completed. Therefore, this design was improved by lessons learned with the 92 GHz radiometer. However, this design also presented new challenges that were not faced in the 92 GHz design due to the much higher frequency.

The 166 GHz design is a similar topology to the 92 GHz design. This design uses a Dicke-switched direct detection architecture. The block diagram for the 166 GHz radiometer is shown in Figure 3-1. The main differences between the 166 GHz block diagram and the 92 GHz block diagram are the additional gain stages, two band definition filters, and a waveguide output, as opposed to the DC detector output on the 92 GHz design. Table 3-1 lists the 166 GHz radiometer components, vendors, and their measured gain and noise figure.

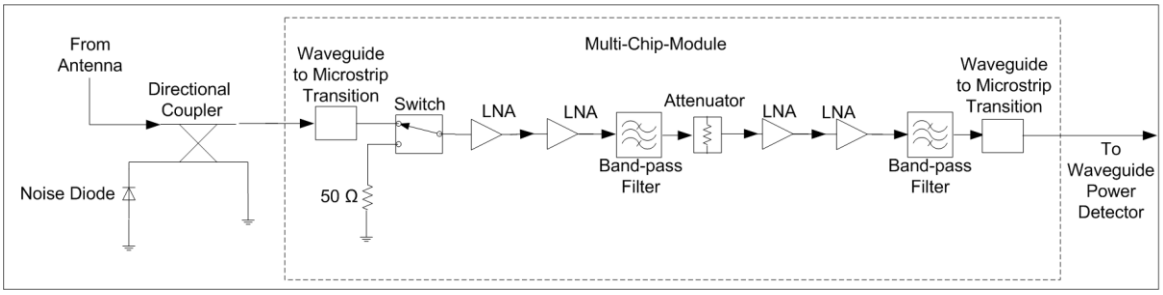

Figure 3-1. 166 GHz receiver block diagram

Table 3-1. 166 GHz receiver noise analysis

Component	Vendor	Part Number	Gain (dB)	Noise Figure (dB)	Cumulative Noise Temperature
Directional coupler	ELVA	DC-05	-1.42	1.42	112
Through Line	Custom Microwave	ST5R	-0.30	0.30	141
Waveguide-to-microstrip transition	MSL	-	-0.5	0.5	194
Switch	JPL	-	-3	3	675
LNA - includes interconnect loss	JPL	-	14	3.34	1792
LNA - includes interconnect loss	JPL	-	14	3.34	1836
Filter	MSL	-	-1.25	1.25	1837
LNA - includes interconnect loss	JPL	-	14	3.34	1839
LNA - includes interconnect loss	JPL	-	14	3.34	1839
Filter	JPL	-	-2.5	2.5	1839
Waveguide-to-microstrip transition	MSL	-	-0.5	0.5	1839
Receiver gain (dB)	46.53				
Receiver noise figure (dB)	8.66				
Receiver noise temperature (K)	1839				

3.1.1 Predicted Gain Requirements

The same constraints that drove the 92 GHz gain requirements apply to the 166 GHz design. The ideal system gain presents a signal to the detector that is just below the edge of its square law region. Four gain stages were used to amplify the RF signal level. Using Equation (2-2), with an input temperature of 600 K, a bandwidth of 5.1 GHz, and the gain and noise figure shown in Table 3-1, the signal level at the power detector can be calculated to be –21 dBm. The power detector used in this design remains in the square

law region with input powers up to –20 dBm. The detector has a sensitivity of 318 V/W. This predicted input power level results in a 2.5 mV output signal from the power detector.

3.1.2 Predicted System Noise Temperature

The predicted system noise temperature is 2143 K, as shown in Table 3-1. The predicted noise temperature of this receiver is much larger than that of the 92 GHz receiver. This is mainly due to the higher insertion loss of the components prior to the first gain stage, especially the coupler and the Dicke switch. These are the lowest loss components that could be found at the time of the design. The predicted radiometric resolution for this noise temperature is shown in Figure 3-2. This radiometric resolution plot assumes a Dicke mode of operation, an antenna temperature of 100 K, and normalized gain variations, ΔG/G, of 0.0005.

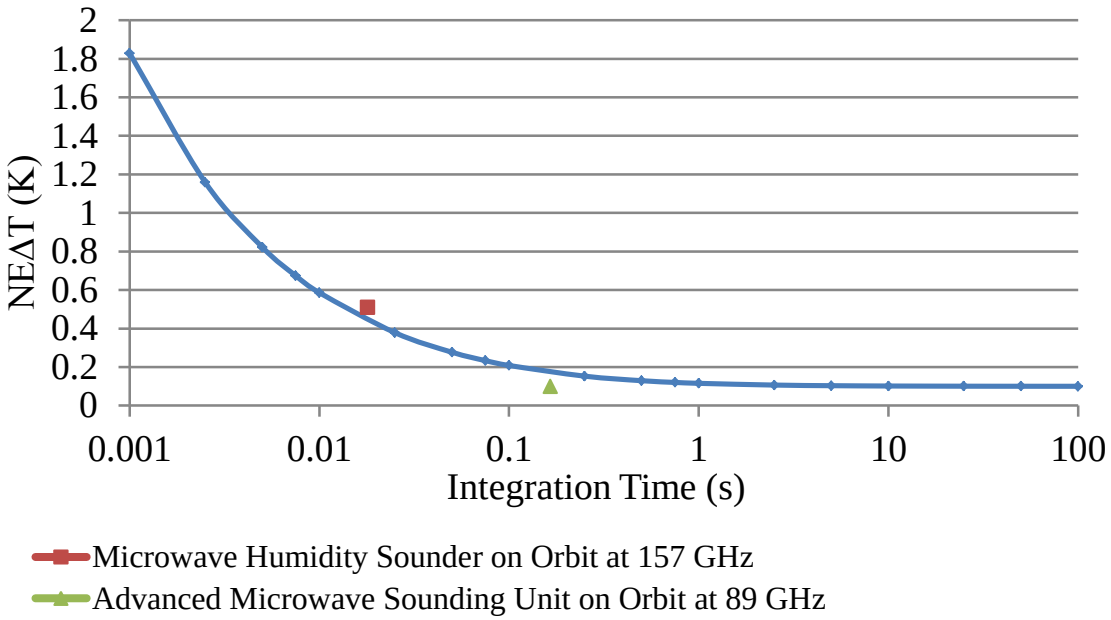

Figure 3-2. Predicted radiometric resolution for 166 GHz receiver

3.2 166 GHz Component Design and Measurement

3.2.1 Custom Designed Passive Components

The following custom designed passive components were all designed and simulated at the MSL at CSU. They were tested by CSU students at JPL, due to the availability of test equipment at JPL in this frequency band. The components were fabricated at ATP, on 3 mil thick polished alumina substrates. Substrates of 3 mil thickness were used, as opposed to the 5 mil thick substrates used for the 92 GHz design, to avoid any parallel plate waveguide propagation modes in the substrates. The cutoff frequency for TE_1 and TM_1 dominant parallel plate waveguide modes is approximately 377 GHz for 5 mil thick alumina, and 628 GHz for 3 mil thick alumina. This thinner substrate pushes the parallel plate waveguide cutoff frequency well above the third harmonic of the operating frequency. Alumina was used for the same reasons mentioned in Section 2.2.1.

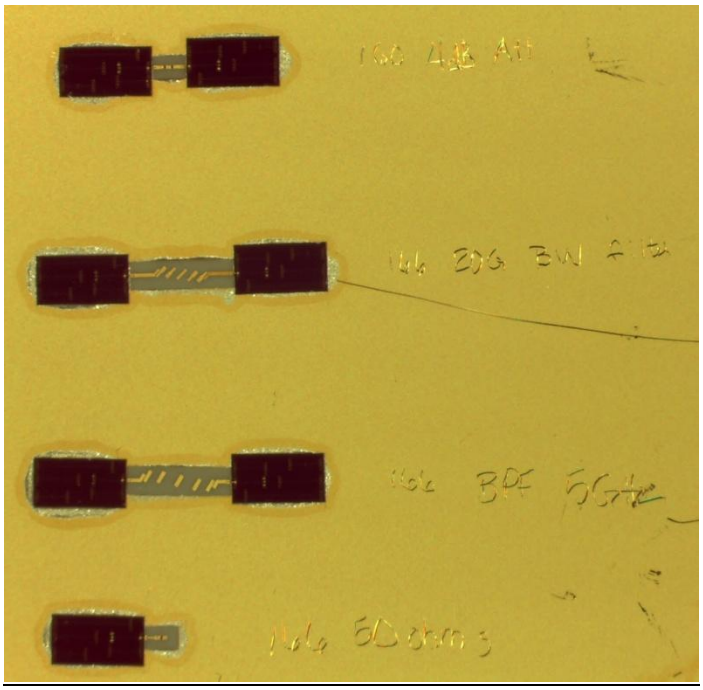

Figure 3-3. Custom designed passive components for 166 GHz mounted on a gold substrate and ready to be tested

3.2.1.1 Bandpass Filter

The bandpass filter defines the bandwidth over which the receiver detects electromagnetic radiation. The bandwidth of the receiver affects the power level at the detector, as well as the system's radiometric resolution. The 166 GHz design uses two bandpass filters, a wideband filter just after the second gain stage and a narrowband filter just after the fourth gain stage. The purpose of the first filter is to limit the power by limiting the bandwidth going to the third and fourth gain stages. It is important to limit the power to avoid saturating the later gain stages. The narrowband second filter sets the system bandwidth.

The filter types and orders are identical to the 92 GHz design. Several filter options were considered for the 92 GHz design, and this filter topology was deemed to be the best. The filters use microstrip transmission lines due to the ease of wire bonding.

The same iterative design process was used for the high frequency filters as for the 92 GHz filter. Hand calculations were completed for the initial filter design. The hand calculations were verified using Ansoft Designer, an analytical circuit simulation tool. The design was optimized using Ansoft Planar EM, a 2.5D simulation program. Finally, the design was fine-tuned using Ansoft HFSS 3D simulation program. An image of the HFSS filter model is shown in Figure 3-4.

The design was fined tuned in both the 2.5D tool and HFSS using the built in optimization function. This function allows the user to set design goals, e.g. return loss greater than 20 dB, and specify variables that can be tuned to meet these goals. Once the optimization setup is complete, the software tries to find the best variable values that meet the design goals. For these filters, variables were created for the resonator length, width, and spacing. A variable was also created for lid height. This optimization tool allowed much of the time consuming fine tuning work to be automated. It also resulted in a design that better met the design requirements than the 92 GHz design. This is especially impressive since the Q of this filter is 33, which is much higher, and therefore harder to realize, than the Q of 18 of the 92 GHz filter.

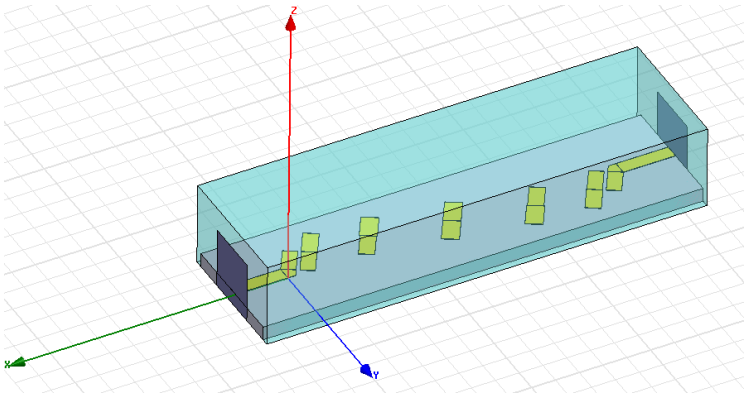

Figure 3-4. HFSS model of the 166 GHz narrow bandwidth filter

An attempt was made to integrate coplanar waveguide ports on the filter edges. This would make wafer probing of these components easier and more accurate. With the thin substrate being used and the required spacing between the ground planes and the center conductor, coplanar waveguide ports were not possible due to ATP's design rules. ATP's minimum required spacing between a via and an adjacent pad, as well as the required metallization surrounding a via, made it impossible to attain 50-ohm lines. Future designs using thicker substrates should include these ports whenever possible.

The HFSS simulated response for both the wideband and narrowband filters are shown in Figure 3-5 and Figure 3-6. The narrowband filter has a simulated 5.5 GHz bandwidth centered at 166.15 GHz, with an average of 2.5 dB insertion loss and 18.5 dB return loss across the bandwidth. The wideband filter has a simulated 20.5 GHz bandwidth centered at 165.95 GHz, with an average of 1.25 dB insertion loss and 22.29 dB return loss across the bandwidth.

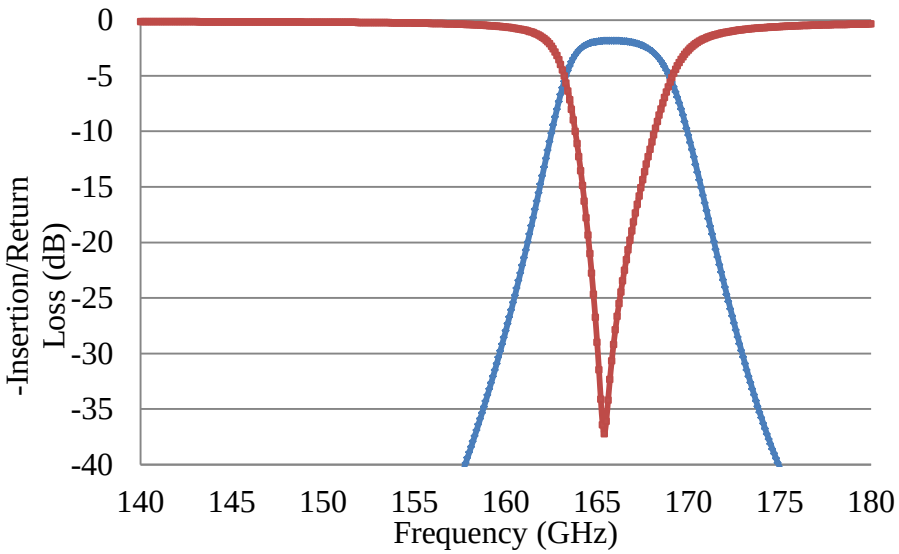

Figure 3-5. HFSS simulated narrow bandwidth filter response

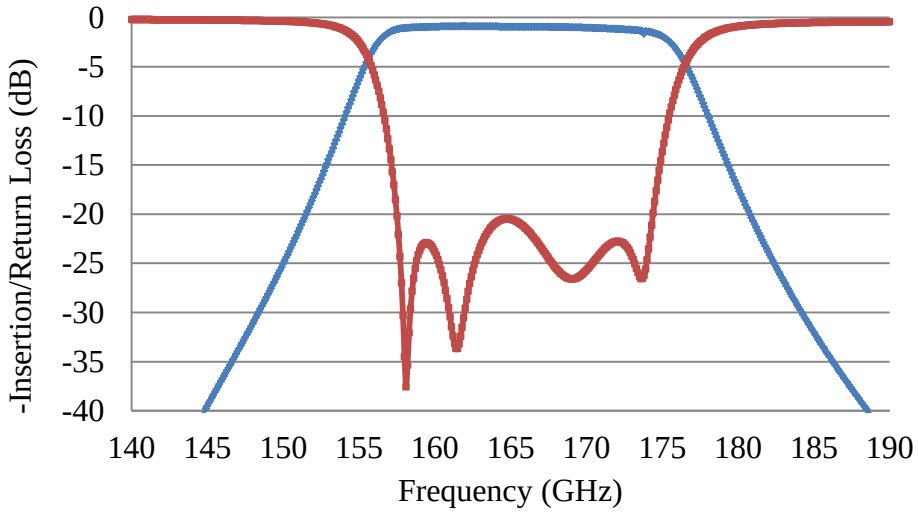

Figure 3-6. HFSS simulated wide bandwidth filter response

These filters were measured in open air using an HP 8510C vector network analyzer with frequency extension options up to the WR-5 band, OML waveguide extender heads, and a Cascade Microtech wafer probe station. Custom designed microstrip transitions were used to interface the coplanar waveguide wafer probe tips with the microstrip based

filters. These transitions were designed by JPL and fabricated on the same InP wafer as the PIN diode switches. Images of the microstrip transitions and the filters are shown in Figure 3-7 through Figure 3-9.

Two microstrip transitions were wire bonded together and measured. The measured insertion loss due to the two transitions was de-embedded from the filter insertion loss data prior to plotting the results in Figure 3-10 through Figure 3-12. The measured narrowband filter response compares well with the simulated response. The measured wideband filter response is shown in Figure 3-13 and Figure 3-14.

Figure 3-7. Microstrip transmission line used to interface with the wafer probe tips.

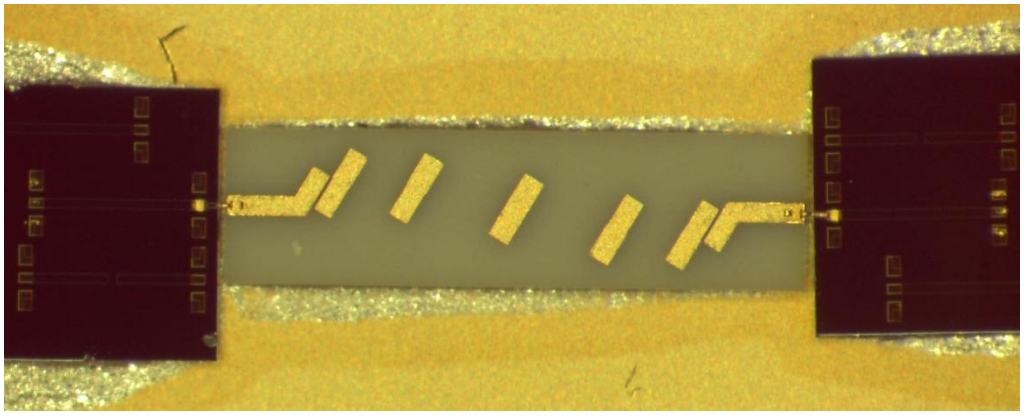

Figure 3-8. 166 GHz narrowband bandpass filter

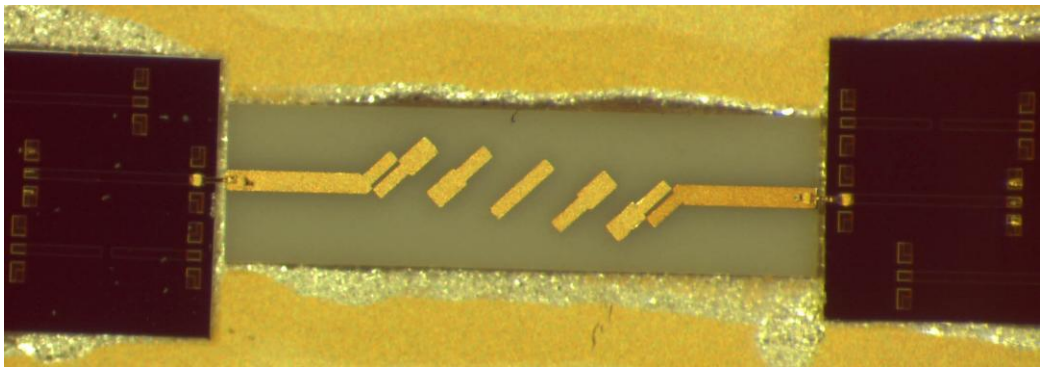

Figure 3-9. 166 GHz wideband bandpass filter

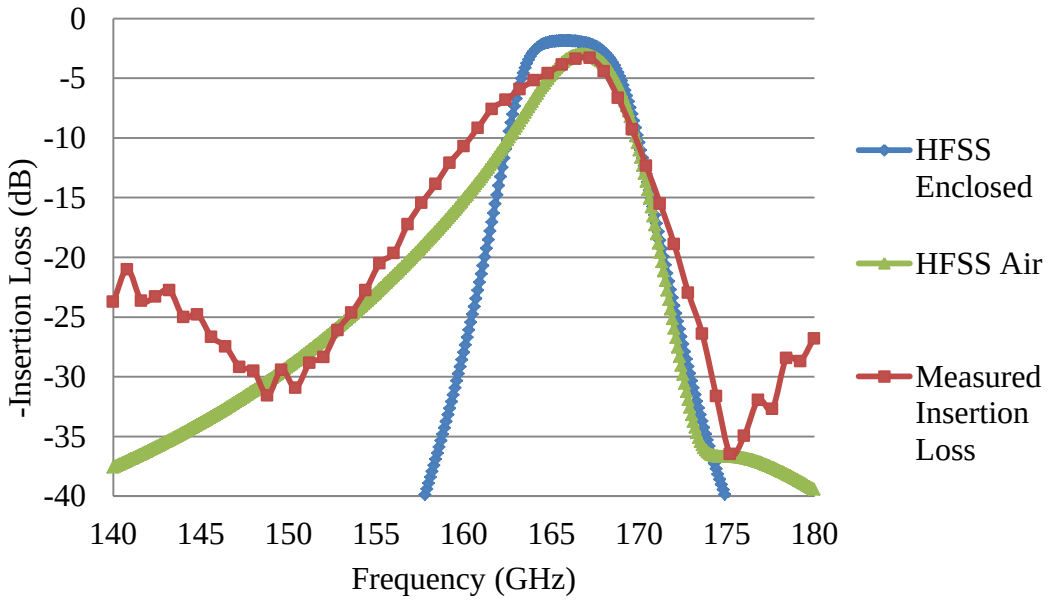

Figure 3-10. Comparison of measured and simulated insertion loss response for the 166 GHz narrowband filter

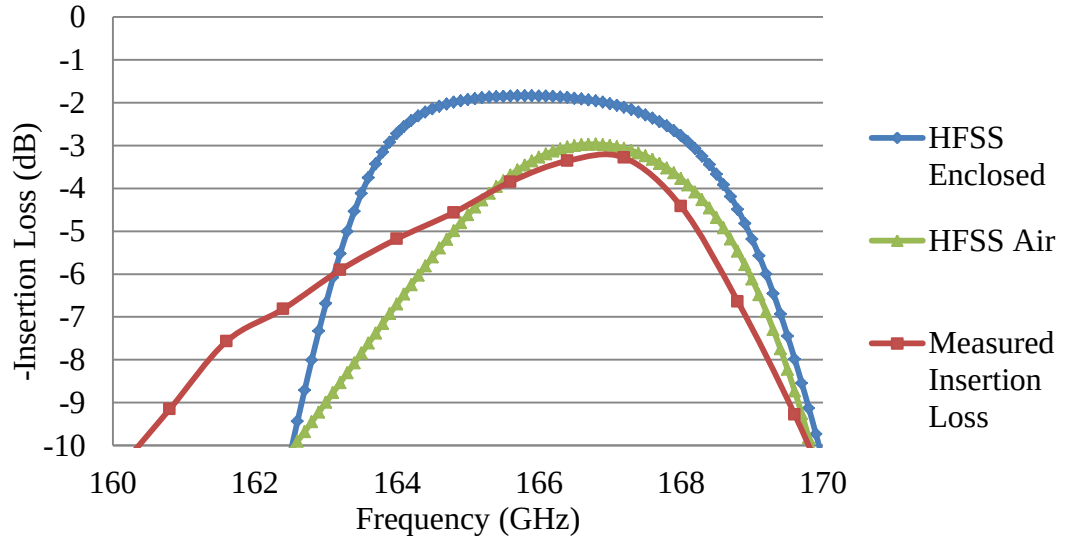

Figure 3-11. Pass band comparison of measured and simulated insertion loss for the 166 GHz narrowband filter

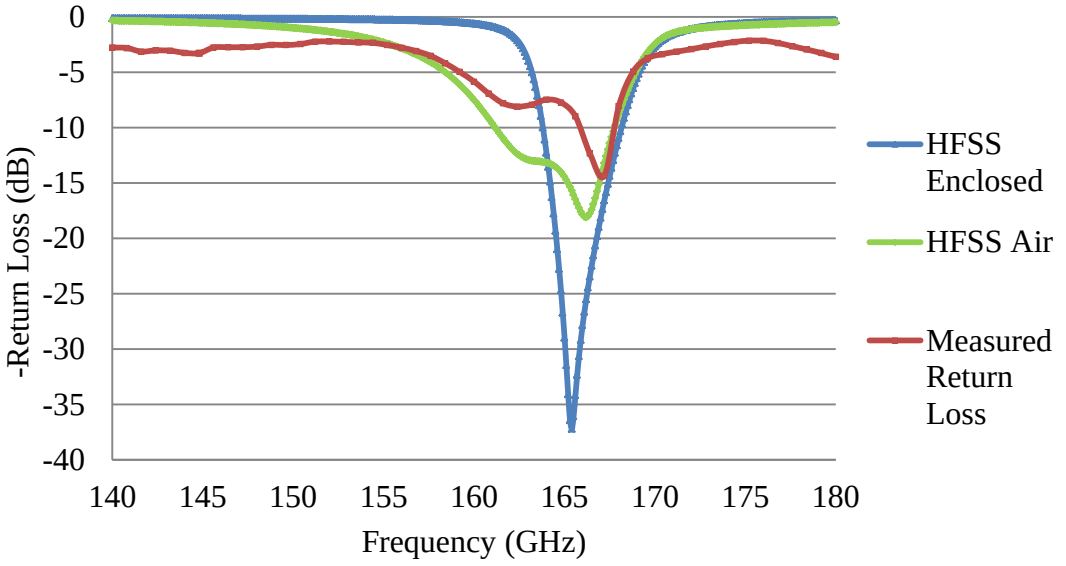

Figure 3-12. Comparison of measured and simulated return loss response for the 166 GHz narrowband filter

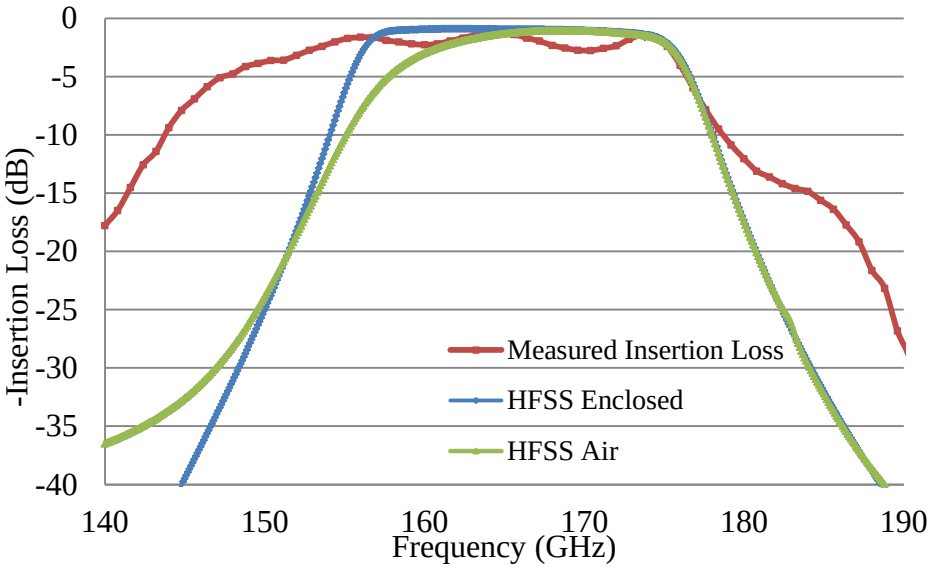

Figure 3-13. Comparison of measured and simulated insertion loss response for the 166 GHz wideband filter

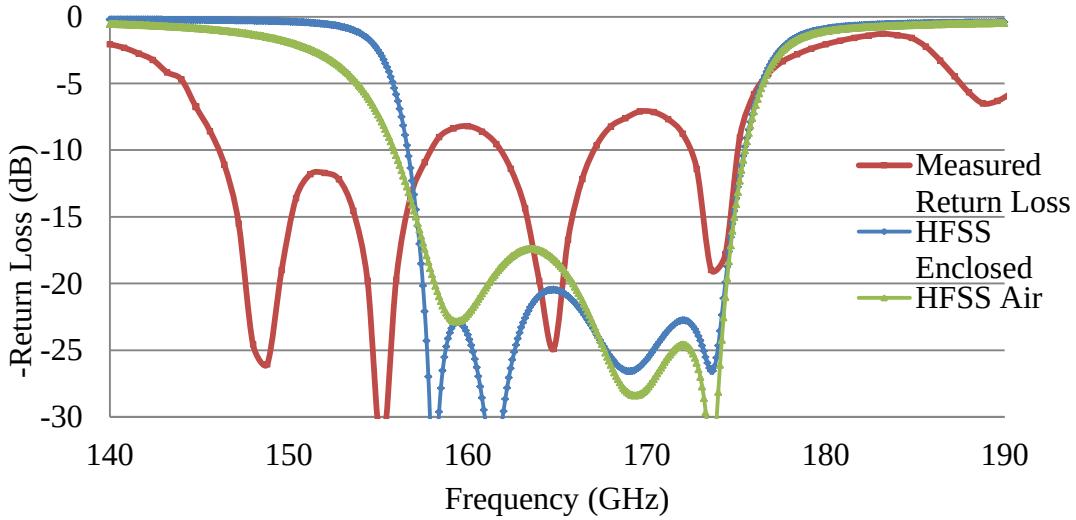

Figure 3-14. Comparison of measured and simulated return loss response for the 166 GHz wideband filter

The wideband filter measurements do not compare with simulation results as well as the narrowband filter measurements do. This poor comparison could be due to assembly issues, e.g. wire bond length or silver epoxy uniformity, or measurement errors, e.g. one

or both of the probes was not making good contact, or it could be due to fabrication issues. It is difficult to tell if this is the actual response of the component and if there will be an equally poor response once it is in a cavity. The loss from the microstrip transitions was de-embedded from the insertion loss measurement in the same manner as was done for the narrowband filter.

As poorly as this response matches the simulated response, it will still work in the design. There is a bit more loss in the pass band, the bandwidth is larger than designed, and the match is not as good as designed, but none of these issues will drastically affect the overall system performance.

Due to the problems encountered with the 92 GHz test fixture, a test fixture was not fabricated for the 166 GHz designs.

3.2.1.2 Matched Load

The 166 GHz matched load serves the same purpose and utilizes the same design philosophy as the 92 GHz matched load. The integrated resistor is composed of the same material as the 92 GHz, although the resistance in the 166 GHz design is 50 ohms per square as opposed to 25 ohms per square in the 92 GHz design.

The main difference between the 166 GHz design and the 92 GHz design is the 166 GHz design's integrated wire bond impedance matching network. Wire bonds have a large impact on component performance at 166 GHz. In an attempt to eliminate the effects of

wire bond impedance, a matching network was included on the chip to tune out the wire bond impedance and maintain a good match. The matched load HFSS model, including wire bond, is shown in Figure 3-15.

The wire bond matching network is optimized to tune out wire bonds with specific dimensions. If the wire bond does not match these dimensions, the match will not compare well with the simulated response. The modeled wire bond rises 1 mil (25.4 μm) above the matched load bond pad and comes down at a 45º angle to a 2 mil high substrate that is located 1 mil away from the matched load. The technicians at JPL assisted in the assembly of the open air measurements, as well as the MCM assembly. A photograph of the assembled 166 GHz matched load is shown in Figure 3-16. The JPL assembly technicians were able to closely replicate the wire bond model; this can be seen from the good agreement between the simulated and measured open air response in Figure 3-17.

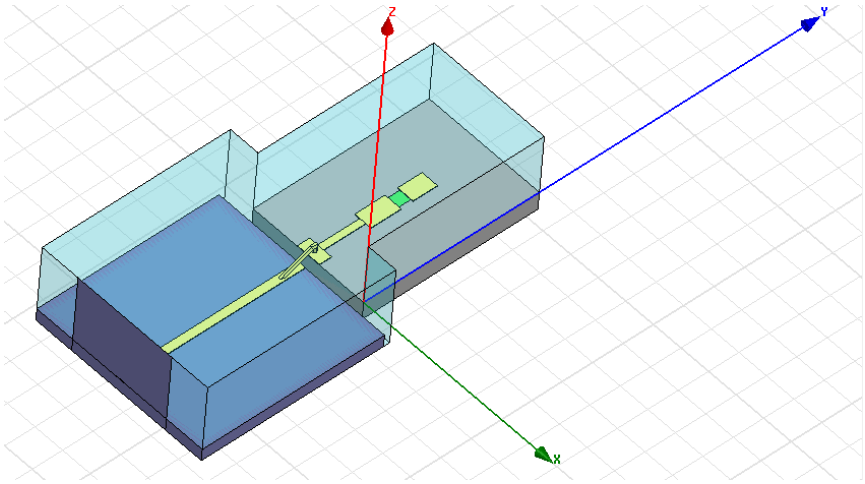

Figure 3-15. 166 GHz matched load HFSS model, including wire bond

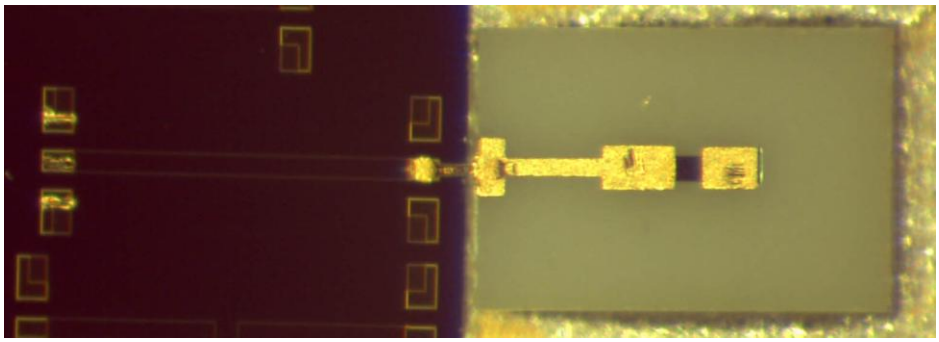

Figure 3-16. 166 GHz matched load and microstrip transition

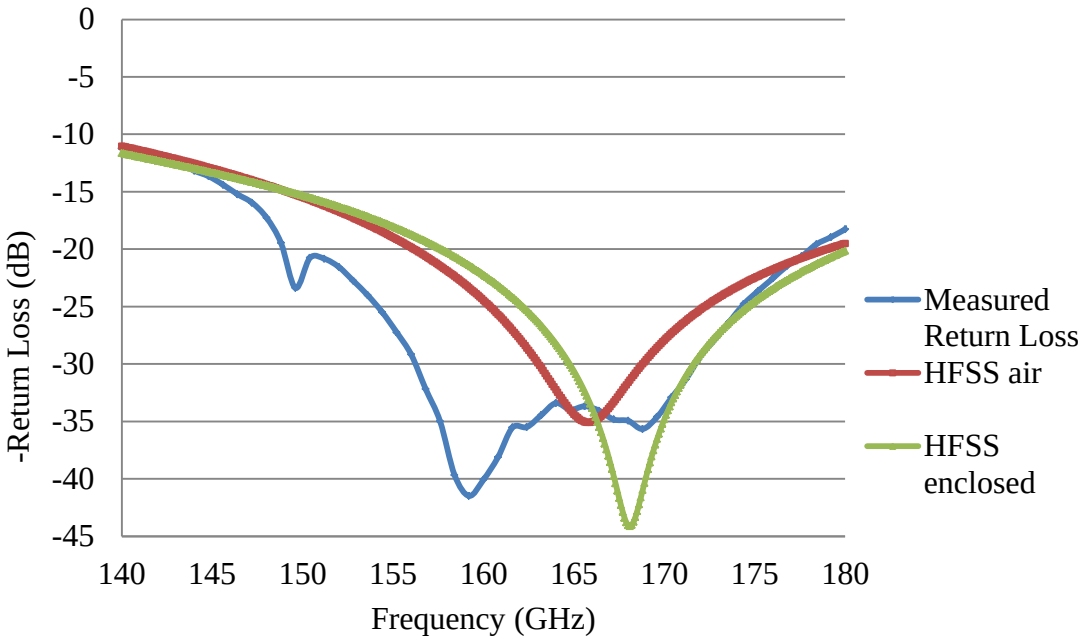

Figure 3-17. Measured return loss of the 166 GHz matched load

3.2.1.3 Waveguide-to-microstrip transition

A detailed explanation of the waveguide-to-microstrip transition's purpose and the design process was given in Section 2.2.1.3. These points did not change for the 166 GHz design. The only differences in the 166 GHz design, besides operating frequency, are the different probe shape and the inclusion of a wire bond matching network.

The 166 GHz waveguide to microstrip design has a taper at the end of the probe section that is closest to the RF trench. If the transition is not properly aligned in the RF trench, i.e. the probe is not completely in the waveguide, additional parasitic capacitance can be created that will degrade the performance of the transition. This parasitic capacitance is due to the capacitance between the large probe, which has no underside metallization, and the bottom of the RF trench. If the transition is properly aligned, the probe is not located above the RF trench and this parasitic capacitance will not be an issue. The tapering reduces the amount of parasitic capacitance created from misaligning the transition. The HFSS model and a photograph of the waveguide-to-microstrip transition are shown in Figure 3-18 and Figure 3-19, respectively. The tapered probe is shown on the right side of the photograph, and the integrated wire bond cancellation network is shown on the left.

Similar to the 166 GHz matched load, the waveguide-to-microstrip transition has an integrated wire bond impedance matching network. In exactly the same manner as the matched load, the effectiveness of this network depends on how closely the actual wire bond matches the simulated wire bond.

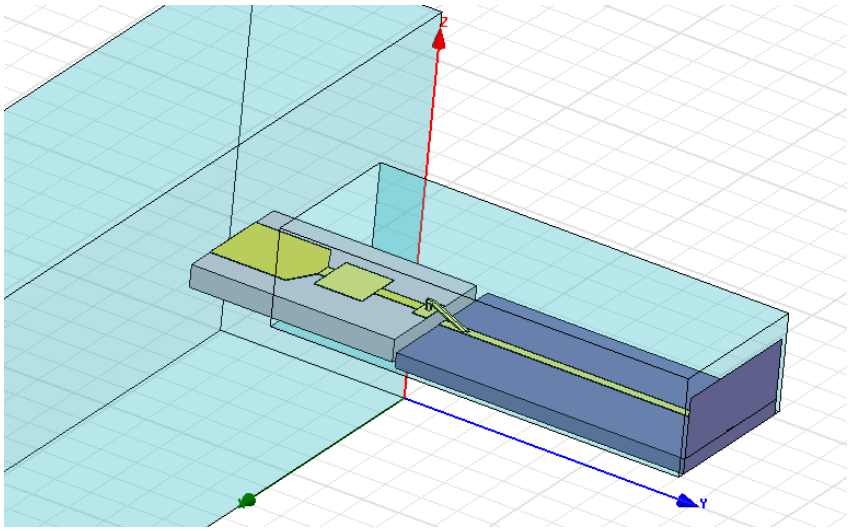

Figure 3-18. HFSS model of 166 GHz waveguide-to-microstrip transition, including wire bond

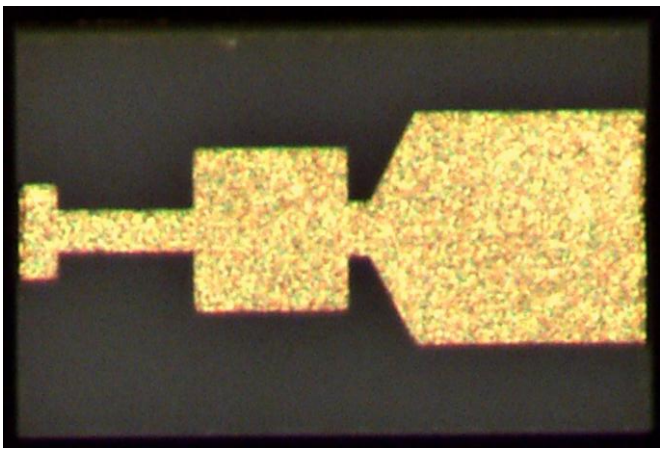

Figure 3-19. 166 GHz waveguide-to-microstrip transition

3.2.2 Commercially Available Components

Commercially available components were used for the 166 GHz waveguide based components. These included both the coupler and power detector.

3.2.2.1 166 GHz Coupler

The coupler is produced by ELVA, the same manufacturer that produced the 92 GHz coupler. The same coupling factor was used and, therefore, the same ENR is required of the 166 GHz noise diode as was required of the 92 GHz noise diode.

The coupler performance plots, Figure 3-20 through Figure 3-22, were provided by the vendor and were not measured by the author. The original coupler that was shipped from the vendor was measured and did not meet the specifications. ELVA shipped a replacement coupler with the included measured performance plots. Unfortunately, due to time and budget constraints, these measurements were not verified by the author. CSU does not have WR-5 measurement capability so these measurements would need to be performed at JPL.

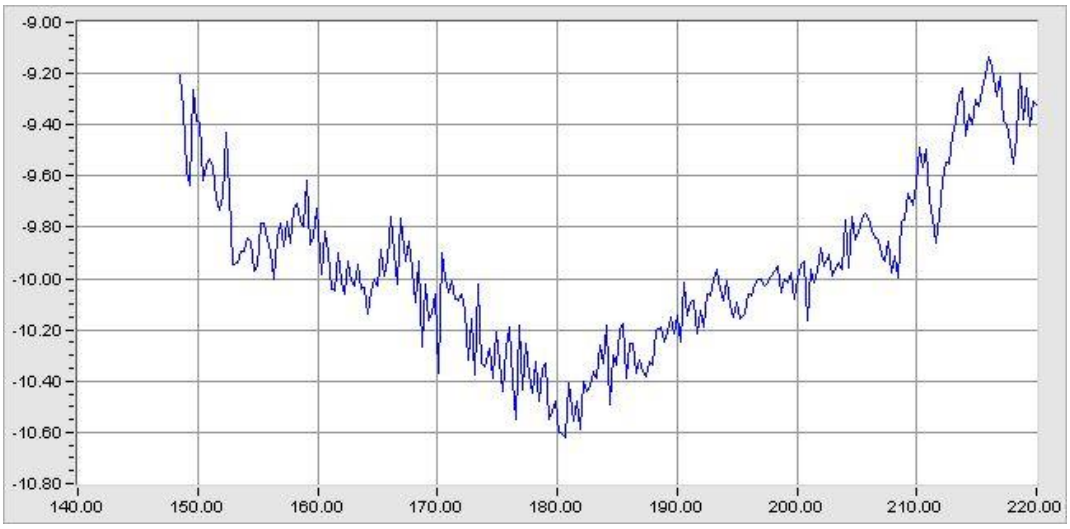

Figure 3-20. 166 GHz coupler vendor-measured coupling performance

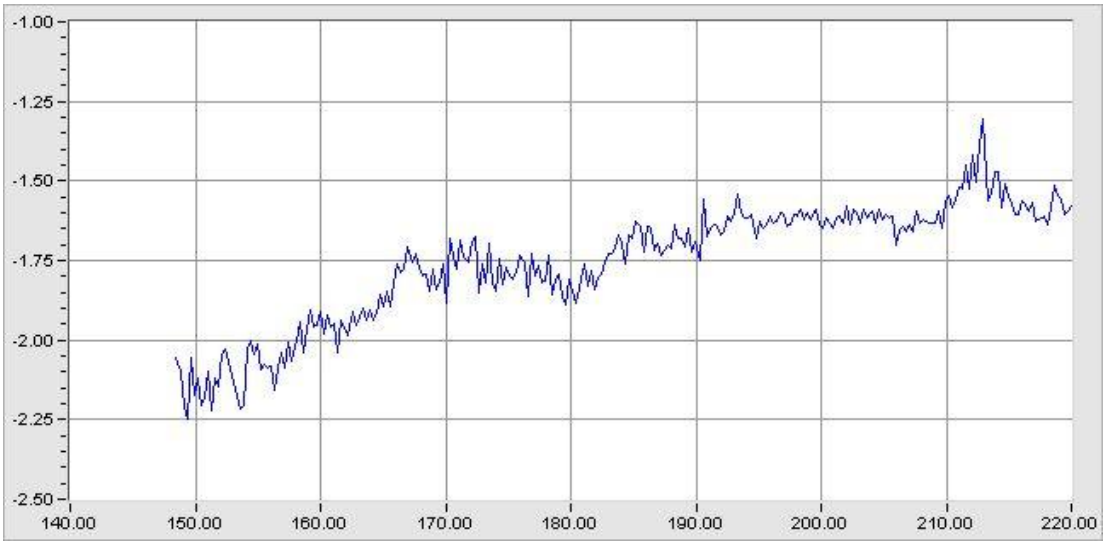

Figure 3-21. 166 GHz coupler vendor-measured transmission loss

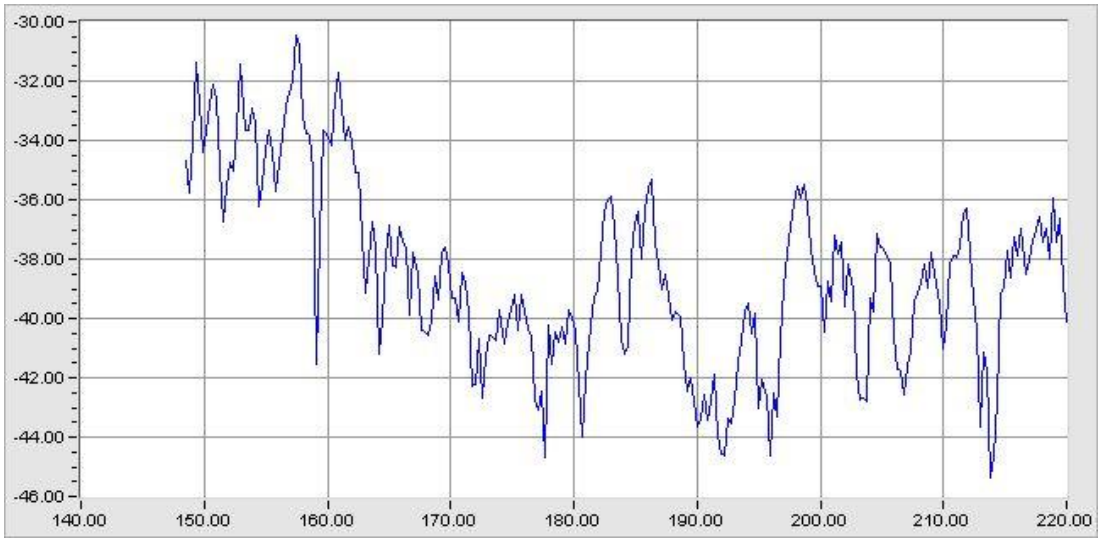

Figure 3-22**.** 166 GHz coupler vendor-measured directivity

3.2.2.2 166 GHz Power Detector

A waveguide based power detector was used in the 166 GHz design. It was manufactured by Pacific Millimeter, model GD. A waveguide based power detector was chosen because commercially available MMIC power detectors were not available. An added benefit of the decreased level of integration, i.e. the waveguide output on the MCM, is that it simplifies troubleshooting and characterizing the RF section.

The waveguide power detector is much less sensitive than the MMIC based power detector used in the 92 GHz design. It has a β of 318 V/W, averaged over the radiometer bandwidth, as opposed to the 92 GHz detector's sensitivity of 13,500 V/W. However, this power detector remains in the square law region with signals as large as –20 dBm. This is an order of magnitude larger than the 92 GHz detector's square law limit. Input signals at

the edge of the square law region will result in a 3.2 mV output, a similar level to the measured output from the 92 GHz detector.

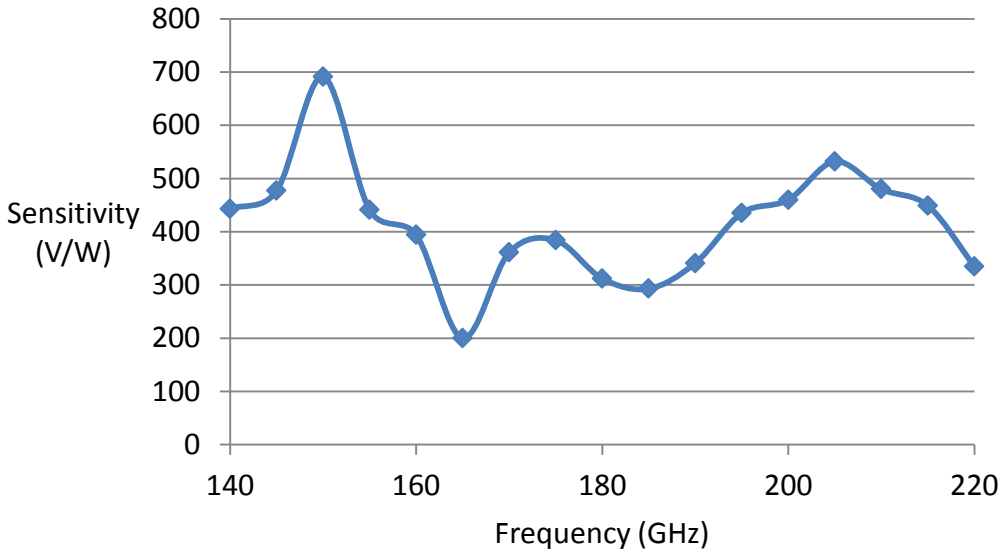

Figure 3-23. 166 GHz power detector vendor-measured sensitivity as a function of frequency

3.2.3 JPL Designed Components

The JPL designed components for the 166 GHz design include the Dicke switch, LNAs, noise source and antenna.

3.2.3.1 166 GHz Dicke Switch

This switch is similar to the 80-105 GHz design. It was designed at JPL and manufactured at Northrop Grumman using their InP MMIC PIN diode process. This is a symmetric, SPDT based design. A photograph of the switch is shown in Figure 3-24. Switching is accomplished using PIN diodes in a series-shunt configuration; as described

in detail in Section 2.2.3.1. The design uses coplanar waveguide based transmission lines, as opposed to the microstrip lines used in the 92 GHz design. The use of coplanar waveguide transmission lines eliminates the need for radial stubs or vias for RF grounds. In a coplanar waveguide configuration, the ground plane is directly adjacent to the signal conductor. This allows an easily accessible low impedance path to ground.

The switch was designed for operation between 160 and 185 GHz. The design goals were insertion loss of less than 2 dB, return loss of greater than 15 dB, and isolation of greater than 20 dB. The simulated and measured switch performance is shown in Figure 3-25 and Figure 3-26.

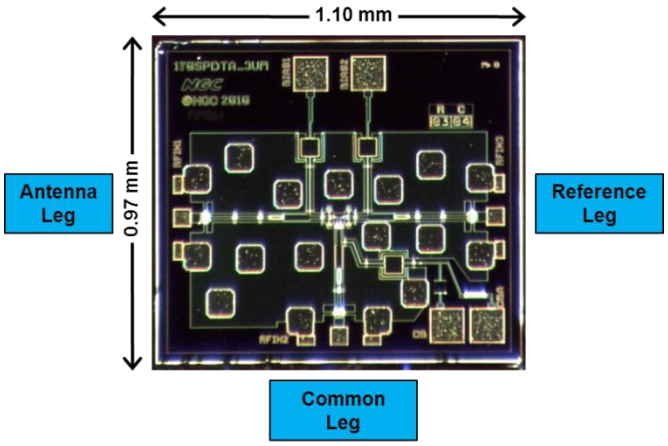

Figure 3-24. 166 GHz PIN diode switch [17]

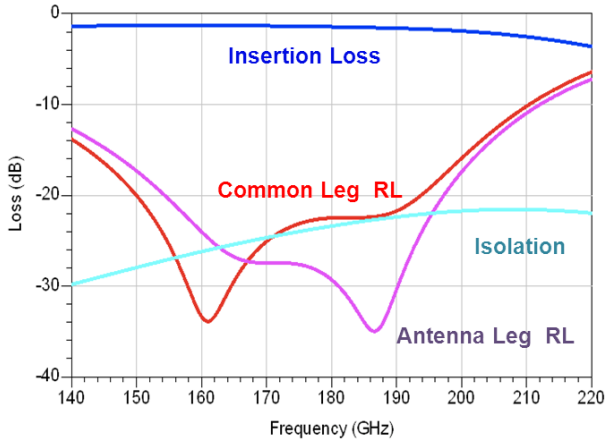

Figure 3-25. 166 GHz PIN diode switch simulated performance [17]

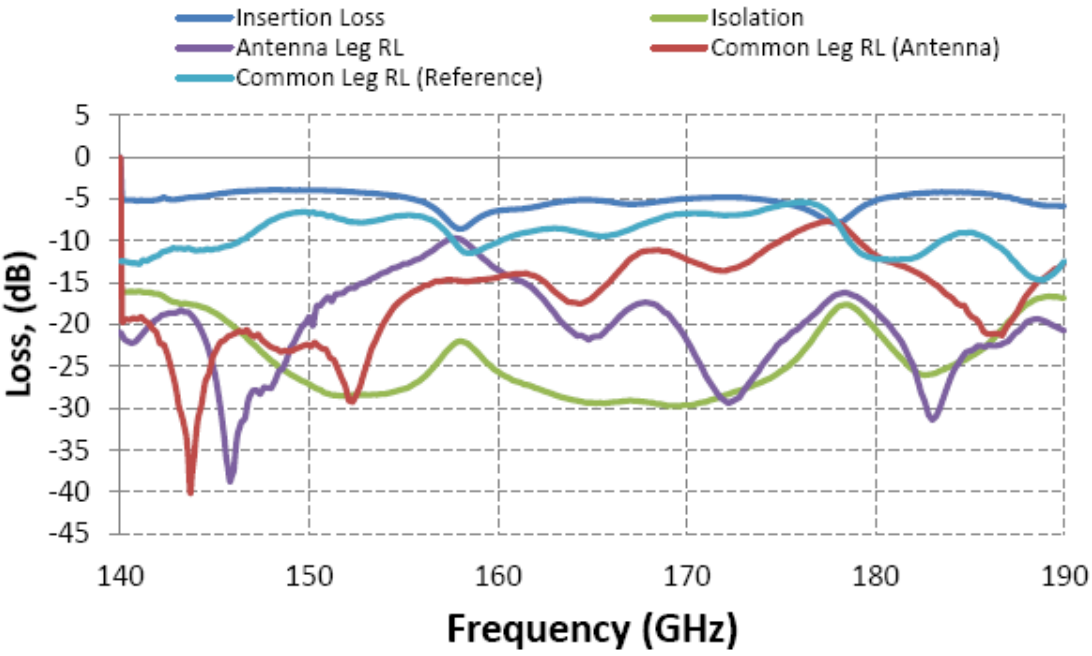

Figure 3-26. 166 GHz PIN diode switch JPL-measured performance [18]

The switch was measured in a generic WR-5 waveguide housing at JPL. The switch was tested in a housing because cavity dimensions have an effect on the component's response. Testing the switch in a housing simulates the conditions of the 166 GHz MCM. The waveguide housing included an input waveguide, an input waveguide-to-microstrip

transition, the switch under test, an output waveguide-to-microstrip transition and an output waveguide. The additional components, two waveguides and two waveguide-to-microstrip transitions, add a total of about 2 dB of loss. This 2 dB of loss is included in the measured response data shown in Figure 3-26. Over the radiometer's bandwidth, the switch has an average measured insertion loss of 3 dB, return loss of 18 dB, and isolation of 27 dB. The measured switch performance is very close to the initial design goals. The measured insertion loss is within 1 dB of the design goal. The measured return loss and isolation both exceed the design goal.

3.2.3.2 166 GHz Low Noise Amplifiers

The low noise amplifiers were designed by JPL for operation between 100 and 200 GHz. These amplifiers have an average gain and noise temperature of 17 dB and 300 K, respectively, over the radiometer's bandwidth at room temperature. More information about these amplifiers can be found in [24] and [25].

3.2.3.3 166 GHz Noise Source

Unfortunately, the measured ENR of the 166 GHz noise source was not sufficiently high to use in this system. JPL is investigating alternative noise diodes to provide the hot calibration at 166 GHz for this radiometer system.

3.3 166 GHz Multichip Module

The 166 GHz MCM is used to package the MMIC based components. It is machined from brass and gold plated. This design proved to be much more difficult for the machinist than the 92 GHz design because of the numerous areas where 0.1 mil (2.54 μm) precision was required. This required detail is due to the smaller wavelength at 166 GHz than at 92 GHz. The 166 GHz MCM was designed using SolidWorks.

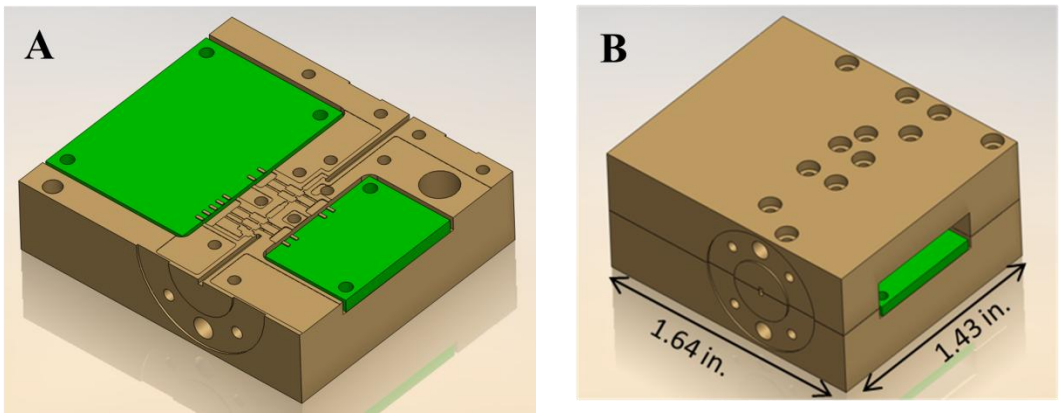

Figure 3-27. SolidWorks model of 166 GHz MCM. (A) Housing with lid removed and (B) complete MCM

The 166 GHz MCM is a split block design with the floor of the RF trench in the bottom half and the ceiling of the RF trench in the top half. The MCM provides input and output waveguides to interface with the coupler and power detector, respectively. The waveguides are standard G-band WR-5 waveguides with dimensions of 51 mils (1.30 mm) and 25.5 mils (0.65 mm). The input waveguide was designed to be as short as possible in order to reduce loss prior to the first gain stage. The waveguides are split along the broad wall, the same as the 92 GHz MCM, to further reduce loss, as described in Section 2.3.

The RF and biasing trenches act as waveguides. The dimensions of the RF and biasing trenches were carefully designed to be certain that their waveguide cutoff was far above the system's operating frequency. All of the biasing trenches include at least 40 mils (1.02 mm) of trench with a broad wall dimension of 12 mils (0.30 mm). This corresponds to a cut off frequency of 492 GHz. The RF trench includes interconnects between all of the components. Around these interconnects the trench narrows down to 13 mils (0.33 mm) wide, corresponding to a cutoff of 454 GHz.

At these high frequencies, low-noise amplifiers are prone to instability when mounted in a cavity. This is because the size of the amplifier corresponds to a cavity resonance in the amplifier's frequency range of operation. Therefore, the cavities that house the LNAs are very wide, 87.2 mils (2.21 mm), to ensure that the cavity resonance is outside of the amplifier's operating frequency range. Also, the wide cavity allows room for microwave absorber to be inserted if stability problems arise.

Grounding of the MCM is established through the use of a single large gauge, 14 AWG, wire that is connected with spade connectors between a bolt on the MCM and one of the standoffs on the back-end board. In order to have a consistent ground, the same contact points on the MCM and the back-end board were always used. As discussed previously, the use of a single ground connection is important to avoid ground loops. The offset ground voltage, i.e. the difference in the ground voltages of the back-end board and

MCM, was measured to be on the order of 100 μV, with the MCM at the higher voltage, when all of the LNAs were biased on.

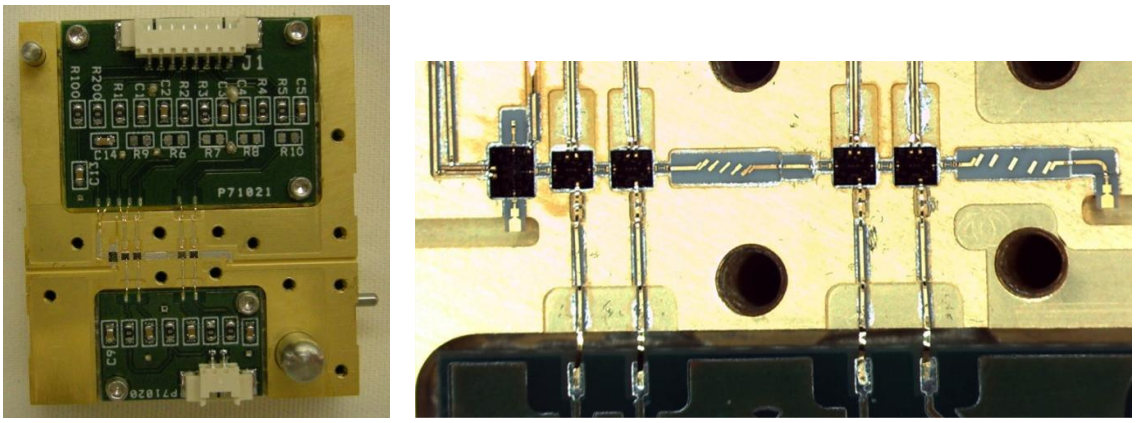

Figure 3-28. 166 GHz fully-assembled MCM

3.4 Bias Boards

The 166 GHz radiometer includes two biasing PCBs inside of the MCM. These boards were fabricated using standard FR4 copper clad laminates. Similar to the 92 GHz bias boards, the copper on the underside of these boards was left exposed and the boards were silver epoxied to the MCM to ensure a low impedance ground connection. All of the signal connections to these bias boards are made using discrete wire connectors with Molex Pico Blade headers and connectors. Orcad tools were used to generate schematics and PCB layout files.

The connections between the bias boards and the MMIC components were made using a parallel gap welding machine. This machine welds thick gold ribbon wire between the bond pads on the PCBs and the microstrip transmission lines in the bias trenches. As

discussed in Section 2.4, this is required because wire bonds do not make reliable connections on the tin solder coated PCB pads.

The larger of the two bias boards is used to route the switch control signals and the gate bias voltages to the four LNAs. The four LNA gate bias voltages are generated using resistor dividers on the PCB. Locating the resistor dividers on the bias board, inside of the MCM, is important because it allows the LNA and the resistor divider to have the same ground reference. This means that the calculated gate voltages will be accurate and will not be affected by different ground references. All of the gate voltages are AC bypassed with 0.1 µF capacitors located close to the bond pads.

The smaller of the two bias boards is used to route the drain voltage to the four LNAs. The drain voltage traces include zero-ohm resistors that can be removed to disconnect any of the LNAs for testing purposes. All of the drain voltage lines include 0.1 µF AC bypass capacitors located near the bond pads.

3.5 166 GHz Radiometer Testing and Performance

The same metrics discussed in the 92 GHz testing section were used to determine the 166 GHz radiometer's functionality and performance. These metrics are system noise temperature and system stability. The internal calibration stability was not tested due to the lack of a noise diode.

3.5.1 Measured vs. Calculated System Gain

Unlike the 92 GHz radiometer, no system architecture changes occurred during the radiometer design, so the original gain table, Table 3-1, can be compared with measured results. The calculated gain can be compared with the measured gain by comparing the measured output voltage level and temperature sensitivity with their predicted values.

The predicted gain and noise temperature of the system are 46.5 dB and 1840 K, respectively. Using Equation (2-2), with the narrowband filter's simulated bandwidth of 5.5 GHz, the predicted power level delivered to the detector is –21.4 dBm. With a detector sensitivity of 318 V/W, the output voltage for this power level should be 2.3 mV. The measured output voltage is 0.711 mV. If the bandwidth and detector sensitivity assumptions are correct, the only thing that could cause this discrepancy is a gain difference. This corresponds to an RF gain that is 5.1 dB lower than predicted.

The RF gain can also be calculated by comparing the theoretical output voltage sensitivity with the measured voltage sensitivity. Voltage sensitivity can be calculated using Equation (2-12). The predicted voltage to temperature sensitivity at the output of the power detector is 0.950 μV/K. The measured voltage to temperature sensitivity is 0.315 μV/K. The lower measured sensitivity corresponds to a 4.8 dB difference in gain, quite close to the 5.1 dB difference mentioned above.

The disagreement between the 4.8 dB and 5.1 dB gain differences is most likely due to measurement errors. For example, the sensitivity measurement was obtained through

radiometric observations of both a hot and a cold microwave absorber. The measurements are noisy and contain data that is statistical in nature. Therefore, both the sensitivity and the radiometer output voltage have noise and uncertainty.

3.5.2 Measured Noise Performance

As discussed in Section 2.5.2, the Y-factor method was used to measure the system noise temperature. Microwave absorbers were observed at ambient temperature and LN_2 temperature, 77.6 K. This yielded a measured receiver noise temperature of 2186 K. This is within 20% of the predicted system noise temperature of 1840 K.

The Y-factor measurements at 166 GHz were much noisier than the 92 GHz measurements. This noise is believed to be due to the large system noise temperature and the small power detector output voltage. As discussed in Section 2.1.1, measuring microvolt level signals is challenging and added noise is unavoidable. The small output voltage requires a significant amount of video gain, about 61 dB.

The same measurement techniques that were discussed in Section 2.5.2 were used to determine the average radiometer output voltages at both ambient and LN_2 temperatures.

3.5.3 System Stability

Similar to the 92 GHz radiometer, stability measurements were performed by observing known scene temperatures for extended periods of time, approximately 2 hours. The Allan deviation of the output voltage was calculated to determine the maximum effective integration time.

The MCM and the back-end board are very sensitive to temperature variations. The MCM is thermally controlled with a Peltier thermoelectric cooler/heater. The back-end board and the MCM are mounted in thermally insulating foam. A photograph of the 166 GHz test setup is shown in Figure 3-29. Only the lower portion of the insulating foam on the MCM is visible, i.e. the pink block in the photo. During normal testing, both the back-end board and the visible portion of the radiometer have foam lids and bottoms. The large black object underneath the fan is a heat sink for the Peltier device. The temperature control module, which controls the Peltier current, is not shown. The radiometer stability would most likely be improved by also including a Peltier module on the back-end board.

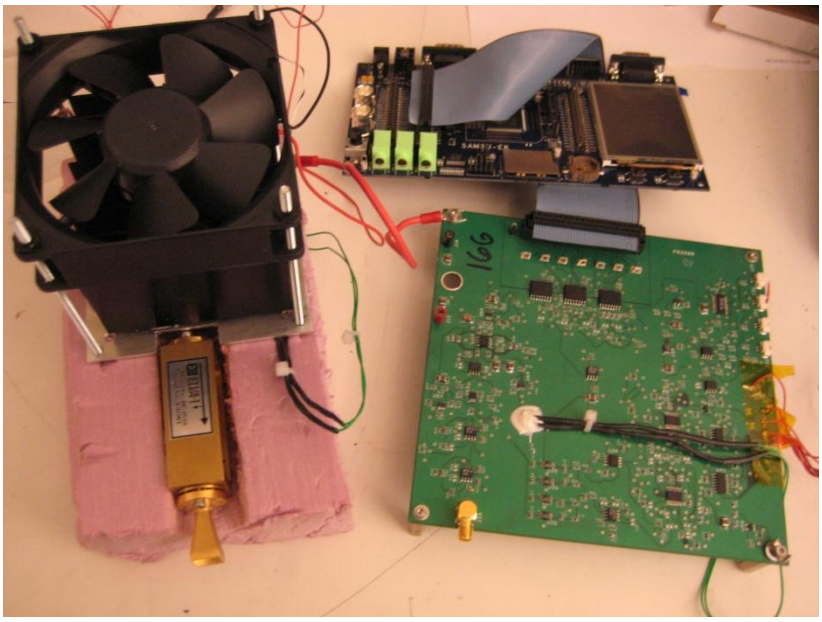

Figure 3-29. 166 GHz radiometer test setup

The radiometer was allowed time to reach thermal stability before any testing was performed. The 166 GHz radiometer reaches thermal stability in about 15 minutes. This time is much lower than the 92 GHz radiometer. This is expected to be due to the smaller thermal mass and the use of a more thermally stable operational amplifier on the video board. A time series of the radiometer voltage output during warm up is shown in Figure 3-30. The MCM and back-end board temperature variations during this same time are shown in Figure 3-31 and Figure 3-32. It can be seen that the radiometer output data stabilizes before the back-end board temperature stabilizes.

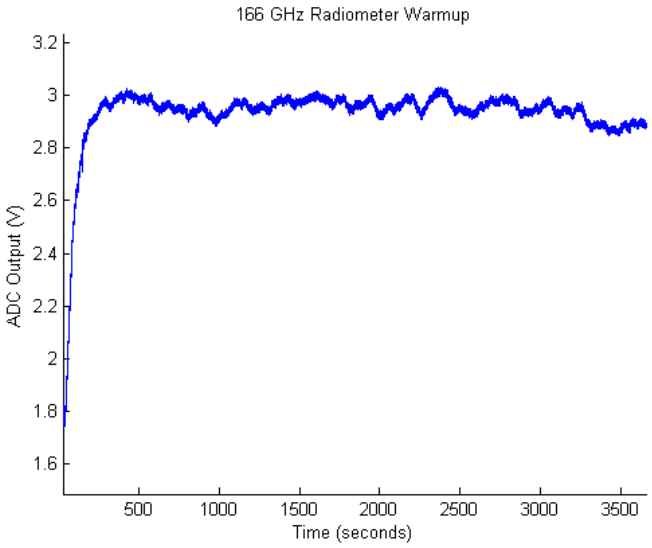

Figure 3-30. 166 GHz radiometer output versus time, illustrating system warm up time

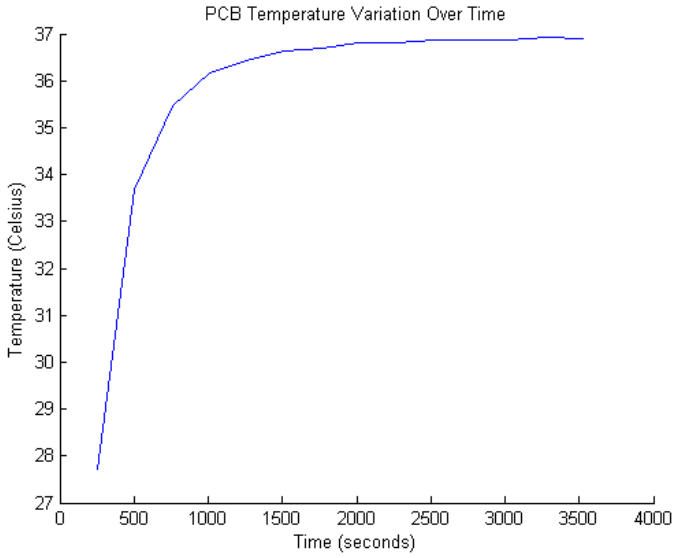

Figure 3-31. 166 GHz back-end board temperature during system warm up

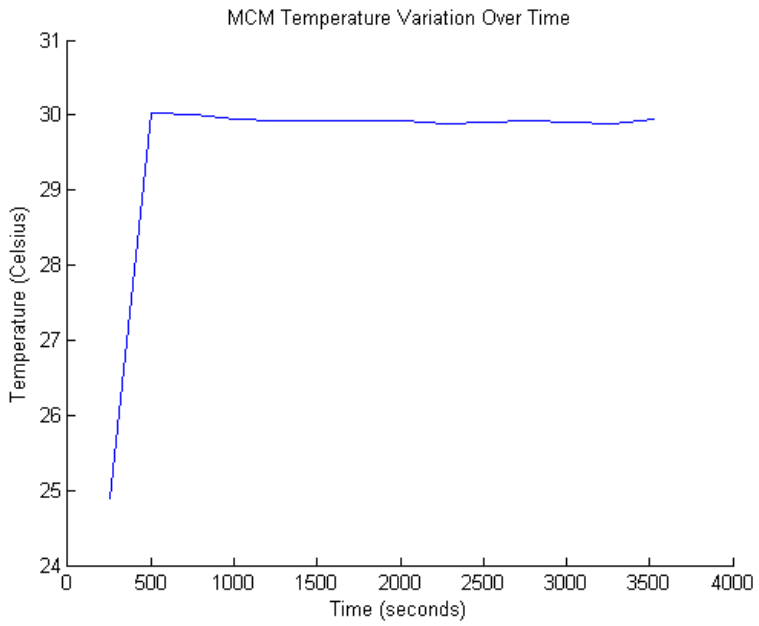

Figure 3-32. 166 GHz MCM temperature during system warm up

Allan deviation was used to quantify the stability of the 166 GHz radiometer. The definitions of Allan deviation and Allan time are discussed in Section 2.5.3. Just under two hours of data was recorded while the radiometer observed a microwave absorber at ambient temperature. The Allan time for this instrument was calculated to be 2 seconds. It is believed that this Allan time could be increased by increasing the amount of thermal control throughout the radiometer. Adding thermal control to the back-end board and encasing the system in a thermally controlled chassis would improve the system stability, and therefore increase the Allan time. Plots of the Allan deviation, the data used for the Allan deviation calculations, and temperatures of the MCM and back-end board during this Allan deviation testing are shown in Figure 3-33 through Figure 3-36.

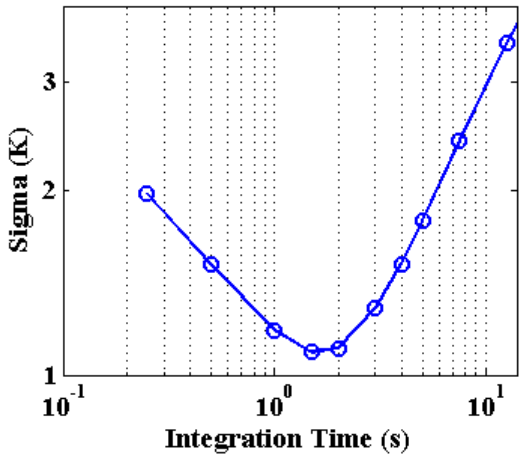

Figure 3-33. 166 GHz radiometer Allan deviation

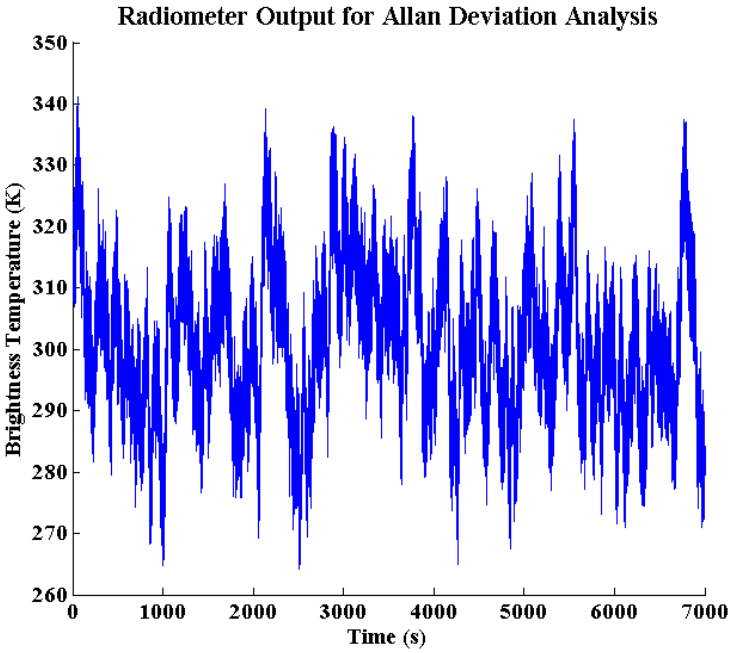

Figure 3-34. 166 GHz radiometer measured brightness temperature versus time

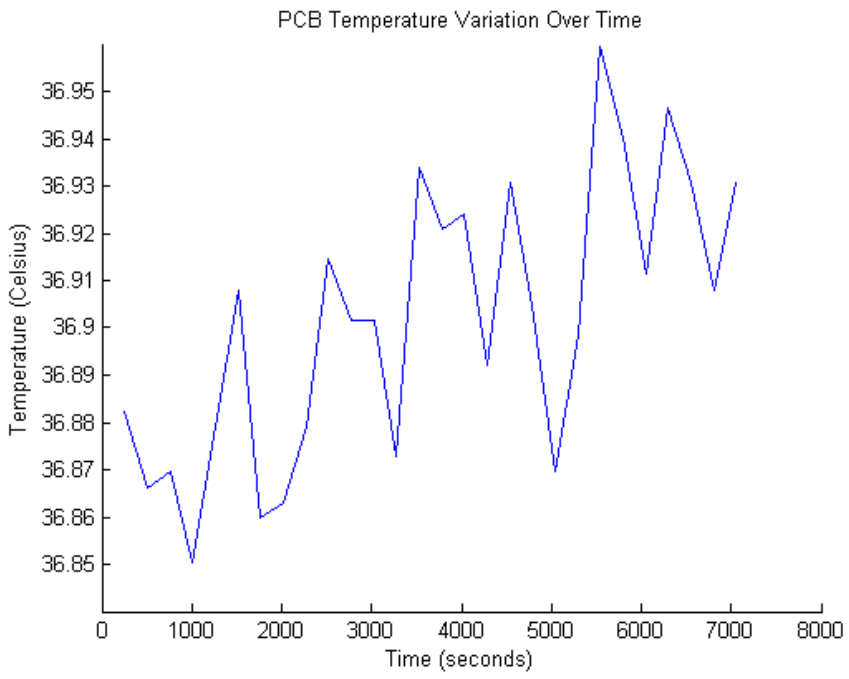

Figure 3-35. Back-end board temperature variation during Allan deviation testing

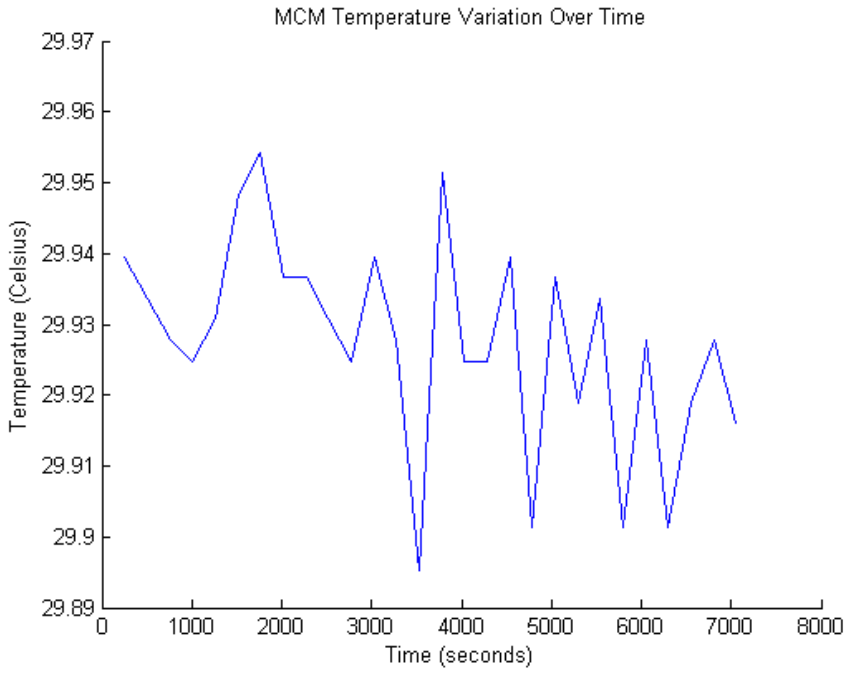

Figure 3-36. MCM temperature variation during Allan deviation testing

The radiometric resolution was calculated using the results of the measured system noise temperature and the Allan deviation testing. The normalized gain variations, $\Delta G/G$ in Equation (1-11), were adjusted until the total power radiometric resolution at integration times greater than 1 s matched the minimum Allan deviation value, approximately 1.1 K. This minimum resolution corresponds to normalized gain variations of approximately $4.5 \cdot 10^{-4}$. Using an antenna temperature of 100 K and the normalized gain variations based upon the measured Allan deviation, Equations (1-11) and (1-12) were used to calculate the radiometric resolution for total power and Dicke modes of operation, respectively. The radiometric resolution is shown in Figure 3-37.

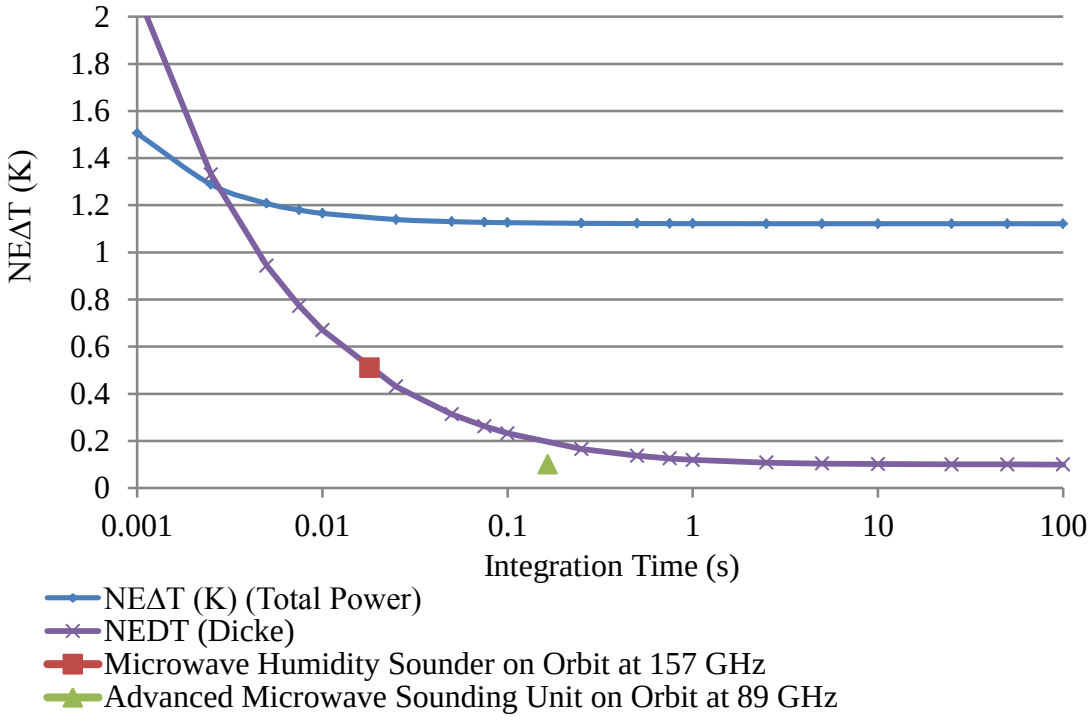

Figure 3-37. 166 GHz radiometric resolution

3.5.4 External Calibration

The steps involved in performing an external calibration are discussed in Section 2.5.4. The coefficients *a* and *b* were calculated through radiometric observations of known scene temperatures. The slope coefficient, *a*, was calculated to be 350 μV/K. The offset coefficient varies with time and temperature.

The 166 GHz radiometer was initially tested with the antenna connected directly to the MCM, with no other waveguide components. During this initial testing, the measured power at the power detector was –35 dBm, about 13 dB lower than expected. The measured system noise temperature without the waveguide components was approximately 6000 K. The radiometer was then tested with the coupler and waveguide through line between the antenna and the MCM. When the Dicke switch was in the antenna position, the measured power at the power detector was –26 dBm, close to the predicted power level. However, when the Dicke switch was connected to the matched load, the power level was still about –35 dBm. The receiver noise temperature with the waveguide components was measured to be very close to the calculated value, 2186 K. This behavior is believed to be due to matching issues with the first LNA. When a narrowband match is presented to the LNA, the LNA may be oscillating outside the bandwidth of the radiometer. The antenna and the matched load both provide a narrowband match. When the waveguide components are connected, and the Dicke switch is connected to the antenna, it is possible that the added insertion loss, due to the waveguide components, improves the antenna match and eliminates the oscillation. Due to the potential oscillation with the Dicke switch connected to the matched load, the

antenna-referred brightness temperature of the internal matched load cannot be measured. Since the system gain changes depending upon the switch position, a calibration performed through the antenna is not valid for the matched load.

3.5.5 166 GHz Mass and Power Consumption

A table with the mass of the various radiometer components is shown in Table 3-2 . This table does not include the mass of the power supplies or temperature control module. These components were not optimized for low mass, and therefore different components would be used in space-borne radiometers.

Table 3-2. 166 GHz radiometer mass

	Mass (g)
MCM and waveguide components	432
Heat sink, fan, and Peltier device	463
Back-end board	144
Microcontroller development board	197
Total	1,236

The 166 GHz radiometer power consumption is shown in Table 3-3. This table does not include power consumed by the thermal control or the microcontroller development board. These subsystems were not optimized for minimum power consumption and therefore would be designed differently for space-borne radiometers. The back-end power consumption could be reduced if some of the unused components were removed, as discussed in Section 5.4.

Table 3-3. 166 GHz radiometer power consumption

	Power consumption (W)
MCM	0.068
Back-end board	3.220
Total	3.288

Chapter 4: Data Acquisition System

4.1 Data Acquisition System Overview

The data acquisition system consists of two main components, a back-end board designed by the Microwave Systems Lab at CSU and the commercially available Atmel SAM3U-EK microcontroller development board. The overall system is responsible for providing bias and control signals to the MCM, as well as amplifying, digitizing, and recording the power detector output voltage from the MCM. The system also monitors and records crucial system information such as LNA drain current and system temperatures.

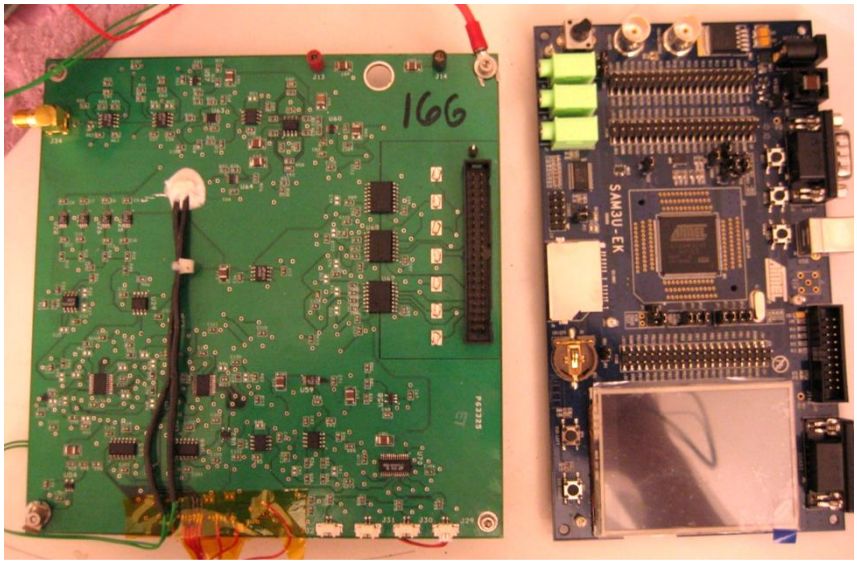

Figure 4-1. Data acquisition system with the back-end board on the left and the Atmel development board on the right.

4.2 Back-end Board

The back-end board consists of six main functional units, as follows: radiometer post-detection gain and digitization, the LNA gate voltage driver, LNA drain voltage driver, radiometer system health monitor, Dicke switch driver, and power supply regulation. A block diagram for this board is shown in Figure 4-2.

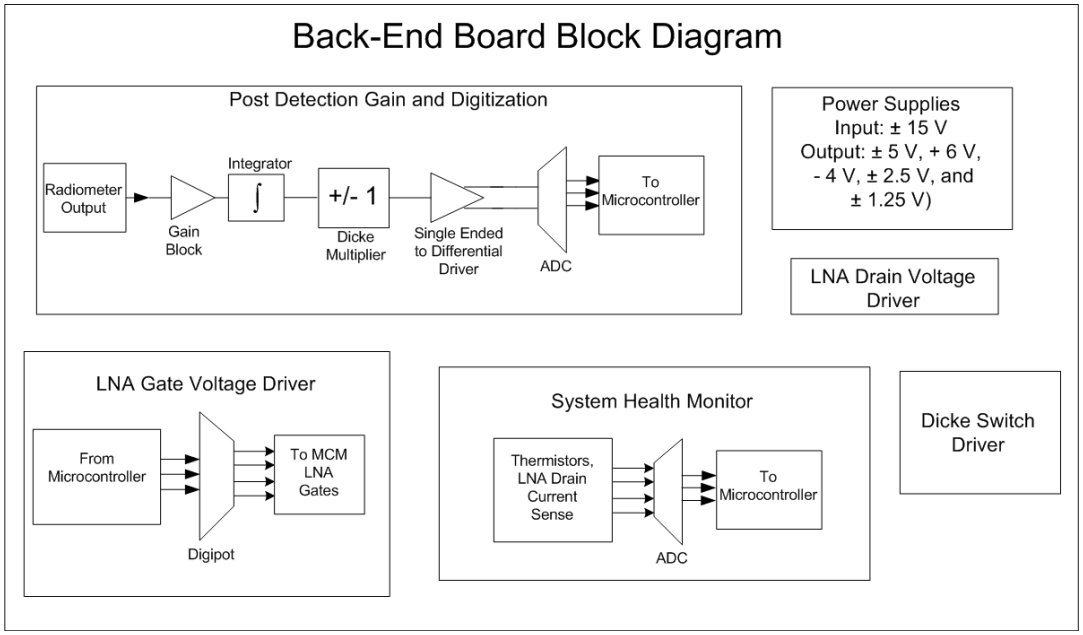

Figure 4-2. Back-end board block diagram

4.2.1 Post-Detection Gain and Digitization

The post-detection gain and digitization consists of two gain stages and a switch that redirects the radiometer signal between an inverting and a non-inverting amplifier depending on the Dicke switch position. This block also includes a single-ended to differential amplifier with a gain of two, and a 16-bit single-channel analog-to-digital

converter (ADC). The first two gain stages are Linear Technology low noise operational amplifiers, model LT1007. Their gain was set to use the maximum dynamic range of the ADC. Specifically, the gain was set so that the signal level at the ADC was near the maximum input level when the radiometer was viewing the brightest scene temperature, i.e. the noise source added to the antenna temperature of an ambient load, as described in Section 2.2.2.4.

The second gain stage has the ability to add a voltage offset to the input signal to make use of even more of the available ADC range. Since much of the signal coming from the output of the MCM is due to system noise and does not tell us anything about the scene temperature being viewed, it is desirable to add a voltage offset to the input signal. This allows the ability to only amplify the portion of the signal that corresponds to scene temperature variations. The offset voltage is set by one of the digital potentiometer outputs and is adjustable in software, as described in Section 4.3.1. A schematic of the gain/offset circuitry is shown in Figure 4-3. By putting a resistor in R_9 and leaving R_{31} open, the offset correction can be enabled, or conversely by putting a resistor in R_{31} and leaving R_9 open, the amplifier can function as a conventional gain stage. The offset voltage level depends on the ratio of the feedback resistors as

$$V_{out} = V_{in}\left(\frac{R_{18}}{R_9} + 1\right) - \frac{R_{18}}{R_9} \cdot V_{offset} \tag{4-1}$$

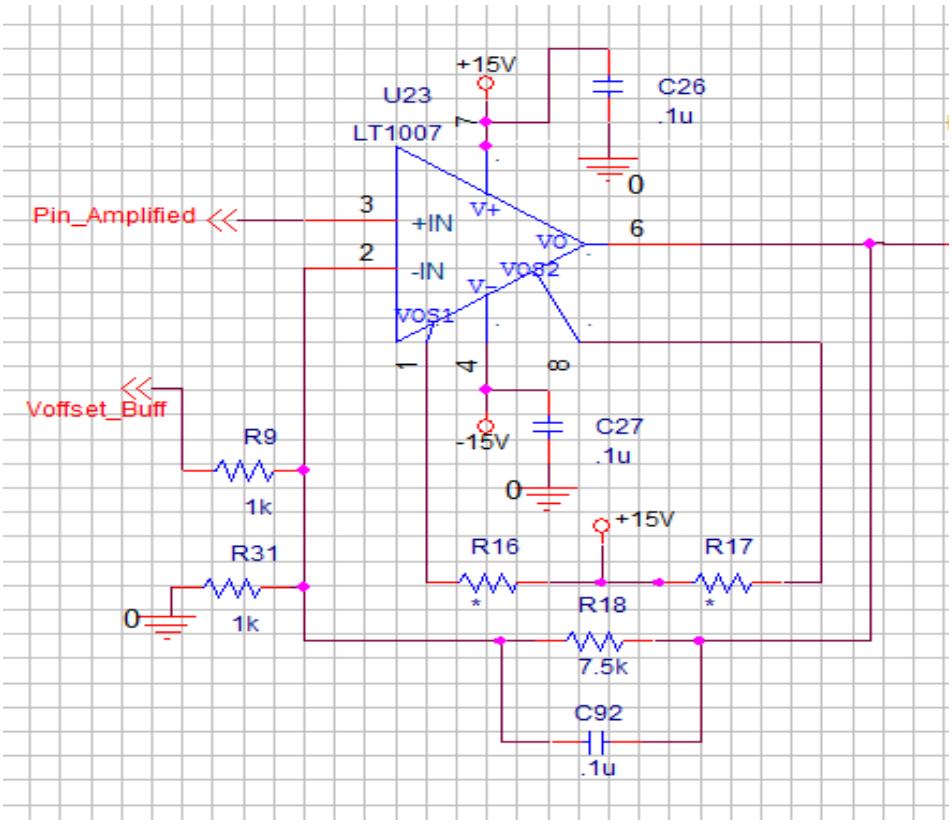

Figure 4-3. Second gain stage and offset voltage generation on the back-end board

After the second gain stage, the radiometer output voltage passes through a switch that redirects the radiometer signal between either an inverting or a non-inverting difference amplifier, INA129, depending on the Dicke switch position. This switch is the Maxim 4764. This multiplies the signal by +1 when the Dicke switch is connected to the antenna, and –1 when the Dicke switch is connected to the matched load. The switch position is controlled by the same microcontroller output that controls the Dicke switch driver. This switch position can be manually controlled through the user interface, or it will be automatically switched when the radiometer is operating in Dicke mode, as discussed in Sections 4.2.4 and 4.3.1.

The single-ended input to differential output driver, Analog Devices AD8132, is required to make use of the ADC's differential inputs and enable both positive and negative voltages to be digitized. The output of the driver is a differential signal with a common mode voltage of 2.5 V. The power supply rails on the single ended to differential driver are offset by one volt, i.e. instead of using ± 5 V rails, +6 V and –4 V rails were used. This was done because the differential driver output on either output line can only come within 1.2 V of the power supply. This offset voltage supply enables the maximum output to be 4.8 V, as opposed to only 3.8 V with a 5 V supply. A maximum voltage of 4.8 V and a minimum voltage of 0.2 V on a 2.5 V common mode voltage is equivalent to a differential output of ± 4.6 V. This differential output limits the range of inputs to the ADC to ± 4.6 V.

The single ended to differential driver is sensitive to parasitic capacitance on its input terminals. For this reason, the layout avoids any inner plane layers underneath the input of the differential driver. The input pin and any metal plane underneath it could act as a parallel plate capacitor. By removing the plane layers, the lower plate of the capacitor is removed, and the parasitic capacitance is eliminated.

The ADC is a differential, 16-bit, single channel, delta sigma ADC, i.e. Linear Technologies LTC2452. This ADC has a conversion time of 16 ms; the sampling rate is set to 50 ms with a 500 ms Dicke switch period. The ADC input range is ± 5 V, but only ± 4.6 V is being used. Communication with this device is through a serial peripheral interface (SPI), a standard communications protocol.

A 16 bit ADC with a 5 V reference has a quantization level of 76 µV. In order to achieve 0.1 K radiometric resolution, the voltage to brightness temperature sensitivity of the radiometer must yield a quantization in temperature of 0.1 K or better. The minimum radiometer voltage to temperature sensitivity can be calculated to be 760 µV/K.

4.2.2 LNA Gate Control Circuitry

The gate control circuitry is used to provide either a fixed or a user adjustable voltage to the LNA gates. The user adjustable voltage is supplied by two Intersil ISL22444 digital potentiometers, configurable through a SPI. A fixed voltage can be applied by removing a zero ohm jumper, thereby disconnecting the digital potentiometer, and loading resistors into a voltage divider. A fixed voltage may be desirable if the level of noise from the digital potentiometer is unacceptable. The user adjustable voltage is helpful for prototyping and system characterization applications.

The digital potentiometer outputs are all buffered by low noise, unity gain operational amplifiers, National Instruments LM837. These buffers are necessary because the digital potentiometer output cannot source sufficient current.

The digital potentiometer was not used in the final system due to grounding issues, mentioned in Section 2.4. Instead, the fixed voltage output was used and the digital potentiometer was left disconnected. The radiometer output was more stable when the

bias boards' on board resistor dividers were used than when the digital potentiometer outputs were used.

4.2.3 System Health Monitor

The system health ADC, Linear Technologies LT2439, is an eight-channel differential input sigma-delta converter. It is used for monitoring four thermistors and a current sensing resistor that senses the total LNA drain current. The conversion time for this ADC is 150 ms. Communication is accomplished through a SPI. Not all of the ADC inputs are currently being utilized, and three more inputs could be added in future revisions of the board. Also, a 16-bit ADC is not necessary for these monitoring applications. On future board revisions, this could be replaced with an 8-bit or 12-bit ADC.

4.2.4 Dicke Switch Driver

The Dicke switch signal from the microcontroller is connected to a M/A–Com MADR–007097–000 switch driver. This driver converts the CMOS voltage input to a level compatible with the MMIC Dicke switch. Several current limiting resistors are included after the switch driver.

4.2.5 Power Supply Regulation

The power supply regulation consists of six linear voltage regulators and a low noise precision voltage reference. The precision voltage reference is used to generate the LNA bias voltages. It outputs 1.25 V and is buffered through a low noise, unity gain operational amplifier to provide current driving capability.

4.2.6 LNA Drain Driver

The LNA drain voltage is generated by the precision voltage reference discussed in Section 4.2.5. A voltage divider and buffer amplifier are included so that any voltage less than or equal to 1.25 V can be generated. The 92 GHz radiometer uses a 1.15 V drain voltage, and the 166 GHz radiometer uses a 0.75 V drain voltage.

The LNA drain bias runs through a switch that the user must close through the user interface. This switch is open upon powering on the back-end board. The open switch allows the LNA gate bias to stabilize prior to applying the drain bias. If the drain bias were applied prior to the gate bias, the LNA could be damaged. After the drain switch, the drain voltage goes through a precision 1-ohm current sense resistor. This allows the system health monitor ADC to record the drain current. From there, the drain voltage is delivered to the MCM.

The loss from the switch and current sense resistor must be taken into account when setting the drain voltage. For example, the 166 GHz radiometer has four LNAs that draw

15 mA each. The drain voltage was set 110 mV higher than required in order to compensate for the voltage drop due to the current sense resistor and switch.

4.2.7 Electromagnetic Interference (EMI) Design Considerations

The first design of the back-end board had problems with noise and data stability. The recorded radiometer data had intermittent noisy patches and large spikes on the recorded data. Initially, electromagnetic coupling from external sources was suspected to be causing the noise issues. External sources were suspected because some of the noisy patches were correlated with external events, such as someone walking by the system or even opening the door to the laboratory. However, the problems persisted even after the back-end board was mounted in a shielded box. Consequently, it was suspected that the problems were due to ground loops and layout problems. The ground loop problems were solved by changing the MCM grounding to a single point ground. The layout issues were two-fold. First, there was a lack of isolation between the analog and digital sections of the data acquisition system, allowing digital noise to contaminate the sensitive analog sections of the board. Second, the EMI was not considered in the initial layout. So, the EMI performance had a lot of potential for improvement.

The digital isolation was improved on the second design of the back-end board in a number of ways. The most important improvement was the complete separation of the digital and analog sections of the data acquisition system. A section of the back-end board is dedicated to interfacing with the microcontroller board. This digital section has a separate ground, i.e. the digital ground, which is completely isolated from the analog

ground. Any digital signals that need to interface with the analog components, e.g. the SPI lines, go through isolation transformers that have a very high common mode transient immunity, greater than 25 kV/μs. These isolation transformers filter common mode digital noise, such as the 96 MHz clock, from these digital signals.

Once the digital signals are filtered by the isolation transformers, they are again filtered by low pass filters. These filters reduce the rise and fall times of the digital signals. Sharp rising and falling edges on digital signals contain high frequency harmonic components. These harmonics are likely to radiate, and can interfere with the sensitive analog circuitry on the board. The filtered digital signals are then routed on internal, digital only, metal layers that are located between AC grounded layers on the board. The AC grounded layers act as shields to further isolate the digital signals. Finally, the digital signals come up through vias near the part they are connected to.

The number of metal layers on the PCB, the designation of each layer, and the spacing between the layers is referred to as the PCB stack-up. The stack-up for the second revision back-end board utilizes more metal layers than the first revision. More layers on a PCB allow the designer to improve the boards' EMI performance. The second revision board is a 6-layer board. The PCB stack-up, from top to bottom, is analog layer 1, ground, isolated digital, +15 V, –15 V, and analog layer 2. As mentioned above, the isolated digital signals are routed between AC grounded signal layers, i.e. ground and + 15 V.

Although they are often ignored, ground currents are a very important consideration when designing for EMI immunity. This is especially true of high frequency signals, but applies to signals with frequencies as low as 1 MHz [26]. All sensitive or high frequency signals should be routed over an AC ground plane in a microstrip, coplanar waveguide, or stripline configuration. Except for the stripline configuration, the ground currents will flow directly beneath the signal path, since this is the lowest impedance return path [26]. Any gap in the ground plane beneath the signal path will disrupt the ground currents. This will add inductance to the return path and cause a voltage drop in the return path. Also, the gap in the return path will cause increased sensitivity to external EMI sources, and will cause the signal being carried to excessively radiate. These EMI issues are due to the ground currents being forced to deviate from the signal path, and thus forming a larger loop of current. This loop of current behaves like a loop antenna [26].

Ground currents also need to be considered when signals change ground planes. For example, when the digital SPI signals on the back-end board need to move from the top layer to the shielded inner layer, the return currents need a path to the new ground plane as well. Wherever signals change ground planes, capacitors (1.0 μF) were added between the two ground planes. These capacitors connect the different ground layers, e.g. +15 V to ground, so that the return currents are able to have a low impedance path between ground planes.

Several areas were found for EMI improvement in the first back-end board design. The digital signals were not filtered or isolated from the analog signals. All four board layers

were used for routing signals; none were dedicated plane layers. There was no AC ground plane under all of the sensitive or higher frequency signal traces. Return currents were not considered. This combination of errors is especially detrimental in a system that measures signals of 1 mV or less.

4.3 Microcontroller Board

The microcontroller development board is manufactured by Atmel, model SAM3U–EK. It is based on the Atmel SAM3U microcontroller, which uses the 32 bit ARM Cortex M3 processor. This embedded processor has a 96 MHz clock rate, as well as on-chip SD card and SPI interfaces. The embedded processor communicates with all of the SPI devices on the back-end board. It records the data from the ADCs onto an SD card, controls the Dicke switch timing, and provides a user interface.

4.3.1 Embedded Processor Software

The embedded code is written in C, using IAR Systems' embedded workbench and ARM compiler. An external computer, such as a laptop, communicates with the embedded processor through an RS-232 serial interface. The code requires user input to begin running. The user must close the drain bias switch and enable any system health monitor data to be recorded on the SD card.

The main microcontroller code runs in an infinite loop. It exits this loop when the user presses a button on the computer that is connected via RS-232. Every 50 ms, the loop is

interrupted to read the radiometer ADC. Every 500 ms, the data from the radiometer ADC is written to the SD card and the Dicke switch is toggled. The length of these intervals can be changed, although the ADC sample time cannot be reduced below 16 ms, the conversion time of the ADC. If the user has enabled system monitoring data to be written to the SD card, such as thermistor voltages or drain current magnitude, it will be written every 90 seconds.

If the user pushes a button on the attached computer while the code is running in its main loop, it will break out of its loop and change to the user interface mode. In the user interface mode, interrupts are disabled, no data is being recorded, the Dicke switch is not being toggled, and the software is waiting for user input. From the user interface, the user has the following options: communicate with all of the SPI devices on the back-end board, toggle the Dicke switch, adjust the digital potentiometer levels, read all of the ADC voltages, open or close the drain current switch, disable or enable Dicke switching (changing between a total power and a Dicke radiometer), enable or disable what system health monitor data is written to the SD card, and quit the testing.

Chapter 5: Conclusions and Future Work

A three-channel radiometer operating at 92, 130, and 166 GHz was designed, fabricated and tested. This MMIC-based, millimeter-wave radiometer, in conjunction with a multi-channel radiometer operating between 18 and 37 GHz, is expected to improve satellite based retrieval of wet tropospheric path delay in regions close to the coasts. Design philosophy as well as test results were discussed for both the 92 and 166 GHz systems.

5.1 Wet Path Delay Performance

For the use of the radiometer in its intended application, the wet path delay performance is more important than any other system metric. The accuracy of the wet path delay retrievals is related to the radiometer's radiometric resolution and long term stability. The initial goal for this work was to achieve wet path delay accuracy of better than 1 cm. The sensitivity of wet path delay to brightness temperature as a function of the amount of wet path delay is shown in Figure 5-1 for various frequencies. The sensitivity is highly nonlinear, but a worst case point can be chosen to represent the worst path delay accuracy at each frequency.

The lowest sensitivity for the 90 GHz channel is approximately 1.8 K/cm at a path delay of approximately 27 cm and greater. The minimum Allan deviation for the 92 GHz radiometer was measured to be 0.2 K in a total power mode and simulated to be 0.05 K in a Dicke mode, as shown in Figure 2-53. This corresponds to a worst case wet path delay accuracy of approximately 0.1 cm in a total power mode and 0.03 cm in a Dicke mode.

At approximately 27 cm and greater of wet path delay, the 160 GHz channel is saturated and is not sensitive to changes in wet path delay. For low values of path delay, up until approximately 17 cm, the 160 GHz channel is more sensitive than the 90 GHz channel. The minimum Allan deviation for the 166 GHz radiometer was measured to be 1.1 K in a total power mode and simulated to be 0.1 K in a Dicke mode, as shown in Figure 3-37. These correspond to a path delay accuracy of less than 1 cm up to approximately 22 cm of path delay when operating in a total power mode, and up to 26 cm when operating in a Dicke mode.

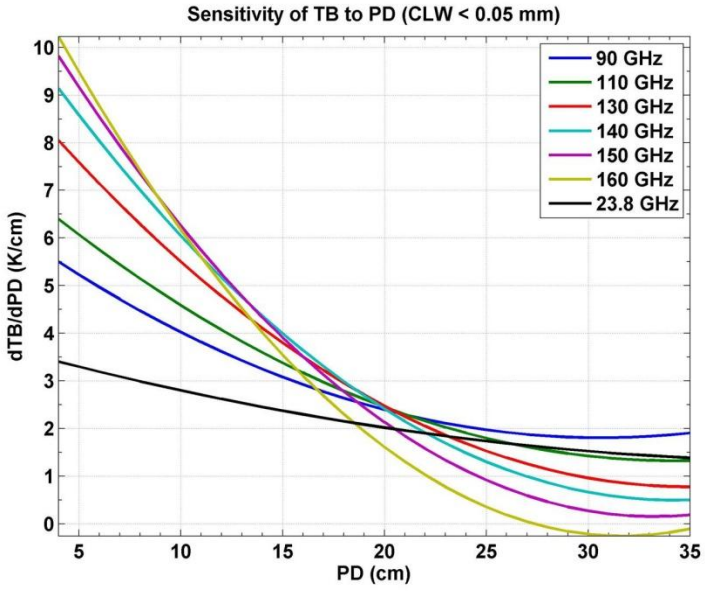

Figure 5-1. Sensitivity of brightness temperature to path delay [5]

5.2 Scientific Contributions

This work has demonstrated the operation of internally calibrated, MMIC based, Dicke radiometers at 92 and 166 GHz. These radiometers observe two internal calibration sources without the use of moving parts. These are a Dicke-switched matched load at ambient physical temperature and a high ENR coupled noise source. Based on their use of MMIC and microstrip-based components, these radiometers are especially well suited for satellite deployment. The radiometric resolution of these radiometers compares well with current NOAA instruments operating at similar frequencies without internal calibration. This comparison is shown in Figure 2-53 and Figure 3-37. The radiometers described in this work are lower mass than these operational NOAA instruments. AMSU A-1, which includes an 89 GHz channel, has an average radiometer mass of 3.8 kg per channel [27]. The 166 GHz radiometer designed in this work weighs only 1.24 kg, and the 92 GHz radiometer weighs 1.48 kg. These values do not include power supplies or temperature control modules.

5.3 Lessons Learned: 92 GHz Radiometer

The 92 GHz channel was the first radiometer designed as part of this work. As such, many lessons were learned during the design, fabrication, and testing of this system. A number of changes could be made to this radiometer to improve its overall performance.

The first change to the radiometer would be replacing the Dicke switch. The 92 GHz radiometer is currently using a M/A-COM, MA4GC6773, 77 GHz SPDT switch. The 77 GHz switch has a measured insertion loss of approximately 3 dB across the radiometer's bandwidth. The JPL-designed 80-135 GHz switch has less than 2 dB insertion loss across the bandwidth of the radiometer. This switch would improve the radiometer's noise temperature from 1260 K to just below 1000 K, approximately 20% improvement. In turn, this would reduce the radiometric resolution from 0.37 K to 0.31 K for an integration time of 10 ms.

The operational amplifier on the output bias board of the 92 GHz radiometer can be changed to a chopper-style amplifier. Chopper amplifiers, also known as zero-drift amplifiers, use internal calibration to remove most of the operational amplifier's offset voltage. Also, they have much lower input bias current and offset current than conventional operational amplifiers. Since the voltages being measured are so small, and so much post detection gain is needed, i.e. approximately 60 dB, the offset voltages and input bias currents add significant error. Furthermore, the long term drift and temperature coefficient of the offset voltage for conventional operational amplifiers are much higher than that of the chopper amplifier.

The 92 GHz bandpass filters would have benefitted from the optimization algorithm used in the design of the 166 GHz bandpass filters. As mentioned in Section 2.2.1.1, the 92 GHz filter was optimized by hand. This was very time consuming and resulted in the simulated bandwidth of the filter being larger than desired. It also resulted in the low lid

heights directly above the filter matching networks. These lower lid heights above part of the filter are sensitive to position along the filter, so the alignment of these portions may not be correct without high precision machining. These issues could have been avoided if the optimization tool had been used.

The dimensions and mass of the 92 GHz MCM could be reduced by making some sections of the MCM lid and bottom thinner. The dimension of the waveguide flange at the MCM RF input determined the thickness of the entire MCM. However, the other sections of the MCM do not have to be this thick, and could have cutouts to further reduce the mass of the MCM.

The waveguide-to-microstrip transition used in the 92 GHz radiometer did not use a tapered probe. A tapered probe reduces parasitic capacitance caused by potential misalignment of the transition. It improves component performance in the event that the assembly is not perfect. Also, alignment marks should have been included on the transition. These marks make aligning the probe in the RF trench easier and help in achieving the desired performance of the waveguide-to-microstrip transition.

Including power detector protection circuitry is vital. If this circuitry would have been included at the outset, many hours of troubleshooting would have been saved. For future MCM designs, it is recommended to include the protection circuitry shown in Figure 2-46.

Only one copy of the MCM was fabricated for the 92 GHz radiometer. For future designs, at least two MCMs should be fabricated. The additional cost and time required to fabricate and assemble a second MCM is not much more than for the first MCM. The second MCM eases troubleshooting by having a second system to determine problems and test solutions. It also provides insurance if one of the MCMs is damaged.

5.4 Lessons Learned: 166 GHz Radiometer

Some of the improvements that were recommended for the 92 GHz design are also applicable to the 166 GHz design. The first is the addition of alignment marks on the waveguide-to-microstrip transition. Second, the MCM mass could be reduced by adding cutouts in sections where thick metal is not necessary.

The RF gain change when switching between the matched load and antenna needs to be studied and understood. Engineers at JPL have designed a matched load with ultra-wide bandwidth, from 80 to 180 GHz. The physical dimensions of this matched load are similar to those of that currently used in the 166 GHz radiometer. The current matched load should be replaced with the ultra-wideband matched load. Testing with the ultra-wide bandwidth component will indicate whether or not the gain change is caused by a matching issue. Also, microwave absorber could be added to first LNA's cavity. This absorber will help to reduce any cavity resonances.

Some effort should be invested in reducing the level of noise in the measured data from the 166 GHz radiometer. A first step would be the addition of an SMA connectorized, packaged amplifier. The amplifier would connect directly to the output of the waveguide power detector. This would add a gain stage that has a very low impedance ground connection to the power detector ground. This would boost the signal level prior to the back-end board and give the system additional noise immunity.

5.5 Design Improvements: Back-end Board

The stability of the radiometers could be improved by increasing the amount of thermal control on the back-end board. This would also reduce the required warm up time of the radiometers. A Peltier device, similar to the one that thermally controls the MCM, could be added to the back-end board.

The size of the back-end board could be reduced, and additional thermal monitoring ADC channels could be added. The back-end board was designed to be as flexible as possible, so that it could be used for all three radiometers. Several components on the back-end board are not being used in any of the designs, such as the digital potentiometers and their buffer amplifiers. Eliminating the digital potentiometers and their buffer amplifiers would greatly reduce board area.

For the same reasons mentioned in Section 5.2, the first amplifier on the back-end board should be changed to a chopper-style amplifier. This was implemented in the 166 GHz

design. It is especially important for that design, since the 166 GHz radiometer does not have an amplifier inside of the MCM.

5.6 MMIC Assembly

It is not recommended for students to perform the MMIC assembly work that is required at these high frequencies. The experience required to attain the required level of precision is beyond what can reasonably be acquired by a student who will perform the assembly only once. This work necessitates months or years of practice to obtain the level of skill required. This thesis work was accomplished with the assistance of JPL technicians, Mary Wells and Heather Owens, to perform the assembly work. Without the help of these technicians, it is unlikely that the successful assembly of the MCMs would have been possible.

5.7 Future Work

This work is being extended in the future under an Instrument Incubator Program grant (IIP-10). The IIP includes collaboration between CSU, JPL, and the University of California Los Angeles (UCLA). Under this project, radiometers operating at the frequencies discussed in this paper, along with a multi-channel 18-34 GHz radiometer and sounding spectrometers near 118 GHz and 183 GHz will be flown on an aircraft. It will be designed to fly autonomously on the Global Hawk, similar to JPL's High-Altitude MMIC Sounding Radiometer (HAMSR) that flew in NASA's GRIP mission in 2010

[28]. The IIP will further increase the TRL of the millimeter-wave radiometers. It is intended to demonstrate that the addition of these millimeter-wave radiometers to ocean altimetry missions will improve the accuracy of wet path delay retrievals in areas near the coastline. This field experiment will require that the system, including the millimeter wave radiometers and the data acquisition system, be robust enough to meet the demands of aircraft deployment. This will necessitate an increased level of system stability and thermal control. Thorough mechanical testing will be performed to ensure that all of the components are able to operate under a range of temperatures, pressures, vibrations, and shock loads.

Chapter 6: Works Cited

[1] F. T. Ulaby, R. K. Moore, and A. K. Fung, *Microwave Remote Sensing: Active and Passive, Vol. I -- Microwave Remote Sensing Fundamentals and Radiometry*. Reading, MA: Addison-Wesley, 1981.

[2] M. Durand et al., "The Surface Water and Ocean Topography Mission: Observing Terrestrial Surface Water and Oceanic Submesoscale Eddies," *Proceedings of the IEEE*, vol. 98, no. 5, pp. 766-779, May 2010.

[3] S. Sahoo et al., "3-D Humidity Retrieval Using a Network of Compact Microwave Radiometers to Correct for Variations in Wet Tropospheric Path Delay in Spaceborne Interferometric SAR Imagery," *IEEE Transactions on Geoscience and Remote Sensing*, vol. 49, no. 9, pp. 3281-3290, September 2011.

[4] S. T. Brown, "A Novel Near-Land Radiometer Wet Path-Delay Retrieval Algorithm: Application to the Jason-2/OSTM Advanced Microwave Radiometer," *IEEE Transactions on Geoscience and Remote Sensing*, vol. 48, no. 4, pp. 1986-1992, April 2010.

[5] Shannon Brown, Personal Communication, 2010.

[6] S. Reising et al., "Development of Internally-Calibrated, MMIC-based Millimeter-Wave Radiometers to Enable Correction of Wet-Tropospheric Delay for Coastal Zone Altimetry," in *URSI General Assembly and Scientific Symposium*, Istanbul, TR, 2011, pp. 1-4.

[7] S. T. Brown, S. Desai, W. Lu, and A. B. Tanner, "On the Long-Term Stability of Microwave Radiometers Using Noise Diodes for Calibration," *IEEE Transactions on Geoscience and Remote Sensing*, vol. 45, no. 7, pp. 1908-1920, 2007.

[8] C.S. Ruf, "Detection of calibration drifts in spaceborne microwave radiometers using a vicarious cold reference," *IEEE Transactions on Geoscience and Remote Sensing*, vol. 38, no. 1, pp. 44-52, January 2000.

[9] A. Lee et al., "Development of Internally-Calibrated, MMIC-Based Millimeter-Wave Radiometers Operating at 130 and 166 GHz in Support of the SWOT Mission," in *IEEE International Geoscience and Remote Sensing Symposium*, Vancouver, B.C., Canada, 2011.

[10] A. Lee et al., "Development of High-Frequency, Internally-Calibrated Millimeter-Wave Radiometers Operating at 130 and 166 GHz," in *USNC-URSI National Radio Science Meeting*, Boulder, CO, 2011.

[11] Hewlett Packard. (1981, September) Application Note 986 - Square Law and Linear Detection. [Online]. http://literature.agilent.com/litweb/pdf/5953-4444.pdf

[12] D. M. Pozar, *Microwave Engineering*, 3rd ed. Hoboken, NJ: J. Wiley, 2005.

[13] F. Iturbide-Sanchez, S. C. Reising, and S. Padmanabhan, "A Miniaturized Spectrometer Radiometer Based on MMIC Technology for Tropospheric Water Vapor Profiling," *IEEE Transactions on Geoscience and Remote Sensing*, vol. 45, pp. 2181-2194, July 2007.

[14] G. Matthaei, E. M. T. Jones, and L. Young, *Microwave Filters, Impedance-Matching Networks, and Coupling Structures*. Norwood, MA: Artech House, 1980.

[15] Y. C. Leong and S. Weinreb, "Full Band Waveguide-to-microstrip Probe Transitions," in *1999 IEEE MTT-S International Microwave Symposium Digest*, vol. 4, Anaheim, CA, 1999, pp. 1435 - 1438.

[16] ELVA Corporation. (2003) Waveguide Directional Couplers of DC series. [Online]. http://www.elva-1.com/products/microwave/dircoup.html

[17] O. Montes, D. E. Dawson, and P. Kangaslahti, "High Frequency PIN-Diode Switches for Radiometer Applications," in *NASA Earth Science Technology Forum*, Pasadena, CA, June 2011.

[18] Pekka Kangaslahti, Personal Communication, 2011.

[19] F. Iturbide-Sanchez, "Design, Fabrication and Deployment of a Miniaturized Spectrometer Radiometer Based on MMIC Technology for Troposheric Water Vapor Profiling", 2007, Ph.D. Dissertation, University of Massachusetts, Amherst.

[20] D. W. Allan, "Should the Classical Variance Be Used As a Basic Measure in Standards Metrology?," *IEEE Transactions on Instrumentation and Measurement*,

vol. 1M-36, no. 2, pp. 646-654, June 1987.

[21] D. V. Land, A. P. Levick, and J. W. Hand, "The Use of the Allan Deviation for the Measurement of the Noise and Drift Performance of Microwave Radiometers," *Measurement Science and Technology*, vol. 18, pp. 1917-1928, May 2007.

[22] C.S. Ruf, "Characterization and Correction of a Drift in Calibration of the TOPEX Microwave Radiometer," *IEEE Transactions on Geoscience and Remote Sensing*, vol. 40, no. 2, pp. 509-511, February 2002.

[23] M. A. Aziz, "Ocean Surface Measurements and Calibration Techniques using a Ka-Band Polarimetric Radiometer", 2003, M.S. Thesis, University of Massachusetts, Amherst.

[24] P. Kangaslahti, "Recent Developments in 180 GHz MMIC LNA and Receiver Technology," in *11th Special Meeting on Microwave Radiometry and Remote Sensing of the Environment*, Washington, D.C., 2010, pp. 272-275.

[25] P. Kangaslahti et al., "Radiometer Testbed Development for SWOT," in *NASA Earth Science Technology Forum*, Arlington, VA, June 2010.

[26] P. Brokaw and J. Barrow. (1989) Analog Devices Inc. Web Site. [Online]. http://www.analog.com/static/imported-files/application_notes/600114286955201494896049269845513175558467302082 8AN_345.pdf

[27] NASA Goddard Earth Sciences Data and Information Services Center. (2002, February) Advanced Microwave Sounding Unit-A (AMSU-A) Instrument Guide. [Online].

http://disc.sci.gsfc.nasa.gov/AIRS/documentation/amsu_instrument_guide.shtml

[28] S. T. Brown et al., "The High-Altitude MMIC Sounding Radiometer for the Global Hawk Unmanned Aerial Vehicle: Instrument Description and Performance," *IEEE Transactions on Geoscience and Remote Sensing*, vol. 49, no. 9, pp. 3291-3301, September 2011.

Appendix A: Back-End Board Schematic

The backend board is responsible for providing bias and control signals to the MCM, as well as amplifying and digitizing the power detector output voltage from the MCM. Schematics for the backend board are shown in Figures A1 through A8.

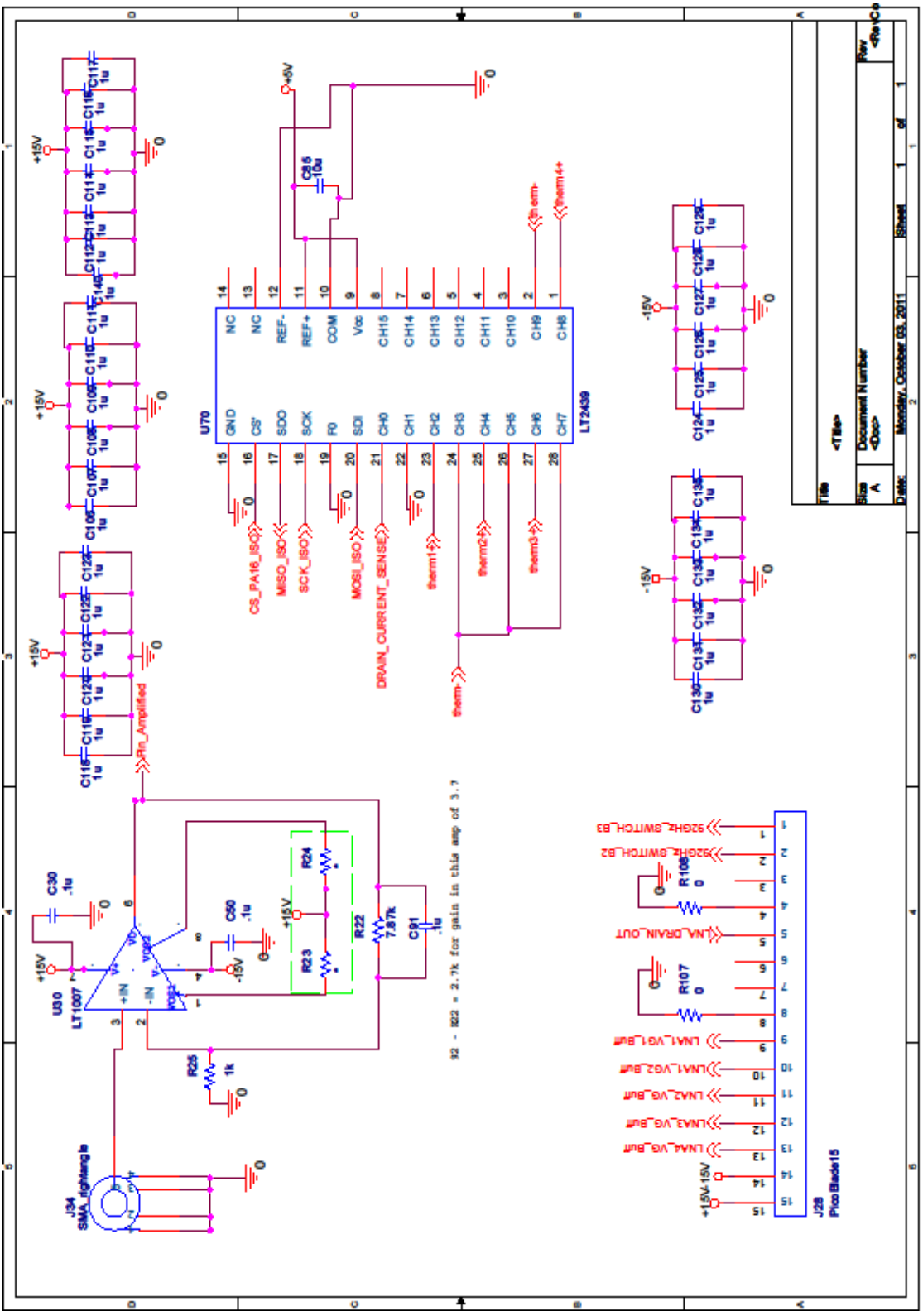

Figure A-1. Back-end board schematic page: 0

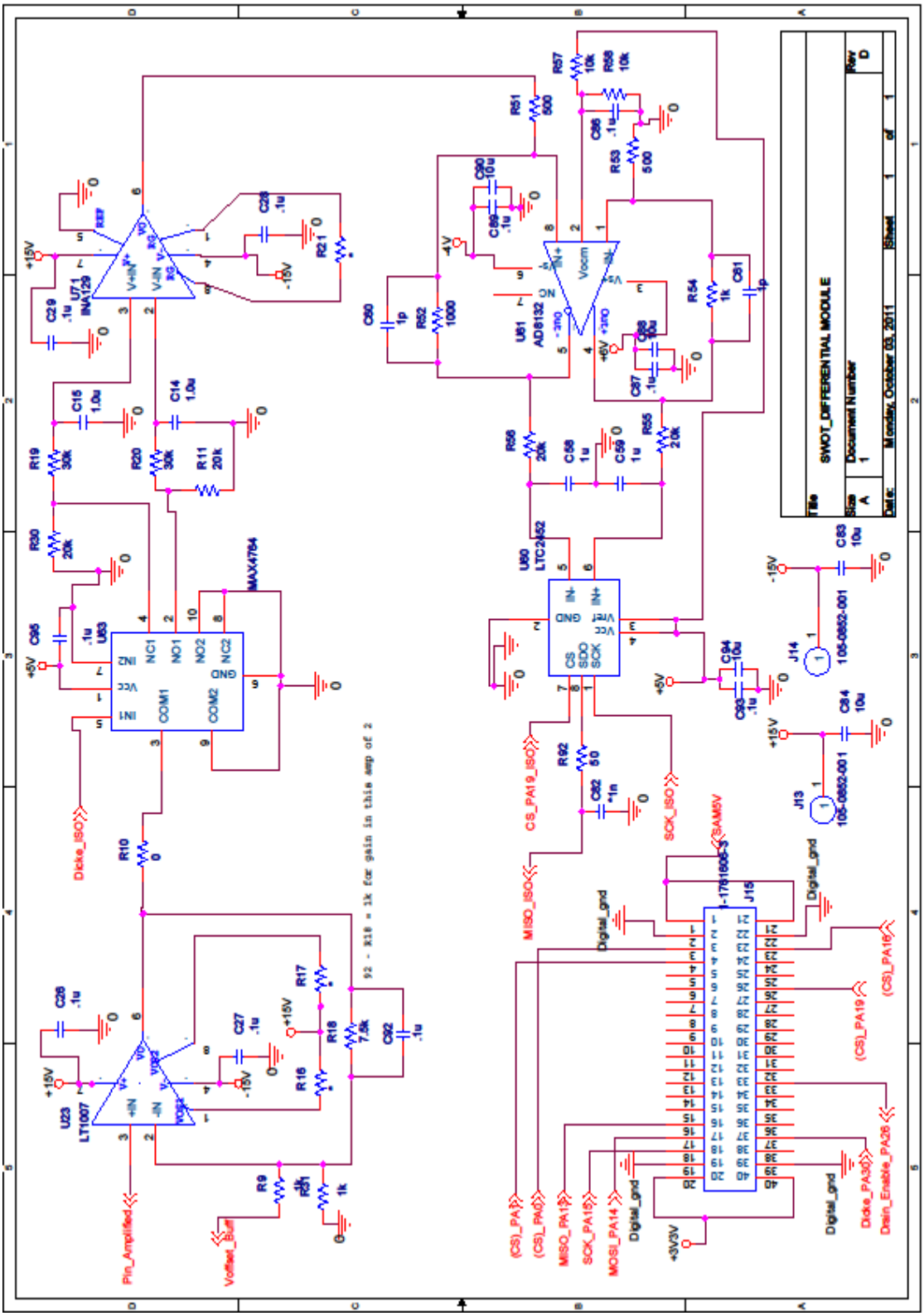

Figure A-2. Back-end board schematic page: 1

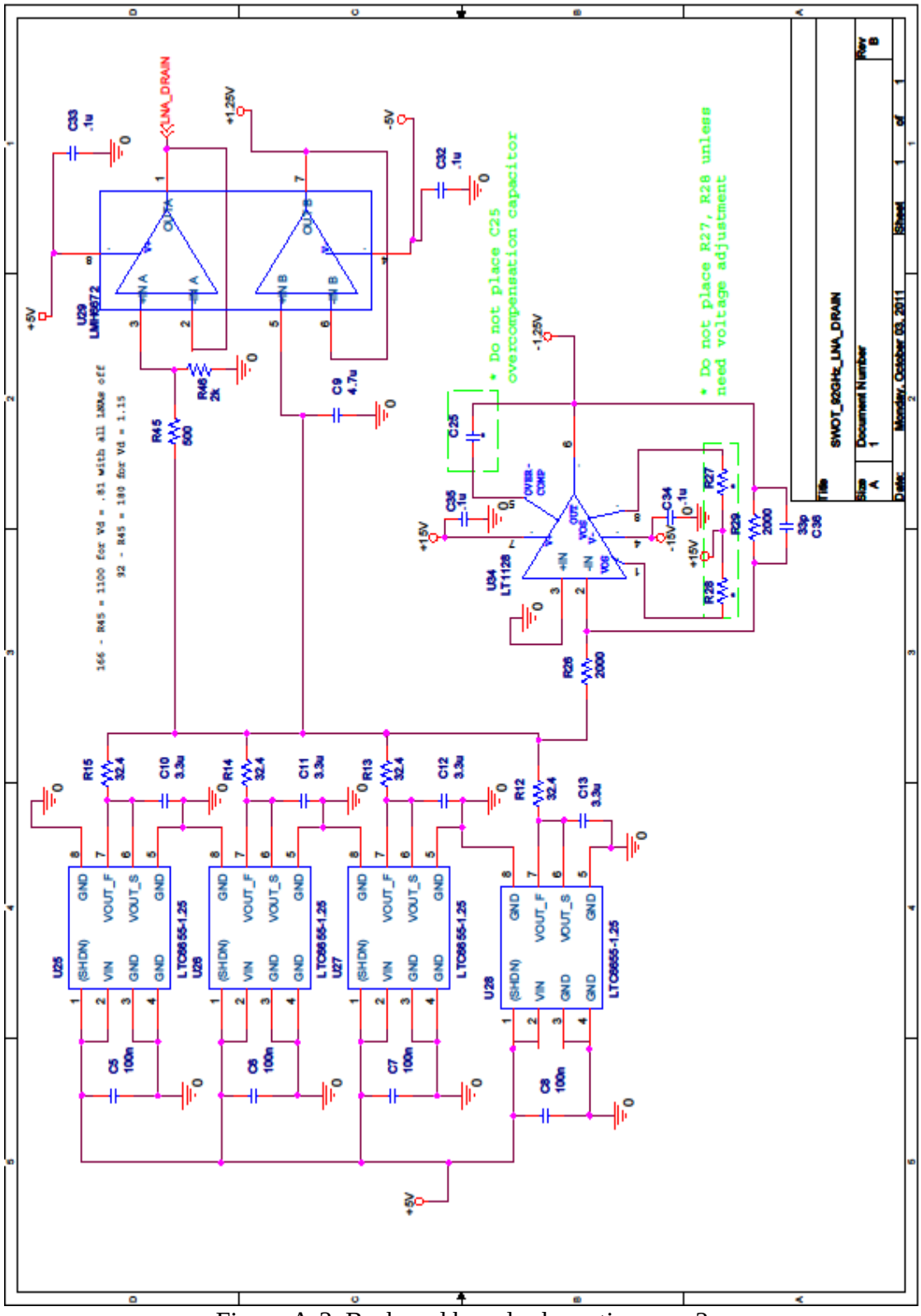

Figure A-3. Back-end board schematic page: 2

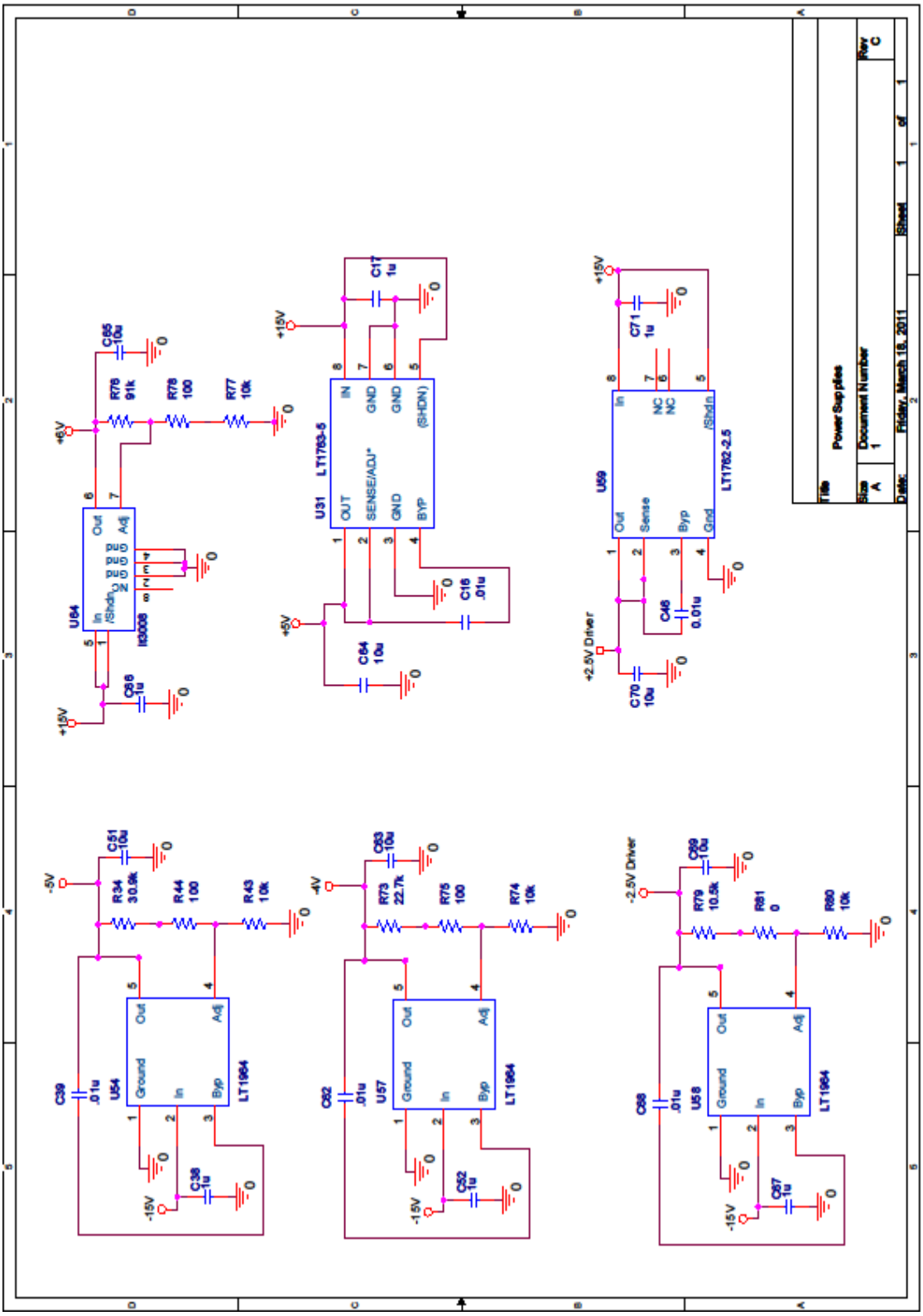

Figure A-4. Back-end board schematic page: 3

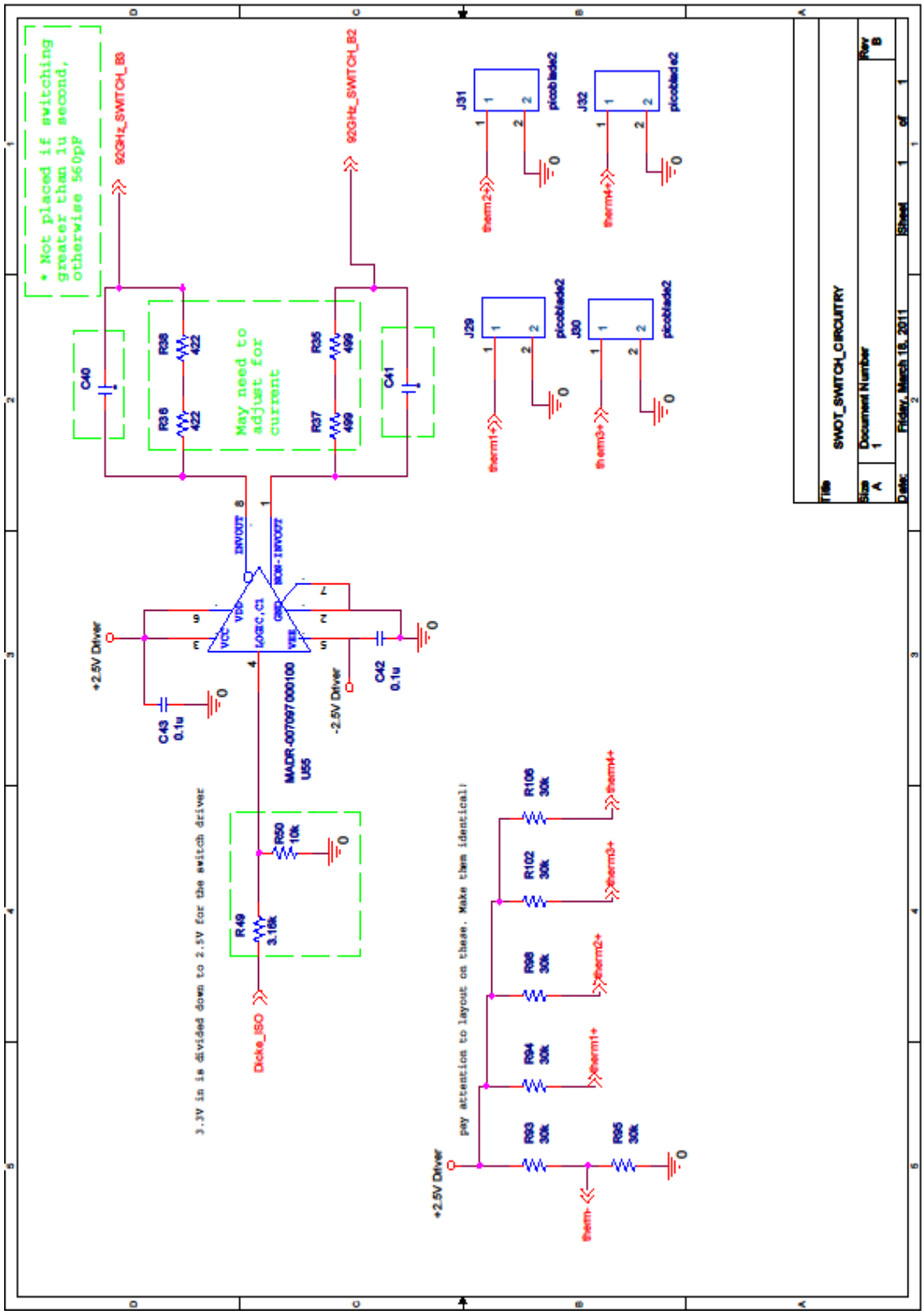

Figure A-5. Back-end board schematic page: 4

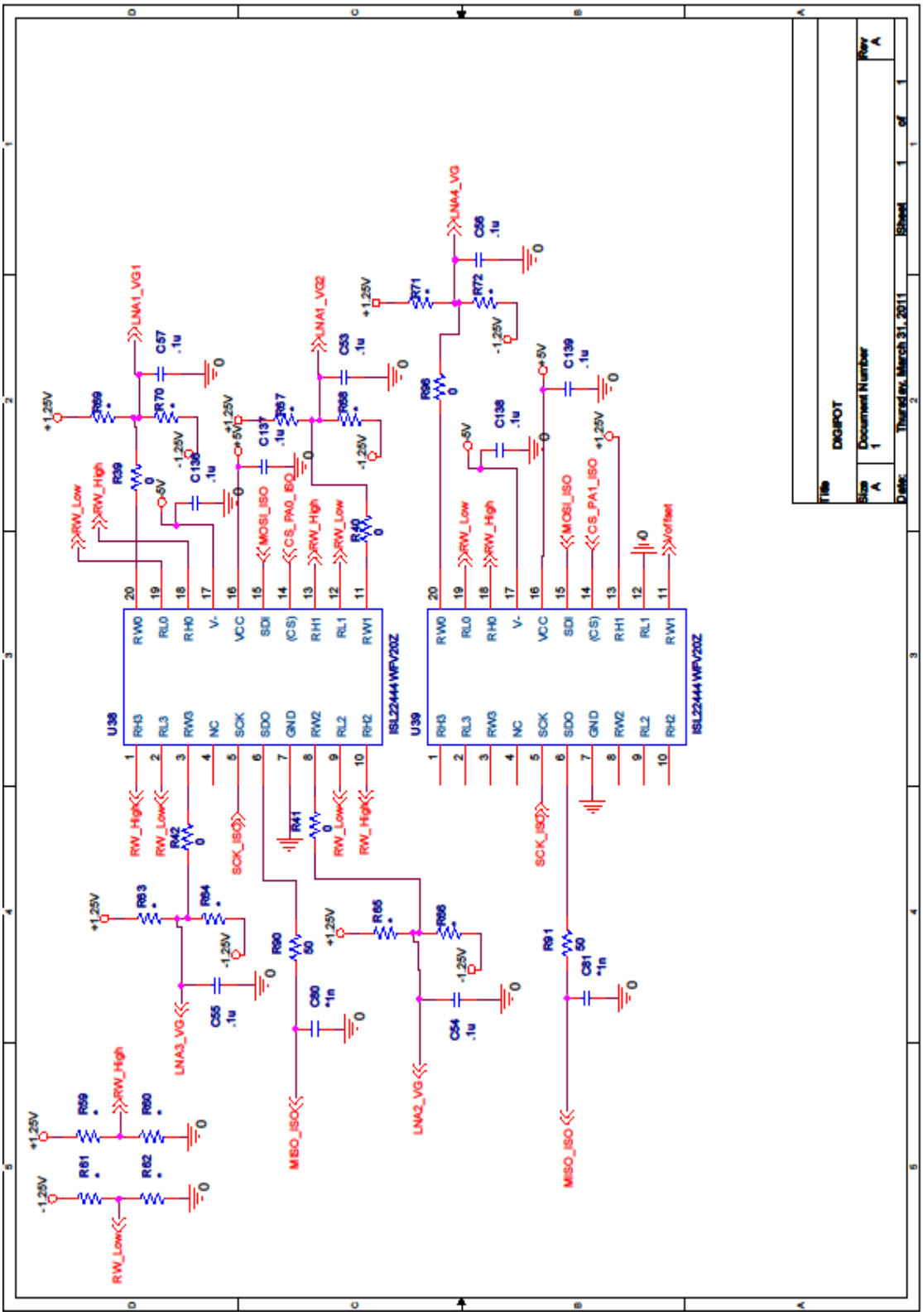

Figure A-6. Back-end board schematic page: 5

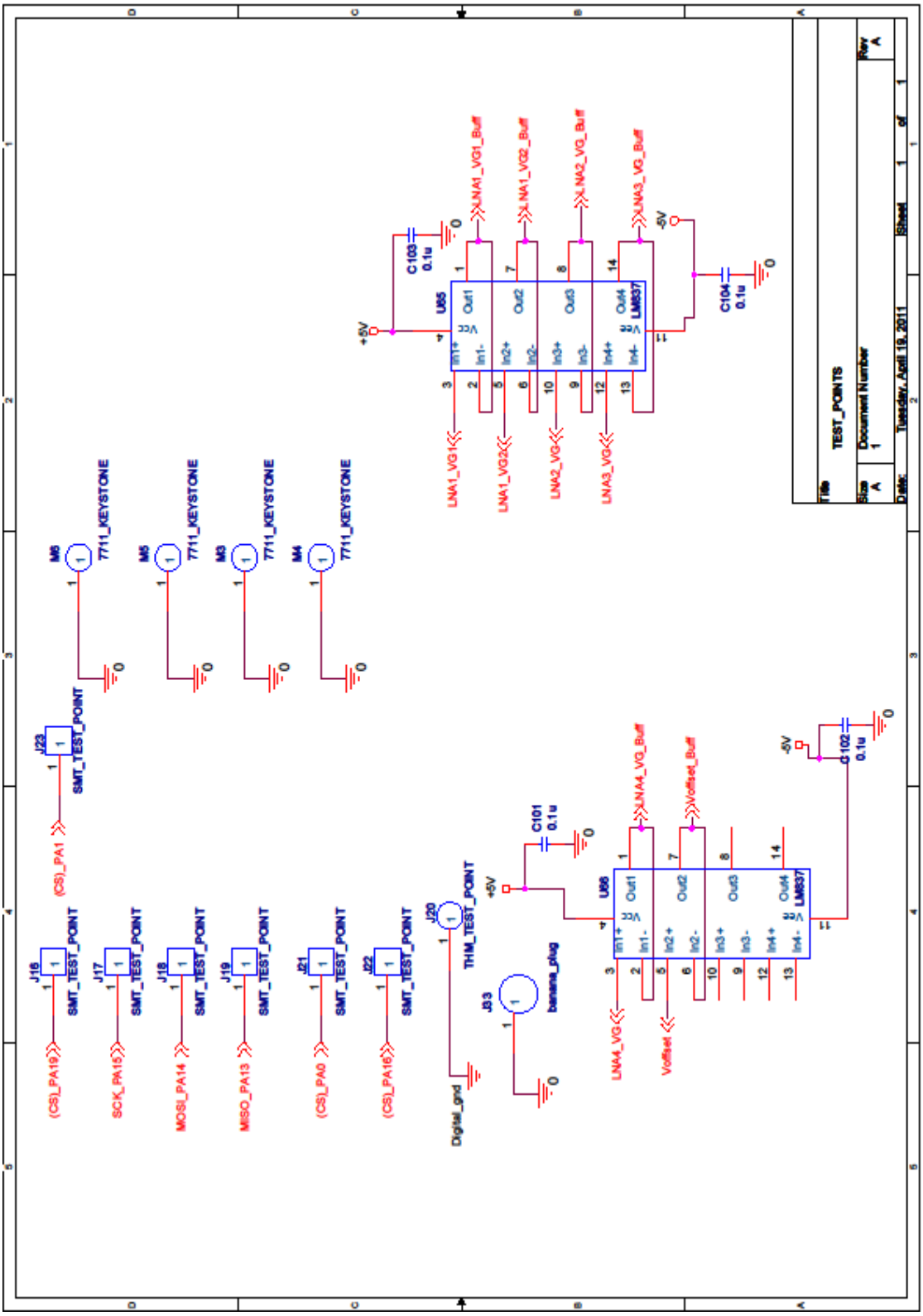

Figure A-7. Back-end board schematic page: 6

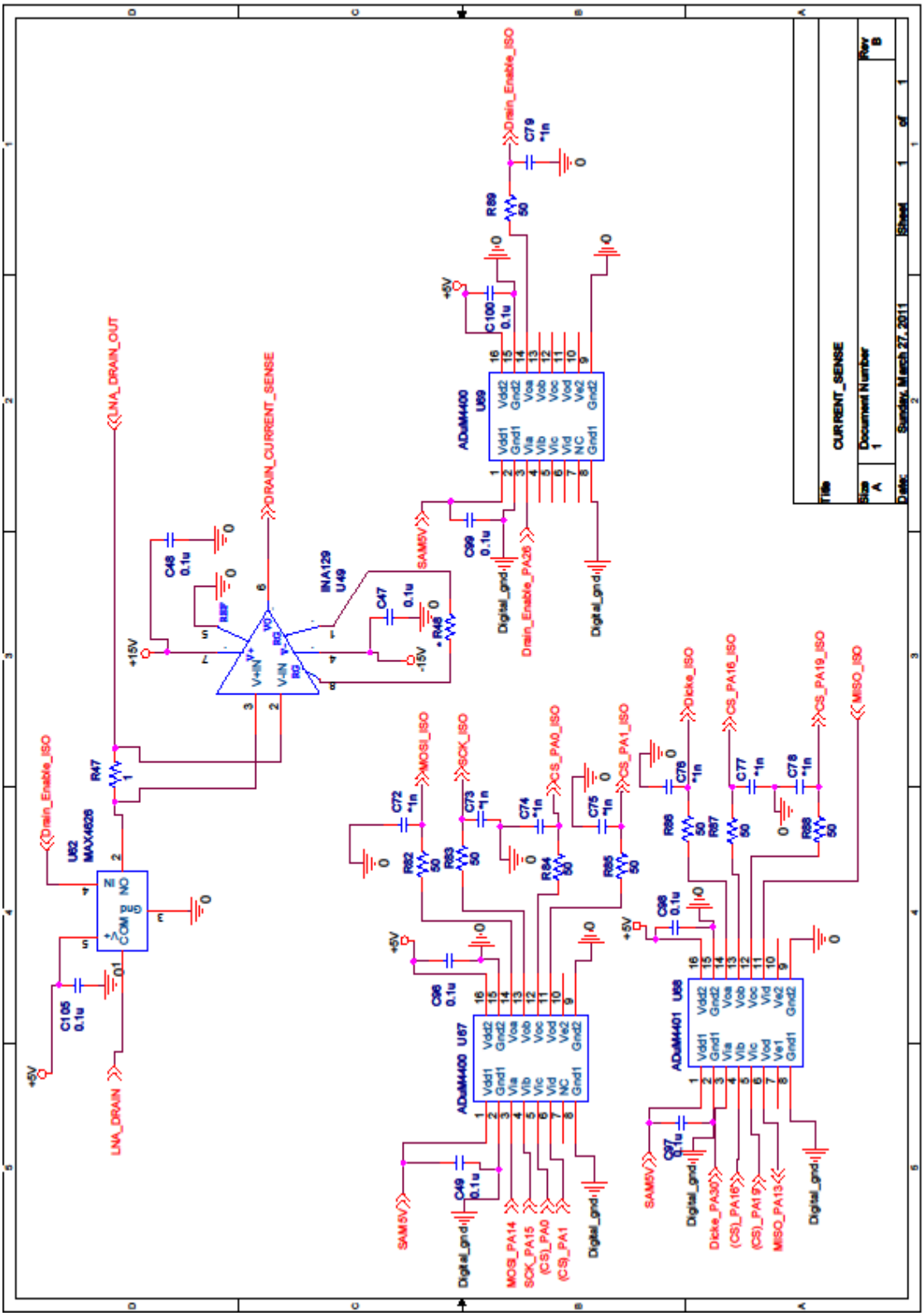

Figure A-8. Back-end board schematic page: 7

Appendix B: 166 GHz MCM Bias Board Schematics

The 166 GHz radiometer utilizes two bias boards, a gate bias board and a drain bias board. The drain bias board schematic is shown in Figure B-1; the gate bias board schematic is shown in Figures B-2 and B-3.

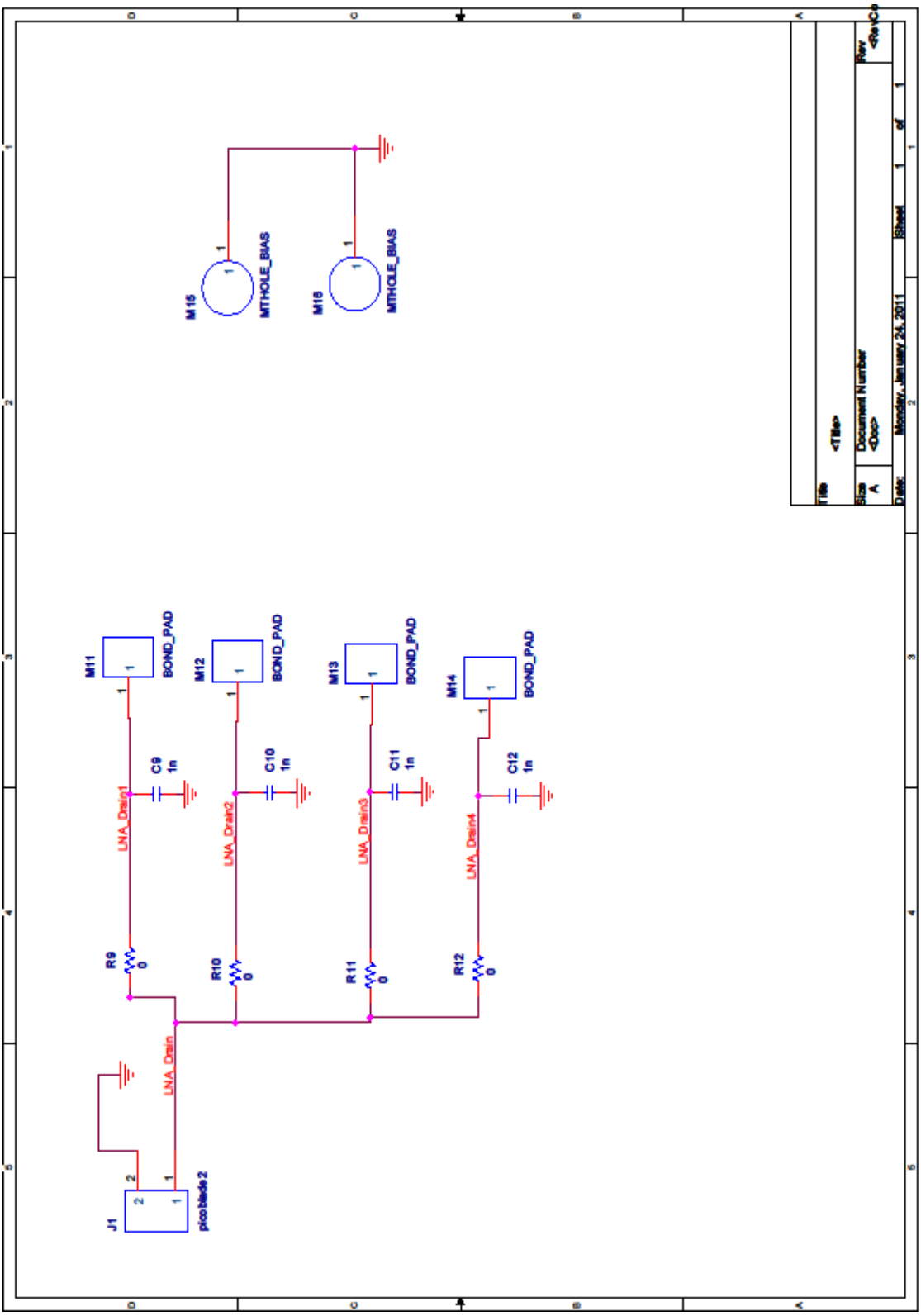

Figure B-1. 166 GHz drain bias board schematic

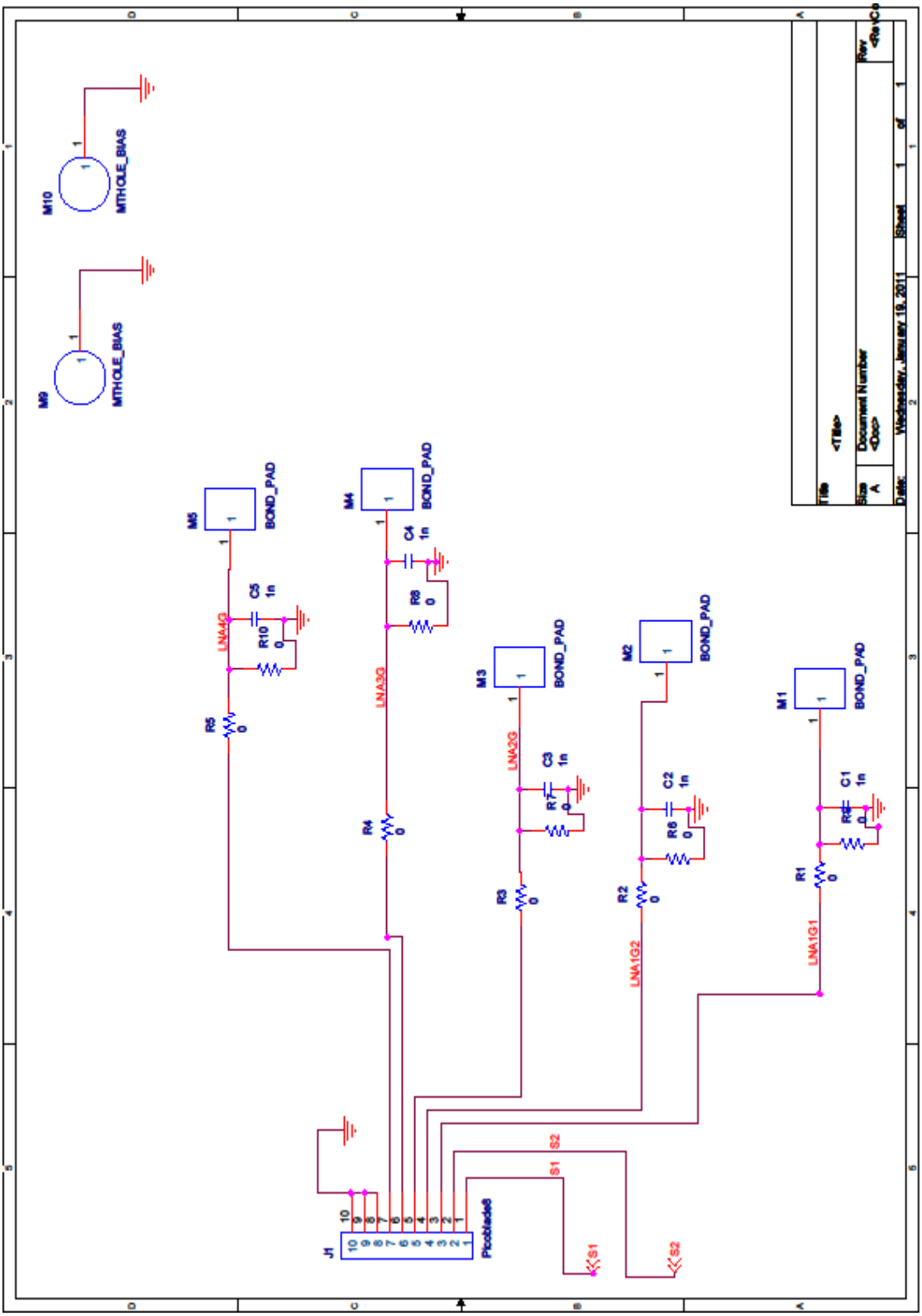

Figure B-2. 166 GHz gate bias board schematic page: 0

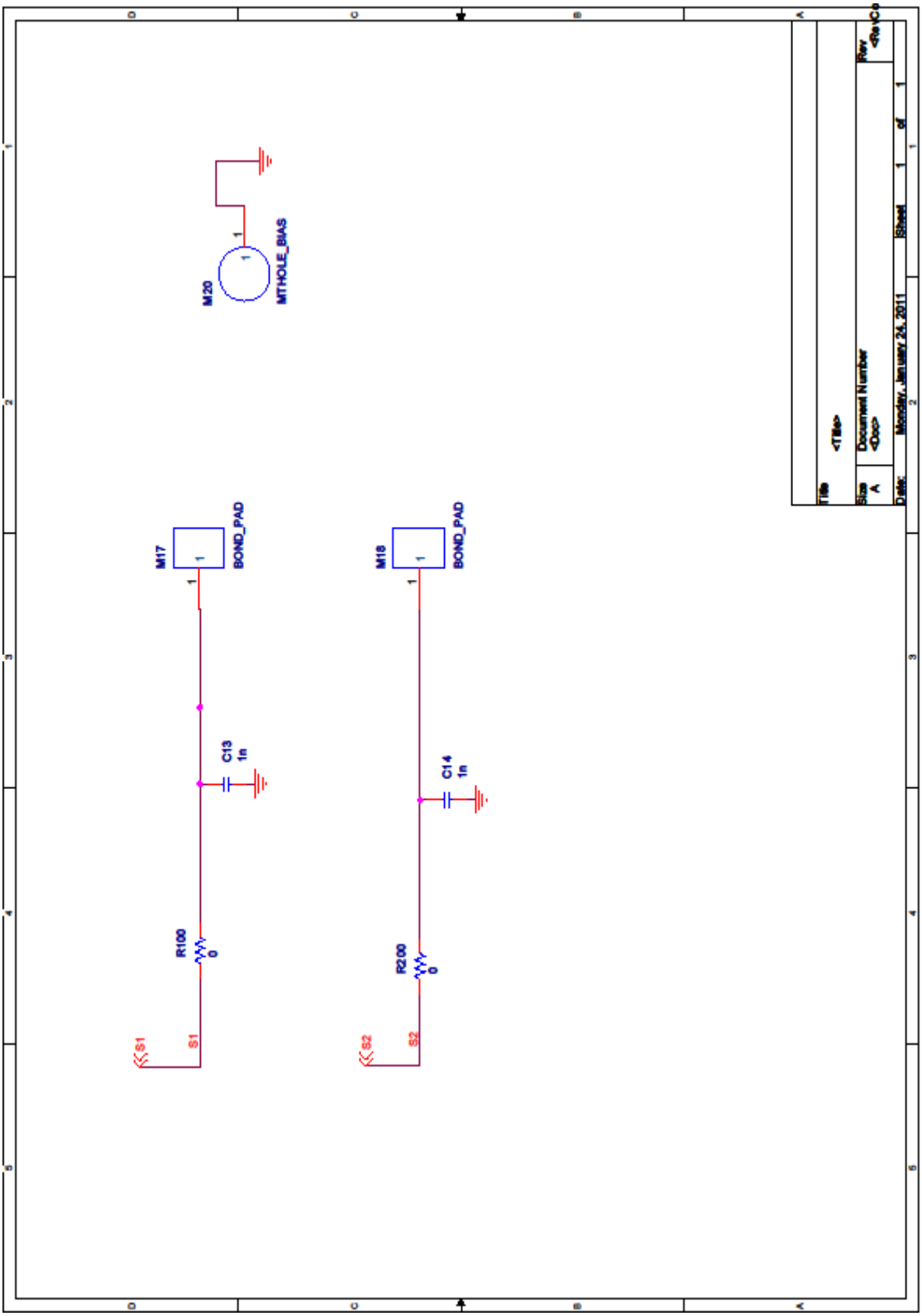

Figure B-3. 166 GHz gate bias board schematic page: 1

Appendix C: 166 GHz Alumina Substrate DXFs

The following drawings for the custom thin film components were supplied to Applied Thin Film in a .dxf format. These are shown to provide future students with an example of what documentation the vendor requires in order to fabricate thin film components.

Figure C-1. 166 GHz matched load

Figure C-2. 166 GHz waveguide-to-microstrip transition

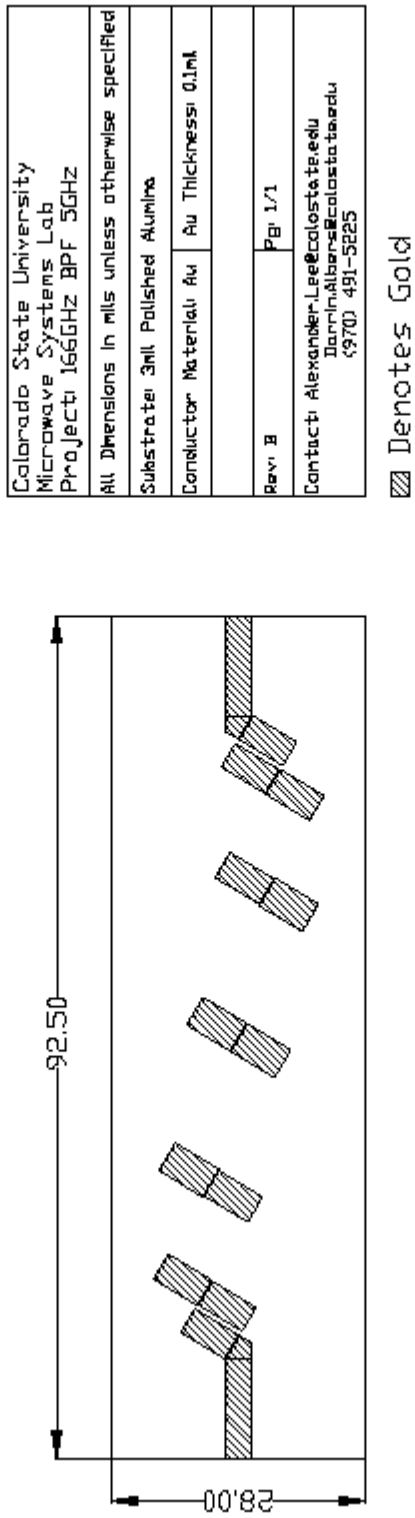

Figure C-3. 166 GHz narrowband filter

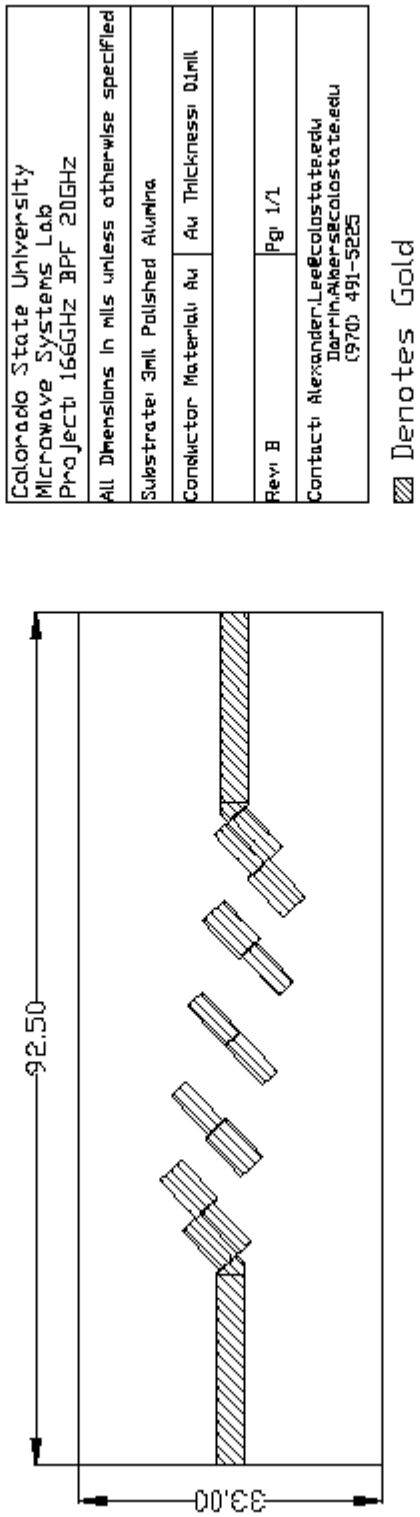

Figure C-4. 166 GHz wideband filter